Olfactory flow in the sea catfish, *Ariopsis felis* (L.): origin, regulation, and resampling

Matthew A. L. Cox[a], Russell J. Garwood[b], Julia Behnsen[c], Jeremy N. Hunt[d], Luke J. Dalby[e], Graham S. Martin[e], James S. Maclaine[f], Zhijin Wang[a], Jonathan P. L. Cox[g]

[a]Department of Mechanical Engineering, University of Bath, Bath, BA2 7AY, UK.
[b]Department of Earth and Environmental Sciences, University of Manchester, Manchester, M13 9PL, UK.
[c]Henry Moseley X-ray Imaging Facility, University of Manchester, Manchester, M13 9PY, UK.
[d]Jeremy Hunt Design, Unit A6, 66 Norlington Road, London, E10 6LA, UK.
[e]TotalSim, Top Station Road, Brackley, NN13 7UG, UK.
[f]Department of Life Sciences, Natural History Museum, Cromwell Road, London, SW7 5BD, UK.
[g]Department of Chemistry, University of Bath, Bath, BA2 7AY, UK.

Abstract

The olfactory epithelium of the sea catfish, *Ariopsis felis*, is found on a pinnate array of lamellae (the olfactory rosette) housed within a nasal chamber. The nasal anatomy of *A. felis* suggests an ability to capture external water currents. We prepared models from X-ray micro-computed tomography scans of two preserved specimens of *A. felis*. We then used dye visualisation and computational fluid dynamics to show that an external current induced a flow of water through a) the nasal chamber and b) the sensory channels of the olfactory rosette. The factors responsible for inducing flow through the nasal chamber are common to fishes from two other orders. The dye visualisation experiments, together with observations of sea catfishes *in vivo*, indicate that flow through the nasal chamber is regulated by a mobile nasal flap. The position of the nasal flap – elevated (significant flow) or depressed (reduced flow) – is controlled by the sea catfish's movements. Flow in the sensory channels of the olfactory rosette can pass through either a single channel or, via multiple pathways, up to four consecutive channels. Flow through consecutive sensory channels (olfactory resampling) is more extensive at lower Reynolds numbers (200 and 300, equivalent to swimming speeds of 0.5 – 1.0 total lengths s^{-1}), coinciding with the mean swimming speed of the sea catfishes observed *in vivo* (0.6 total lengths s^{-1}). Olfactory resampling may also occur, via a vortex, within single sensory channels. In conclusion, olfactory flow in the sea catfish is regulated and thoroughly sampled by novel mechanisms.

Keywords: *Anguilla*; microfluidic chemical sensor; *Esox*; Polypteridae; sturgeon.

1. Introduction

Many animals use the energy available in an external current to drive flow through some part of them or their surroundings (Vogel, 1978). We are interested in how fishes capture an external water current for convectively transporting odorant molecules into the vicinity of the olfactory epithelium (Cox, 2008). Our interest stems from a desire to understand one aspect (odorant transport) of a fundamental biological process (olfaction). In fishes at least, odorant transport has received little attention. The knowledge gained from studying odorant transport in fishes may also be applied to the design of artificial chemical sensors (Rouhi, 1997; Settles, 2005).

In this report, we investigate how a sea catfish, *Ariopsis felis* (Ariidae; Nelson, 2006, pp. 181-182; Fig. 1), captures and exploits an external water current for convective odorant transport. We chose *A. felis* for two reasons. First, its nasal anatomy suggests that it is indeed capable of capturing an external water current (Zeiske et al., 1994). For example, the incurrent nostril is directed towards oncoming flow (Fig. 1B, inset, horizontal white arrow), whilst the relatively large excurrent nostril is normal to oncoming flow (Fig. 1B, inset, vertical white arrow). These features are hallmarks of a fish able to capture an external water current (Cox, 2008). The second reason for choosing to study *A. felis* was its pinnate (feather-like) array of olfactory lamellae (the olfactory rosette, Fig. 2C), where the olfactory sensory epithelium is found (Zeiske et al., 1994). There is no obvious *internal* agent (i.e. accessory sacs or a uniform field of motile non-sensory cilia) for driving flow through the interstices (sensory channels) between these lamellae. Consequently, we hypothesised that in *A. felis* an external water current is responsible for driving flow through the olfactory sensory channels.

For our investigation, we used the complementary techniques of dye visualisation and computational fluid dynamics (CFD; Garwood et al., 2019, 2020). The anatomically accurate models that we used for our experiments were derived from X-ray micro-computed tomography (micro-CT) scans of two well-preserved specimens (e.g. Fig. 1). Both specimens had visibly intact olfactory rosettes (e.g. Fig. 2). To inform our study, we used a) micro-CT scans of two other preserved specimens of *A. felis*, and b) observations of living specimens of *A. felis* in a public aquarium. We also inspected the nasal anatomy of another sea catfish, *Galeichthys feliceps* (Ariidae; Nelson, 2006, p. 182).

We compare our results with those from our previous studies of externally-induced flow in fishes (Abel et al., 2010; Garwood et al., 2019, 2020), and with those from studies of olfactory flow in several other fishes. The fishes featured in the comparisons are from five different orders (Acipenseriformes, Anguilliformes, Esociformes, Polypteriformes, and Siluriformes; Nelson, 2006).

There are two previous studies of the olfactory system of *A. felis* (Caprio, 1980; Zeiske et al., 1994; both refer to *Ariopsis felis* as *Arius felis*). Caprio's study focused on the olfactory sensitivity of *A. felis*, but mentions the possibility of flow regulation through the nasal chamber, which we also discuss here. Zeiske et al.'s study concerned the gross morphology and fine structure of *A. felis*'s olfactory organ; we make additional observations on *A. felis*'s nasal anatomy here.

2. Materials and methods

Much of our methodology has been described before (Cox, 2008; Abel et al., 2010; Holmes et al., 2011; Howard et al., 2013; Ramsey et al., 2015; Garwood et al., 2019, 2020). We therefore give only brief descriptions here. Further details are given in the Appendix. Values for the density and dynamic viscosity of water are taken from Haynes and Lide (2011, p. 6-7), and Table 1 of Goldstein (1965), respectively.

2.1. Preserved specimens

The preserved specimens of *Ariopsis felis* (Fig. 1; see also Fig. A.1, Appendix A.4) used for this study are from the Natural History Museum, London, UK, catalogue numbers BMNH 1983.7.6.11-12 (two specimens) and 1948.8.6.195-196 (two specimens). The specimens were caught at Dauphin Island, Alabama, USA and Port Aransas, Texas, USA, respectively. The total lengths (Fig. 1A, *TL*; Helfman et al., 2009) of these specimens are 13 cm (BMNH 1983.7.6.11-12) and 18 cm (BMNH 1948.8.6.195-196). Since capture, the specimens have been stored in 70 % industrial methylated spirits, 30 % distilled water. Importantly, the lamellae within the olfactory rosettes of these specimens did not generally adhere to each other in the absence of the preservative fluid (Fig. 2B). This observation indicated that the olfactory lamellae were relatively stiff, and therefore could be faithfully represented by a rigid model. We also inspected a preserved specimen of *Galeichthys feliceps* from the Natural History Museum, London, catalogue number BMNH 2016.8.17.102 (Fig. A.2, Appendix A.4).

Note that both *A. felis* and *G. feliceps* have three pairs of barbels: a pair of lateral barbels, and two pairs of ventral barbels (Fig. 1C; see also Figs. A.1 and A.2, Appendix A.4).

2.2. Aquarium specimens

Five specimens of *A. felis* (the ‘aquarium specimens’) were observed *in vivo* at a large, professionally-maintained, publicly-accessible aquarium in Cabela’s, a retail store in Gonzales, Louisiana, USA, 6 – 8 May 2017. The observations were recorded with a hand-held Panasonic HC-V270 digital camcorder (50 frames s^{-1}, 1920 pixels x 1080 pixels per frame). Footage was analysed using the software Adobe Premiere Pro CC.

2.3. Micro-CT

Micro-CT of the four preserved specimens of *A. felis* was done at the Henry Moseley X-ray Imaging Facility, University of Manchester, UK, using an XT H 225 system. All scans were performed in air. The voxel size was 20 μm x 20 μm x 20 μm for the scan of specimen BMNH 1983.7.6.11, and 16 μm x 16 μm x 16 μm for the scan of BMNH 1983.7.6.12 and 26 μm x 26 μm x 26 μm for the scan of BMNH 1948.8.6.195 and that of BMNH 1948.8.6.196. Each scan comprised the head only (e.g. Fig. 1A, region anterior to white marks). Further details of the scans are given in Appendix A.1.1.

We chose the scans of BMNH 1983.7.6.12 and BMNH 1948.8.6.196 to convert to models for dye visualisation and CFD (Model 1 and Model 2, respectively, Table 1). We chose the scan of BMNH 1983.7.6.12 because it had the highest resolution (i.e. smallest voxel size) and least noise (cf. Fig. 3B and C). Consequently, this scan gave the most well-defined olfactory rosettes in the surface model. Notably, the olfactory lamellar attachments to the nasal chamber wall were intact (cf. arrowheads in Fig. 3B and C). Both excurrent nasal flaps of BMNH 1983.7.6.12 were elevated (e.g. Fig. 4A, white asterisk), and its mouth was shut (Fig. 1C, white disk). We chose the scan of BMNH 1948.8.6.196 because one excurrent nasal flap was elevated whilst the other was depressed (Fig. 4B, yellow asterisk), allowing us to determine the effect of the latter on flow (e.g. whether flow passed through the nasal chamber when the excurrent nasal flap was depressed) with an internal positive control (the other excurrent nasal flap elevated). Specimen BMNH 1948.8.6.196 was also larger than BMNH 1983.7.6.12 (*TL* 18 cm *v.* 13 cm, respectively), which meant that the free-stream speed employed for the dye visualisation experiments was within the range of swimming speeds *A. felis* may adopt (Section 2.6). Furthermore, the mouth of BMNH 1948.8.6.196 was partially open (Fig. A.1C, white disk, Appendix A.4), reflecting the normal behaviour of the mouth in the aquarium specimens (Fig. 5A and B).

The scan of BMNH 1983.7.6.11 and the scan of BMNH 1948.8.6.195 were of insufficient quality to convert into models for fluid dynamics experiments. We did, however, use these two scans (after converting them to surface models, Section 2.4) to support our observations on the nasal anatomy of *A. felis*. The excurrent nasal flaps of specimen BMNH 1983.7.6.11 were both depressed. The excurrent nasal flaps of specimen BMNH 1948.8.6.195 were both

elevated and its mouth was wide open. We did observe the aquarium specimens opening their mouths to this extent, but this was not normal behaviour.

2.4. Surface models

Surface models of the heads of BMNH 1983.7.6.11-12 and BMNH 1948.8.6.195-196 (Fig. 6; see also Fig. A.3, Appendix A.4) were generated with the image processing software ScanIP (Synopsys, Mountain View, USA) as previously described (Garwood et al., 2019, 2020). Further details of the surface models are given in Appendix A.1.2. Selected surface models are available to download as stereolithography (STL) files (Cox et al., 2021).

2.5. Plastic models

The plastic models of the heads (Fig. 7; see also Fig. A.4, Appendix A.4 and Table 1) were either 5.5x (Models 1A and B) or 3.7x (Models 2A and B) life size. The plastic models were larger than life (and as large as they could be without their maximum transverse cross-sectional area exceeding 5 % of the flume's cross-sectional area; Appendix A.1.5.1) to allow us to see dye behaviour in the nasal region and to detect any passage of dye through the olfactory sensory channels (Section 2.6). Observation of dye behaviour was facilitated by choosing an appropriate colour or plastic for each model: off-white gave good contrast with red dye; black gave good contrast with green fluorescent dye; and translucent plastic facilitated dye visualisation in the nasal chamber. We used two versions of Model 1 (Table 1): Model 1A (off-white, with a translucent right nasal region; Fig. 7A, Tr) and Model 1B (black; Fig. 7B and C). We chose the right nasal region for the translucent part because: a) the lateral edge of Model 1A's excurrent nasal flap was not bent back, as it was in the left nasal region (Fig. 6C, ellipse); and b) Model 1A would be upright when observed from the flume's most convenient viewing face (Fig. A.7A, arrow *a*, Appendix A.4). We used two versions of Model 2: Model 2A (off-white; Fig. A.4A and B, Appendix A.4) and Model 2B (black; Fig. A.4C, Appendix A.4). Model 2A had flexible barbels (Fig. A.4A and B, Appendix A.4). Model 2B had either truncated barbels or no barbels (Fig. A.4C, Appendix A.4). Fabrication and assembly of the models are described in Appendix A.1.3.

2.6. Dye visualisation

Dye visualisation was performed in an Eidetics Model 1520 closed-circuit, free-surface, continuous-flow flume (Wang et al., 2007) using the plastic models of the sea catfishes'

heads. To obtain a well-defined dye filament, the flume was operated at a free-stream speed of 5 cm s^{-1}. This speed corresponded to Reynolds numbers of 600 – 800 for both Models 1 and 2 (Table 1 and Section 2.9.2), a range indicative of laminar flow (Vogel, 1994, pp. 84-85). According to the principle of dynamic similarity (Shapiro, 1961, p. 74; Vogel, 1994, p. 102), a free-stream speed of 5 cm s^{-1} with Model 1 (5.5x life size) corresponds to a free-stream speed of 27.5 cm s^{-1} for the actual specimen, or 2.1 *TL* s^{-1} (*TL* = 13 cm; Section 2.1). A free-stream speed of 2.1 *TL* s^{-1} is just above the upper limit of the range of swimming speeds (0.3 – 1.9 *TL* s^{-1}) observed in the aquarium specimens (Appendix A.1.4). A speed of 5 cm s^{-1} with Model 2 (3.7x life size) corresponds to a free-stream speed of 18.5 cm s^{-1} for the actual specimen, or 1.0 *TL* s^{-1} (*TL* = 18 cm; Section 2.1). A free-stream speed of 1.0 *TL* s^{-1} is within the range of swimming speeds observed in the aquarium specimens (Appendix A.1.4).

The pitch and yaw angles (Fig. 10.1 of Barnard and Philpott, 2004) of the plastic models were 0 ± 10°. Roll angles (ibid.) are specified in the legends for the video clips (Video, Supplementary data). Pitch angles were within the range observed in the aquarium specimens (+ 70° to - 90°; Appendix A.1.4). Yaw angles matched those observed in the aquarium specimens (Appendix A.1.4). Flow was visualised with either red food dye diluted in a ratio of four parts water to one part dye (off-white/translucent models; Abel et al., 2010) or a 0.4 mM aqueous solution of rhodamine 6G, a green fluorescent dye (black models; Agbesi et al., 2016a, 2016b). The solution of rhodamine 6G was neutrally buoyant. The water temperature in the flume varied between 10 – 18 °C, and changed by ≤ 2.0 °C in a single day. Dye visualisation experiments were recorded on a Panasonic HC-V500 digital camcorder (50 frames s^{-1}, 1920 pixels x 1080 pixels per frame) mounted on a Velbon DV-7000 tripod fitted with a Vel-flo 9 PH-368 head. In one instance (Video clip 9) the camcorder was hand-held. Footage was analysed using the software Adobe Premiere Pro CC. Further details of the dye visualisation experiments are given in Appendix A.1.5.1.

2.7. Computational fluid dynamics

2.7.1. Model

Computational fluid dynamics simulations of olfactory flow in the sea catfish were done on a life-sized model of the head of BMNH 1983.7.6.12 (Model 1C, Table 1; Cox et al., 2021). To create this model, we fused the high-resolution STL model of the right nasal region of this

specimen to the low-resolution STL model of its head (Appendix A.1.5.2.1). The fusion was seamless: there was no detectable joint between the two parts in the model of the complete head (Fig. A.13A, Appendix A.4). Because the right nasal region was at a higher resolution than the left nasal region (pixel spacings 16 μm and 33 μm, respectively; Appendix A.1.2.1), analysis of the CFD simulations focused primarily on the right nasal region. We did, however, compare results from the right nasal region with those from the left.

Prior to the CFD simulations, we made three further modifications to the model. The first two are detailed in Appendix A.1.5.2.1, the third in Garwood et al. (2019). The first modification was to remove the lateral line canals (Fig. 3A, circle; Fig. 6.2A of Helfman et al., 2009). We did so to stop flow through them. *In vivo*, the canals would be filled with a viscous fluid (Kasumyan, 2003), and therefore there would be no flow of water through them.

The second modification was to the olfactory rosettes. Generally, the lamellae of both the left and the right olfactory rosettes of the model were uniformly spaced (Fig. 8B), as they were in the preserved specimen from which the model was derived (Fig. 2) and in the other preserved specimens that we inspected. The olfactory lamellae also appear uniformly spaced in Fig. 3 of Zeiske et al. (1994). Consequently, the olfactory rosettes of the model are likely to be accurate representations of the olfactory rosettes *in vivo*. There were, however, four types of aberration in the olfactory rosettes: 1) a hole in the lamellar attachment to the wall of the nasal chamber (Fig. A.8, Appendix A.4); 2) a bridge between two adjacent lamellae (Fig. A.9, Appendix A.4); 3) a gap in the lamellar attachment (Fig. A.10, Appendix A.4); and 4) lamellar tips that were both bridged and bent (Fig. A.11, Appendix A.4). The aberrations were caused by either: a) the anatomical feature not being well-resolved (holes/gaps) by the image processing that gave rise to the surface model (Section 2.4); b) the presence of residual preservative fluid in the nasal chamber during the micro-CT scan (bridges); or c) a postmortem change in the specimen (bridged/bent lamellar extensions). All four types of aberration were corrected to improve further the anatomical accuracy of the olfactory rosettes. In short, the olfactory rosettes of the CFD version of Model 1 were improved versions of the dye visualisation versions of Model 1.

The third modification was the addition of a tapered extension (‘tail’) to the back of the model. The tail was 5.6x the length of the head and had a 7° taper (Fig. A.12, Appendix A.4).

We added the tail to reduce any modification to upstream flow due to the lack of a body (Abel et al., 2010).

2.7.2. Simulations

Simulations were run with the software OpenFOAM (Weller et al., 1998). The CFD mesh used for the simulations comprised ~ 24 million cells. The surface of this mesh was refined in the nasal region (Fig. 8A), where the prescribed cell edge length was typically 7.8 μm. Adjacent to the surface of the nasal region, the mesh comprised five layers of cells, each with a prescribed thickness of typically 2.6 μm (Fig. 8C). The thickness of these cells was sufficient to capture the velocity gradients here. The number of cells across the sensory channel was ~ 15 – 35 (e.g. Fig. 8B). The density and dynamic viscosity were set to 999.3 kg m^{-3} and 1.2 x 10^{-3} Pa s (values for fresh water at 14 °C). Simulations were run at inlet velocities of 6.5, 13 and 27.5 cm s^{-1}, corresponding to swimming speeds of 0.5, 1.0 and 2.1 *TL* s^{-1} and Reynolds numbers of 200, 300 and 700, respectively (Section 2.9.3). Thus the largest Reynolds number fell in the range of Reynolds numbers used for Model 1 in the dye visualisation experiments (600 – 800; Section 2.6). Pitch and roll angles were 0°; yaw angles were 0 ± 10° (positive and negative pitch and yaw angles are indicated in Fig. 6A and 6B, respectively). Flow was assumed to be steady, laminar (Section 2.6), isothermal, and incompressible. The assumption of steady flow was based on a transient simulation. In the transient simulation, the volumetric flow rate in a plane of refined cells through each nostril of each nasal region (Fig. A.13, Appendix A.4) was found over the last 4 s of the simulation to vary by ≤ 0.0007 % of the average volumetric flow rate in each plane over that time period (Fig. A.14, double-asterisked line, Appendix A.4). Velocities and static pressures in the steady CFD simulations were the averages of the last 500 iterations from a total of 1995 iterations of a converged, time-averaged solution to the Navier-Stokes equations. Convergence was checked by monitoring the volumetric flow rate through the nostril planes (above). Because the volumetric flow rate through these planes changed by ≤ 0.0015 % over the last 500 iterations of the simulations, we assumed convergence had occurred. Results from the steady CFD simulations were analysed and visualised with ParaView (Ayachit, 2016). Because flow was steady, the streamlines generated in ParaView equate to pathlines (Kline, 1972), and therefore indicate the path a fluid particle takes (Barnard, 2009, p. 6). Further details of the CFD simulations are given in Appendix A.1.5.2.

2.7.3. Pressure

Static pressures are expressed as pressure coefficients (*Cp*; Douglas et al., 1985, p. 318; Vogel, 1988), i.e. the ratio of the difference in static pressure (P - P_0) to the dynamic pressure of the free-stream flow ($\frac{1}{2}\rho U_0^2$):

$$C_p = \frac{P - P_0}{\frac{1}{2}\rho U_0^2}$$

Equation 1

where P is the static pressure at a given point, P_0 is the ambient static pressure of the fluid (set to zero in the CFD simulations), ρ is the density of the fluid (999.3 kg m^{-3}; above), and U_0 is the free-stream speed (inlet velocity = 6.5, 13 or 27.5 cm s^{-1}).

The percentage of the dynamic pressure of the free-stream flow harnessed by the nasal region was calculated using the expression 100 x [C_p (Incurrent nostril) – C_p (Excurrent nostril)], where C_p (Incurrent nostril) and C_p (Excurrent nostril) are the average pressure coefficients for the fluid in the incurrent and excurrent nostrils, respectively.

Details of how we located points of static pressure on the surface of the CFD model and of how we calculated the average static pressure in each nostril are given in Appendix A.1.5.2.3.

2.7.4. Boundary layer

We gauged the thickness of the boundary layer on the surface of the CFD model using vorticity (Abernathy, 1972; Thwaites, 1960, p. 18), according to Garwood et al. (2020). We defined the thickness of the boundary layer using a vorticity of 50 s^{-1} and the methodology described in Appendix A.1.5.2.5.

2.8. Morphometry

Morphometric measurements (e.g. nasal chamber volumes) were made using ParaView, Rhinoceros (Version 4.0, Robert McNeel & Associates), and ScanIP, according to previous methodology (e.g. Garwood et al., 2019, Appendix A.1.5). Morphometric measurements were made on both the left and right nasal regions.

313 *2.9. Reynolds numbers*

314

315 *2.9.1. General*

316 Reynolds numbers (*Re*) for olfactory flow were calculated using either Equation 2 (Vogel,
317 1994, p. 85) or Equation 3 (Holmes et al., 2011):

318

319 $$Re = \frac{UL\rho}{\mu}$$

320 Equation 2

321

322 $$Re = \frac{4Q\rho}{L\mu}$$

323 Equation 3

324

325 where U is the speed of the fluid, L is the characteristic dimension of the object, μ is the
326 dynamic viscosity of the fluid, and Q is the volumetric flow rate. For external olfactory flow,
327 U was the free-stream speed (U_0), and L was the width of the nasal region in dorsal profile,
328 normal to the direction of flow (Fig. 9C). For internal olfactory flow, L was the wetted
329 perimeter of the nasal chamber (Fig. 8D, WP). Reynolds numbers are given to one significant
330 figure and, unless stated otherwise, refer to *external* olfactory flow.

331

332 *2.9.2. Reynolds numbers for dye visualisation*

333 The Reynolds numbers for olfactory flow in the dye visualisation experiments were
334 calculated (Equation 2) with U_0 = 5 cm s^{-1} (the free-stream speed in the flume; Section 2.6), L
335 = 16 mm (Model 1) or 15 mm (Model 2), ρ = 998.6 – 999.7 kg m^{-3}, and μ = 1.31 – 1.06 x 10^{-3}
336 Pa s at 10 – 18 °C (water temperature in the flume; Section 2.6).

337

338 *2.9.3. Reynolds numbers for CFD*

339 Calculations of Reynolds numbers for olfactory flow in the CFD simulations used the values
340 of speed (inlet velocity), density, and dynamic viscosity given in Section 2.7.2. Reynolds
341 numbers for external olfactory flow were calculated (Equation 2) with L = 2.9 mm. Reynolds
342 numbers for flow through the right nasal chamber (i.e. internal flow) were calculated (Equation
343 3) with Q = 12 mm^3 s^{-1} (U_0 = 6.5 cm s^{-1}), Q = 37 mm^3 s^{-1} (U_0 = 13 cm s^{-1}), Q = 106 mm^3 s^{-1}
344 (U_0 = 27.5 cm s^{-1}) and L = 9.7 mm. Reynolds numbers for flow through the left nasal chamber

were calculated (Equation 3) with Q = 12 mm^3 s^{-1} (U_0 = 6.5 cm s^{-1}), Q = 41 mm^3 s^{-1} (U_0 = 13 cm s^{-1}), Q = 121 mm^3 s^{-1} (U_0 = 27.5 cm s^{-1}) and L = 8.8 mm. Volumetric flow rates were determined according to Appendix A.1.6 and are quoted to two significant figures.

2.10. Figures and video clips

In keeping with our previous work (Garwood et al., 2019, 2020), the figures (including those in Appendix A.4) and video clips (Video, Supplementary data) are shown in the same orientation, with the anterior part of the head or nasal region to the left. In dorsal views, the lateral part of the head is always uppermost. Some images in the figures have been flipped horizontally or vertically. In these cases, the designation of the anatomical aspect shown, left or right, is italicised (e.g. *right* nasal region). Superior views are those normal to the nasal region. Copyright of the images of the specimens belongs to the Natural History Museum, London, UK.

3. Results

3.1. Nasal anatomy

The nasal anatomy of the preserved specimens generally agrees with previous descriptions of *Ariopsis felis*'s nasal anatomy (Caprio, 1980; Zeiske et al., 1994), and with our observations of the aquarium specimens of *A. felis* (Section 2.2).

The paired nasal regions of *A. felis* are situated on the anterior part of its head (Fig. 6B, NR). Each nasal chamber is linked to the external environment by an incurrent nostril and an excurrent nostril (Fig. 9A, IN and EN). The incurrent nostril faces oncoming external flow (Fig. 9A, arrow 1). The incurrent nostril has a lateral extension, which we refer to as the incurrent nasal flap (Fig. 10A, asterisk). The excurrent nostril faces dorsolaterally (Fig. 6C, arrow), approximately normal to oncoming flow (Fig. 9A, arrow 2). Its area is twice that of the incurrent nostril. The excurrent nostril is bounded by a single flap, split caudally (Fig. 10B and C, yellow asterisk). For convenience we treat this flap as three separate flaps – one large anterior flap, which we refer to as the excurrent nasal flap (Fig. 10B, EF), and two small flaps, which we refer to as the lateral excurrent nasal flap and the medial excurrent nasal flap (Fig. 10B, LF and MF, respectively). The excurrent nasal flap was either elevated (Fig. 10B) or depressed (Fig. 10C, EF*) in the preserved specimens we inspected. If depressed, it formed a complementary interaction with the lateral and medial excurrent nasal flaps, leaving only a small gap (Fig. 10C, Gp). Therefore, as noted by Caprio (1980), when depressed the excurrent nasal flap covers almost completely the excurrent nostril.

The nasal chamber is compact, with a volume of 6 – 24 mm^3. It has a large medial recess (Figs. 11A, MR) and a small lateral recess (Fig. 11A, LR). The medial and lateral recesses were present in all the specimens of *A. felis* that we inspected (Fig. A.16, Appendix A.4). The floor of the nasal chamber is inclined to the body axis (Fig. 11B; $\alpha = 40 – 65°$) and is occupied by 32 – 44 olfactory lamellae (Figs. 11B and 12, La) arranged in a pinnate fashion around a central raphe (Fig. 11A, green dashed line). We refer to the lamellar array as the olfactory rosette (Fig. 2C). The incurrent and excurrent nostrils lie above the anterior and posterior parts of the olfactory rosette, respectively (Fig. 11C). The olfactory epithelium is located on the surface of the olfactory lamellae (Zeiske et al., 1994). Most lamellae have a tip (Figs. 11B and 12, Tp). A peripheral channel lies between the lamellar tips and the wall of the

nasal chamber (Fig. 11A, black dashed line). The proximal dorsal edge of each lamella (Fig. 11B, yellow arrowhead) is broad, whilst each distal lamellar edge, which forms the attachment to the wall of the nasal chamber, is thin (Fig. 11B, white arrowhead). The lamellae create 33 – 45 sensory channels (Fig. 11B, SC).

3.2. Dye visualisation

Using dye visualisation, we established that flow of water through the nasal chambers of the plastic models of two different specimens of *A. felis* could be induced by the free-stream flow (Fig. 13A-C; Video clips 1 – 4). These models included the model with the barbels (Video clip 3). Flow through the nasal chamber was induced at Reynolds numbers of 600 – 800 and at pitch and yaw angles of 0 ± 10°. We observed that:

1) Dye fanned in front of the incurrent nasal flap (Fig. 13D, Video clip 5). Such behaviour indicated that flow was decelerating and therefore that the incurrent nasal flap was a region of relatively high static pressure (Shapiro, 1972).

2) Dye entered the nasal chamber via the incurrent nostril, and exited via the excurrent nostril, confirming the roles of these two apertures (Fig. 13B; Video clip 2).

3) Generally, the dye filament passed intact into the incurrent nostril (Video clips 1 – 4).

4) After entering the incurrent nostril, the dye filament could be deflected medially within the nasal chamber (Fig. 13E; Video clip 6).

5) Dye passing out of the excurrent nostril demonstrated a variety of behaviours, depending on the exit point. For example, dye passing out of the anterior part of the excurrent nostril did so as a vortex (Video clip 3; Lugt, 1983).

Importantly, we also established unequivocally that external flow could induce a flow of water *through* the *olfactory sensory channels*, specifically those of Model 1 (Fig. 13F; Video clips 7 – 9). We observed dye passage through the sensory channels at Reynolds numbers of 600 – 800, and at pitch angles of 0 ± 10° (e.g. Video clips 7 and 8) and yaw angles of 0 ± 10° (e.g. Video clips 7 and 9). Dye passage was observed through both the lateral sensory channels (channels 21 – 26; Fig. 13F, and Fig. A.17, Appendix A.4; Video clips 7 – 9) and

through the medial sensory channels (channels 8 – 11; Fig. A.17, Appendix A.4; Video clips 8 and 9). We observed dye passage through up to five (Fig. 13F), and possibly six (Video clip 8), sensory channels at once. We also observed dye dispersing *over* the sensory channels (Video clip 9).

Using Model 2, we showed that dye still passed through the nasal chamber when the excurrent nasal flap was depressed, albeit at a reduced rate (Video clip 10). This dye passed through the gap between the three excurrent nasal flaps (Fig. 10C, Gp). Using the same model, a dye filament directed at the nasal region with the elevated excurrent nasal flap passed through the nasal chamber normally (Video clip 3), showing that the reduced rate was due to the depressed nasal flap.

Four other notable types of dye behaviour were: 1) unimpeded flow through the nasal chamber in the presence of a flexible lateral barbel (Video clip 3); 2) a vortex on the dorsal edge of the incurrent nasal flap (Fig. 13G, asterisk; Video clip 11); 3) a vortex on the external face of the lateral excurrent nasal flap (Fig. 13H, asterisk; Video clip 12); 4) recirculation of dye dorsal to a truncated lateral barbel (Video clip 13); and 5) a vortex in the open mouth of Model 2 (Video clip 14).

3.3. Computational fluid dynamics

3.3.1. General

The results from the CFD simulations were consistent with the dye visualisation experiments, indicating that the CFD results were valid. For example, dye behaviour in the flume could be replicated by streamlines generated from the CFD simulations (Fig. 13), including: 1) the overall route taken by olfactory flow (Fig. 13A-C); 2) flow fanning prior to the incurrent nasal flap (Fig. 13D); 3) the medial route through the nasal chamber taken by flow entering the incurrent nostril (Fig. 13E); 4) a vortex on the dorsal edge of the incurrent nasal flap (Fig. 13G, asterisk); and 5) a vortex on the external face of the lateral excurrent nasal flap (Fig. 13H, asterisk).

Additionally, the CFD simulations showed that:

1) The model's stagnation point was located on either the incurrent nasal flap or the excurrent nasal flap (Fig. 14A and B, white disks; see also Fig. A.18, Appendix A.4). At non-zero yaw angles the stagnation point could shift from one nasal region to the other. Specifically, and as expected, the stagnation point could shift to the nasal region that met directly oncoming flow. The stagnation point was never located on the rostral tip. The rostral tip was, however, in a region of high pressure (Fig. 14A).

2) 48 – 51 % of the dynamic pressure of the external flow was harnessed by the right nasal region and 36 – 43 % by the left.

3) Flow accelerated as it passed over the excurrent nostril (Fig. 15, region within dashed line).

4) The anterior part of the nasal chamber floor was a region of relatively high static pressure (Fig. 16A).

5) Flow decelerated as it approached the nasal chamber floor (Fig. 16B).

6) Within the olfactory rosette, the raphe, or the dorsal edge of one of the anterior lamellae, had the greatest static pressure (Fig. 16A, white disk; see also Fig. A.19, Appendix A.4).

7) Streamlines impinging on the anterior part of the olfactory rosette were dispersed over the floor of the nasal chamber (Fig. 16).

8) Some of the dispersed streamlines passed through the sensory channels (Fig. 16A). How they passed through the sensory channels is described in detail in Section 3.3.2.

9) Streamlines leaving a sensory channel could either: a) pass directly out of the excurrent nostril (Fig. 16C, Streamline Y); or b) re-enter another sensory channel (Fig. 16C, Streamline X and inset). Passage from the sensory channel and into the excurrent nostril could be aided by the tips of the olfactory lamellae (Fig. 16C, yellow disks and Streamline X).

10) The nasal region – including the incurrent and excurrent nasal flaps – remained within the boundary layer (Fig. 15; see also Figs. A.21 and A.22, Appendix A.4).

11) Reynolds numbers in the nasal chamber were 4 – 50.

12) The volumetric flow rate through the nasal chamber was 10 – 120 $mm^3 s^{-1}$.

The Reynolds numbers in the nasal chamber and volumetric flow rate increased with increasing external Reynolds number, but the percentage dynamic pressure harnessed by the nasal region *de*creased with increasing external Reynolds number.

3.3.2. Dispersal of olfactory flow

Streamlines impacting on the anterior part of the olfactory rosette could enter the sensory channels either directly (Figs. 17A-C and 18A-C) or indirectly (Figs. 17D-F and 18D-F). By 'indirectly' we mean that a streamline passes first through *another* sensory channel (or channels).

Direct entry was via either the proximal (Fig. 18A and B, pr) or distal part of a sensory channel (Fig. 18C, di). Streamlines directly entering the distal part of a sensory channel did so via the medial recess (Fig. 18C, MR). Direct entry could occur in most, but not all, sensory channels (Fig. 17A-C). The number of sensory channels in which direct entry occurred varied with Reynolds number; the greatest number occurred at the largest Reynolds number (700; Fig. 17C). At every Reynolds number, direct entry occurred in most lateral sensory channels and at least the first seven medial sensory channels (Fig. 17A-C).

Indirect entry into a sensory channel typically occurred in the posterior half of the olfactory rosette, and always in a) the central medial channels, and b) the most posterior lateral channels (Fig. 17D-F). Indirect entry could occur in two main ways (Fig. 18D-F):

1) Indirect entry into a medial sensory channel (e.g. sensory channel 12 in Fig. 18D) could occur after a streamline had passed through an anterior medial channel (e.g. sensory channel 2 in Fig. 18D). In this case, passage into the medial channel occurred via either the medial recess (Fig. 18D and F) or the peripheral channel (Fig. 18E).

2) A streamline leaving a medial sensory channel could pass into either a) a lateral channel (e.g. sensory channel 12 to sensory channel 21 in Fig. 18D) or b) another medial channel (e.g. sensory channel 12 to sensory channel 14 in Fig. 18F).

At higher Reynolds numbers (300 and 700), indirect entry into a medial sensory channel could result in a vortex within that channel (Fig. 19A, Vo).

A streamline could pass through one, two, three, or four sensory consecutive channels (Fig. 18B, C, D and F, respectively). The number of sensory channels involved in inter-channel olfactory resampling (i.e. where a streamline passed through consecutive sensory channels; Section 4.5) was the same at the two lower Reynolds numbers employed in the simulations (200 and 300), but decreased markedly at the highest Reynolds number (700; Fig. 17 and Table 2). Fig. 18G-I shows the tendency for inter-channel olfactory resampling to decrease with increasing speed. At the lowest Reynolds number (200), all streamlines pass through three channels (Fig. 18G). At the intermediate Reynolds number (300), only two streamlines pass through three channels (Fig. 18H, arrowheads). At the highest Reynolds number (700) no streamlines pass through three channels (Fig. 18I). The number of unique paths streamlines took during inter-channel olfactory resampling also decreased markedly at the highest Reynolds number (Table 2).

Flow behaved similarly in the right and the left nasal regions (Fig. 20). For example, at a Reynolds number of 300, streamlines passing through channel 12 subsequently passed through several posterior channels (right nasal region: 14, 15, 18 – 21; left nasal region: 16, 18 – 20), having passed first through channel 2 in the right nasal region (Fig. 20A) and channels 2 or 3 in the left (Fig. 20B).

Similarly, yaw had only a minor effect on the route taken by streamlines through the sensory channels. For example, at a yaw angle of 0° (Reynolds number 200) streamlines passing through channel 5 subsequently passed through channel 9, and then through channels 18 – 23 (Fig. 18K); streamlines take essentially the same route at yaw angles of ± 10° (Fig. 18J and L).

4. Discussion

In the following discussion, comparisons are made with several different fishes. Figure 21 shows the classification of these fishes, and notes the features relevant to olfactory flow.

4.1. Olfactory flow in the sea catfish is induced by an external flow

Using dye visualisation, we showed that flow of water through *both* the nasal chamber *and* the olfactory sensory channels of the sea catfish *Ariopsis felis* can be induced by an external flow at Reynolds numbers of 600 – 800. *In vivo*, the origin of the external flow would usually be the movement of the sea catfish as it swims forward, because *A. felis* is 'an almost permanent swimmer' (Zeiske et al., 1994; Appendix A.1.4). For a resting sea catfish, the source of the external flow may be an environmental water current, or one of the other mechanisms mentioned in Section 4.4.

4.2. Factors determining externally-induced olfactory flow

Externally-induced flow through the nasal chamber of *A. felis* may be attributed to:

1) The location of the incurrent nostril on the blunt anterior surface of the head, in a region of relatively high static pressure ($Cp > 0$; Fig. 14). The relatively high static pressure in this region will force flow into the nasal chamber.

2) The incurrent nasal flap impeding external flow and deflecting it into the nasal chamber. Indeed, so effectively does the incurrent nasal flap impede flow that in five of the nine CFD simulations it was the stagnation point for the entire model (Fig. A.18E-I, Appendix A.4). We note, however, that in the preserved specimens the nasal flap was not rigid, and so may be bent back when a sea catfish swims forward.

3) The excurrent nostril lying normal to the external flow (Fig. 9, arrow 2). As a result, the fluid within the excurrent nostril should experience only the ambient static pressure of the external flow (Vogel, 1994, p. 60), thereby creating a positive pressure difference across the nostrils. In fact, the static pressure of the fluid within the excurrent nostril was very close to ambient static pressure ($Cp \sim 0 – 0.2$).

4) Viscous entrainment (Cox, 2008). Fluid may be drawn out of the nasal chamber by the tractive viscous forces applied to it by external flow passing directly over the excurrent

nostril (Fig. 9, large arrow). The effect of the excurrent nasal flap, which protrudes from the surface of the head (Fig. 15, EF, inset), is to accelerate flow in this region (Fig. 15, region within dashed line), thereby increasing these tractive viscous forces.

The percentage of the dynamic pressure of the free-stream flow harnessed by the right nasal region (48 – 51 %) was greater than the left (36 – 43 %). The difference may be attributed to the lateral edge of the excurrent nasal flap being folded back (Fig. 6C, ellipse), and therefore not being as effective at accelerating flow as the excurrent nasal flap of the right nasal region.

4.3. Regulation of olfactory flow

Visual inspection of the preserved specimens showed that the excurrent nasal flap is elevated or depressed (Fig. 4; Section 3.1). When depressed, the excurrent nasal flap forms a complementary interaction with the two smaller excurrent nasal flaps (Fig. 10C). In this depressed state there is, however, a small gap between all three excurrent nasal flaps (Fig. 10C, Gp). In the aquarium specimens, there was a degree of mobility in the excurrent nasal flap. This mobility coincided with the specimens' movements and could take various forms. Most notably, the excurrent nasal flap could be deflected down with fast forward movement of a specimen, or when the specimen turned, or when it flicked its lateral barbel. After these movements, however, the excurrent nasal flap returned to its elevated state. The excurrent nasal flap was always elevated in resting specimens. Dye visualisation with a plastic model showed that water still flowed through the nasal chamber when the excurrent nasal flap was depressed, albeit at a reduced rate (Video clip 10). The reduced flow passes through the gap between the three excurrent nasal flaps (Fig. 10C, Gp).

These observations, together with those of Caprio (1980), suggest that the sea catfish's movements control the position of the nasal flap. The position of the nasal flap in turn controls the flow of water through the nasal chamber. When elevated, there is significant flow through the nasal chamber. When depressed, there is reduced flow through the nasal chamber. This regulatory mechanism presumably protects the delicate nasal structures from damage at faster swimming speeds. Other fishes also have, or appear to have, mechanisms for regulating flow through their nasal chambers (Døving et al., 1977; Zeiske et al., 1986; Abel et al., 2010; Howard et al., 2013), but all are distinct from that of the sea catfish, and indeed from each other. Thus, there are different ways of regulating olfactory flow in fishes.

4.4. Other mechanisms that may generate olfactory flow

Flow through the sea catfish's nasal chamber may also be generated by:

1) Respiratory flow, i.e. when water is drawn into the mouth during respiration. The incurrent nostril of the sea catfish is directly above the mouth (Fig. 1B). We observed regular mouth movements in the aquarium specimens when they were either swimming or resting, as well as some irregular ones (e.g. 'yawning' and 'gulping'). Although these movements may not be enough to stimulate a continuous flow of water through the nasal chamber, they may at least draw water towards the incurrent nostril. There is precedent for this type of action (Pfeiffer, 1968) in a resting bichir (Fig. 21; Polypteridae; Nelson, 2006, p. 89;).

2) Movement of the barbels. Burne (1909) showed that skeletal movements associated with the movement of the lateral barbel may produce a current of water through the nasal chamber of the North African catfish, *Clarias gariepinus* (Clariidae; Nelson, 2006, p. 180; Burne refers to *Clarias gariepinus* as *Clarias lazera,* and to the lateral barbel as the maxillary tentacle). They do so by compressing and dilating the accessory sac (a distinct chamber within the nasal region, but separate from the chamber in which the olfactory rosette is housed). Although the sea catfish does not have a recognisable accessory sac, the base of its lateral barbel lies adjacent to the nasal region (Fig. 1B, blue arrowhead), and the lateral barbel's (voluntary) movement may stimulate a water current in the nasal chamber, although perhaps not one that results in a continuous flow of water. We observed in the aquarium specimens a variety of voluntary lateral barbel movements that may have caused such non-directional water currents (Fig. 5D – G). The lateral barbel movements occurred whilst the specimens were either swimming forwards (Fig. 5 D – G) or resting. It is very unlikely that movement of the sea catfish's two pairs of ventral barbels (Fig. 5, outlined in red) will stimulate a water current in the nasal chamber, given that these barbels are remote from the nasal chamber (Fig. 1B and C).

3) Co-ordinated beating of the non-sensory cilia (Reiten et al., 2017) on the olfactory lamellae (Zeiske et al., 1994). The non-sensory ciliated cells are not uniformly distributed on the surface of the sea catfish's olfactory lamellae (Fig. 4 of Zeiske et al., 1994). The scattered nature of these cells suggests that their cilia are not (*pace* Caprio, 1980) able to generate a continuous water current through the olfactory sensory channels (if indeed the cilia are water-

propelling; Cox, 2013), although they might be able to generate a localised current. In any case, our inanimate models did not allow us to investigate ciliary-driven flow.

In summary, although it seems unlikely that movements of the mouth, barbels, or non-sensory cilia could generate a coherent water current through the nasal chamber and its sensory channels, one or more of these types of movement could generate a sporadic water current. The latter may be advantageous to olfaction when the sea catfish is resting (Section 4.1).

4.5. Dispersal of olfactory flow

Dispersal of olfactory flow in the sea catfish may involve up to four stages (Fig. 22). In the first, incurrent flow is dispersed when it impacts on the anterior olfactory rosette in a jet impingement-like mechanism (Fig. 22, white disks; Garwood et al., 2019, 2020). As a result of the impact, the anterior part of the nasal chamber floor is a region of relatively high static pressure (Fig. 16A). The magnitude of the impact, and therefore the degree of dispersal, will be enhanced by the fact that the floor of the nasal chamber is inclined to oncoming flow (Fig. 9B, α), because the hydrodynamic force exerted by the fluid on the floor is proportional to $\cos \alpha$ (Massey, 1989, pp. 117-118).

In the second stage of dispersal (Fig. 22, yellow rounded rectangles), flow enters a medial sensory channel. Flow may be deflected into the medial sensory channel by the broad proximal dorsal edge of each lamella (Fig. 11B, yellow arrowhead). Alternatively, flow may be guided *directly* into the medial sensory channel by the medial recess (Fig. 22A, MR).

The third and fourth stages of dispersal involve olfactory resampling. Olfactory resampling is when flow encounters the olfactory sensory surface more than once (Garwood et al., 2020). The third stage of dispersal is *inter*-channel olfactory resampling (Fig. 22, red and blue rounded rectangles). In this stage, flow is resampled when it passes through two to four consecutive olfactory sensory channels via multiple pathways (Table 2). Three such pathways are shown in Fig. 22A-C. Inter-channel olfactory resampling may be mediated either by the medial recess (Fig. 22B), or by the peripheral channel (Fig. 22C, PC). In both cases, flow passes through an anterior sensory channel first (Fig. 22B and C, yellow rounded rectangles). Inter-channel olfactory resampling is more extensive at the two lower Reynolds numbers

692 employed in the CFD simulations (200 and 300; Table 2), which correspond to swimming
693 speeds of 0.5 and 1.0 *TL* s^{-1}. Thus, inter-channel olfactory resampling is likely to be more
694 effective at lower swimming speeds, and indeed the mean swimming speed of the aquarium
695 specimens (0.6 *TL* s^{-1}; Appendix A.1.4) lay between the two aforementioned values. It is also
696 possible that the reduced inter-channel olfactory resampling at the highest Reynolds number
697 (700), which corresponds to a swimming speed of 2.1 *TL* s^{-1}, coincides with the depression of
698 the excurrent nasal flap (Section 4.3). (We were not able, from our observations of the
699 aquarium specimens, to determine the swimming speed at which the excurrent nasal flap
700 became depressed.)
701
702 The fourth stage of dispersal is *intra*-channel olfactory resampling (Fig. 22C). This stage
703 occurs at higher Reynolds numbers (300 and 700), and involves a vortex in the superior part
704 of a medial sensory channel (Fig. 22C, undulating red line). Vortices may achieve olfactory
705 resampling by bringing repeatedly the same fluid particle into contact with the olfactory
706 sensory surface (Garwood et al., 2020). In the sea catfish, the repeated contact occurs within
707 a single sensory channel. Formation of vortices in the interstices of a regular array of
708 protrusions at moderate Reynolds numbers ('interactive flow'; Fig. 8.7b of Vogel, 1994)
709 occurs in other biological contexts (Vogel, 1994, pp. 171-173).
710
711 Combined, the four stages of dispersal should ensure thorough olfactory sampling. Thorough
712 sampling, together with the extensive sensory surface area of the sea catfish's olfactory
713 rosette (20 mm^2 for specimen BMNH 1983.7.6.12; Appendix A.1.7), should in turn increase
714 the chances of capturing odorant molecules, and should therefore improve the sea catfish's
715 olfactory sensitivity. Caprio (1980) found that the sea catfish had electrophysiological
716 thresholds of 10^{-7} to 10^{-8} M to certain amino acids, suggesting reasonable olfactory sensitivity
717 (cf. olfactory sensitivity of the European eel: 10^{-15} to 10^{-18} M; Section 4.9).
718
719 *4.6. Olfactory flow in other sea catfishes*
720 The nasal anatomy of other species of sea catfishes, e.g. *Galeichthys feliceps*, is like that of *A.*
721 *felis* (Figs. 21 and 23). We would therefore expect olfactory flow in *G. feliceps* to behave in a
722 similar way to that in *A. felis*. We note, however, that the incurrent flap in *G. feliceps* (Fig.
723 23, asterisk) is not as extensive as it is in *A. felis*. The incurrent nostril of *G. feliceps* does,
724 however, have a pronounced lateral incurrent wall (Fig. 23, inset, black disk), and we would

expect this wall to act as the anatomical element that impedes oncoming flow, deflecting it into the nasal chamber, as in the sturgeon (Section 4.7; Garwood et al., 2019).

4.7. Common elements in the olfactory flow of the sturgeon, pike and sea catfish

Olfactory flow in the sea catfish has several elements in common with that of the sturgeon, *Huso dauricus*, and pike, *Esox lucius* (Figs. 21 and 24; Garwood et al., 2019, 2020):

1) All three fishes have an incurrent nostril located in a region of relatively high static pressure (Fig. 24, pink regions), where flow will be forced into the nasal chamber.

2) All three fishes have a nasal feature that impedes external flow (Fig. 24, white asterisk), deflecting it into the nasal chamber (sturgeon: lateral wall of the incurrent nostril; pike: nasal bridge; sea catfish: incurrent nasal flap).

3) All three fishes have an excurrent nostril approximately normal to external flow (Fig. 24, arrow 3). Consequently, in all three fishes the water in the excurrent nostril experiences a static pressure equal or close to the ambient static pressure of the external flow.

4) The pike and the sea catfish have a nasal feature that accelerates flow over the excurrent nostril (Fig. 24, black asterisk), increasing the tractive viscous forces there and thereby augmenting excurrent olfactory flow (pike: dorsal edge of the nasal bridge; sea catfish: excurrent nasal flap). Although the sturgeon *Huso dauricus* lacks this type of feature, at least one other species of sturgeon - *Acipenser schrenckii* - does have it. In *A. schrenckii*, the feature is an excurrent nasal flap (Fig. 15A-C of Garwood et al., 2019).

5) In all three fishes, flow is dispersed over the olfactory sensory surface by a jet impingement-like mechanism (Fig. 24, arrows 5). Specifically, dispersal occurs when incurrent flow decelerates on encountering an internal nasal surface (sturgeon: central support, Fig. 25, CS; pike: nasal chamber floor; sea catfish: anterior olfactory rosette).

6) Vortices may aid dispersal of flow in all three fishes (Fig. 24, arrow 6 and undulating red line, inset): within an olfactory sensory channel (sturgeon, Fig. 25, Vo; sea catfish, Fig. 19) or over the nasal chamber floor (pike, Fig. 17 of Garwood et al., 2020). The vortices may allow fluid to be resampled by the olfactory sensory surface (Garwood et al., 2020).

7) In the sturgeon and the sea catfish, olfactory resampling may also occur when flow passes from one sensory channel to another (Fig. 24, arrow 7, inset). Such inter-channel resampling occurs only rarely in the sturgeon and involves just two sensory channels (Fig. 25, channels 17 and 18). Inter-channel resampling in the sea catfish is, on the other hand, frequent, especially at lower Reynolds numbers (Table 2), and involves up to four channels (e.g. sensory channels 2, 11, 12 and 14 in Fig. 18F).

4.8. Percentage dynamic pressure of free-stream flow harnessed by the nasal regions of the sturgeon, pike and sea catfish

The percentage of the dynamic pressure of the free-stream flow harnessed by the nasal regions of the sturgeon, pike and sea catfish is greatest in the nasal region of the sea catfish (Table 3). We attribute the better performance of the sea catfish's nasal region to:

1) The location of its incurrent nostril on the blunt anterior face of the head (resulting in either the incurrent or the excurrent nasal flap being the stagnation point in the CFD simulations; Fig. A.18, Appendix A.4). The incurrent nostrils of the pike and sturgeon, on the other hand, are located further back on the head (Garwood et al., 2019, 2020).

2) The more elaborate nasal flaps of the sea catfish.

But these remarks should be tempered by the fact that the sea catfish CFD simulations involved a higher Reynolds number (700; Table 3).

We note also that, as in the dye visualisation experiments with the sturgeon model, the dye filament in general passed intact into the incurrent nostril of the plastic sea catfish models (Video clips 1-4), reflecting the significant pressure difference across the incurrent and excurrent nostrils.

4.9. Resampling in the pinnate olfactory rosettes of other fishes

A pinnate olfactory rosette is a common nasal structure in fishes (Burne, 1909). Fishes that have pinnate olfactory rosettes include the European eel, *Anguilla anguilla* (Fig. 21; Aguillidae; Nelson, 2006, p. 116; Teichmann, 1959). Water circulation in the olfactory

sensory channels of the European eel is likely to be achieved by the co-ordinated beating of non-sensory cilia (Teichmann, 1959; Cox, 2013). Teichmann (1959) showed that resampling can occur in the European eel's olfactory rosette. Specifically, through careful experiments, he showed that excurrent flow from one sensory channel could be drawn into the next sensory channel (i.e. the one immediately posterior to the first). As in the sea catfish, such resampling should increase the chances of capturing odorant molecules, and therefore improve the European eel's olfactory sensitivity. Indeed, Teichmann (1959), using a behavioural assay, found that European eels (*TL* 10 – 15 cm) had thresholds to several chemicals of 10^{-15} to 10^{-18} M (on the order of 10^{3} to 10^{6} molecules ml^{-1} of water), suggesting excellent olfactory sensitivity.

Given the evidence of olfactory resampling in two fishes from two different teleostean orders (Fig. 21; sea catfish: Siluriformes; European eel: Anguilliformes; Nelson, 2006, p. 114 and 162, respectively), olfactory resampling may be a common theme in fishes with pinnate olfactory rosettes.

4.10. Limitations

The main limitations of this study were:

1) Most of what we learnt about dispersal of flow amongst the sensory channels, particularly the observation of olfactory resampling, was from the CFD simulations, and was not directly validated by the dye visualisation experiments. This limitation was due to two problems in the dye visualisation experiments. First, although the right nasal region of the plastic version of Model 1 was translucent (Fig. 7A), we were unable to get an unhindered view of the complete olfactory rosette. The excurrent nasal flap was largely responsible for obscuring the view (Video clips 7 – 9). Second, although we tried several experimental arrangements (e.g. different viewing positions), we were unable to get a magnified view of the olfactory rosette.

Dye behaviour in the flume could, however, be replicated by streamlines generated from the CFD simulations (Fig. 13), suggesting indirectly that the CFD evidence for the dispersal of flow amongst the sensory channels was reliable. The agreement between the dye visualisation and CFD results from our other studies of olfactory flow in fishes (Garwood et al., 2019, 2020) supports this claim.

2) For one plastic model (Model 1), the free-stream speed in the dye visualisation experiments (2.1 *TL* s^{-1}) was just above the upper limit (1.9 *TL* s^{-1}) of the swimming speeds observed in the aquarium specimens. The free-stream speed in the dye visualisation experiments was a consequence of making Model 1 as large as possible, so that we could detect any passage of dye through the olfactory sensory channels. It is conceivable that *in vivo* the excurrent nasal flap is depressed at 2.1 *TL* s^{-1}.

3) The cross-section of the plastic models used in the dye visualisation experiments (90 – 91 cm^2; Appendix A.1.5.1*)* was close to the recommended limit (97 cm^2, which is 5 % of the working cross-sectional area of the flume). Based on standard corrections (Barlow et al., 1999, p. 361), the effect on flow in the vicinity of the model from the walls of the flume *should* have been negligible. However, the appearance of a pair of vortices immediately anterior to Model 1 in the dye visualisation experiments (Video clips 15 and 16), but not in the CFD simulations at the same free-stream speed, suggests that the plastic version of Model 1 was too close to the acceptable limit. Consequently, the vortices immediately anterior to Model 1 in the dye visualisation experiments were probably artifacts caused by the proximity of the flume's walls to the model.

Limitations 2) and 3) were mitigated by the CFD simulations. Further limitations are described in Appendix A.2.

5. Conclusions

We conclude that, for the sea catfish:

1) Flow through the nasal chamber can be induced by an external flow.

2) Flow through the nasal chamber is regulated by the position of the excurrent nasal flap, which in turn is controlled by the sea catfish's movements. This regulatory mechanism is distinct from those in other fishes.

3) Flow through the sensory channels of the pinnate olfactory rosette can also be induced by an external flow.

4) Olfactory sampling is thorough, with flow passing through up to four consecutive sensory channels via multiple pathways. Both the medial recess and the peripheral channel may act cooperatively with an anterior sensory channel to effect resampling. At higher Reynolds numbers, sampling may be enhanced by vortices in the medial sensory channels.

5) The mechanisms for driving and dispersing olfactory flow in the sea catfish are common to two other piscine orders (Fig. 21; sturgeons: Acipenseriformes; pikes: Esociformes; Nelson, 2006, p. 92 and p. 204, respectively).

The knowledge from conclusions 3) and 4) may be used to devise a rigid, ultrasensitive microfluidic chemical sensor (Settles, 2005).

Acknowledgements

We thank: Laser Lines/Ogle Models and Prototypes for 3D printing; the staff of Cabela's, Louisiana, particularly Ralph (Wood) Oglesby, for facilitating the *in vivo* observations of *Ariopsis felis*; Kashvi Cox, Matt Cross, Fiona Dickinson, Paul Frith, Richard Hoy, George Oates, Steve Roser, Ian Trussler, and Simon Wharf for technical assistance; Ismet Gursul and Richie Gill for allowing use of, respectively, the flume and ScanIP software in the Department of Mechanical Engineering at Bath; Kevin Webb and Nic Delves-Broughton for photography; John Caprio, Harriet Haysom, and Brian Zimmerman for helpful discussions; and Xavier Mear for German to English translation.

Funding statement

This work was supported by the University of Bath. The Engineering and Physical Sciences Research Council, UK, funded the Henry Moseley X-ray Imaging Facility through the Royce Institute for Advanced Materials (grants EP/F007906/1, EP/F001452/1, EP/I02249X, EP/M010619/1, EP/F028431/1, EP/M022498/1 and EP/R00661X/1). The funding sources were not involved in the conduct of the research, or the preparation of the article.

888 **References**

889 Abel, R.L., Maclaine, J.S., Cotton, R., Xuan, V.B., Nickels, T.B., Clark, T.H., Wang, Z.,
890 Cox, J.P.L., 2010. Functional morphology of the nasal region of a hammerhead shark. Comp.
891 Biochem. Physiol. A 155, 464-475.
892 Abernathy, F.H., 1972. Fundamentals of boundary layers. In: National Committee for Fluid
893 Mechanics Films. Illustrated Experiments in Fluid Mechanics. MIT Press, London, pp. 75-81.
894 Agbesi, M.P.K., Naylor, S., Perkins, E., Borsuk, H.S., Sykes, D., Maclaine, J.S., Wang, Z.,
895 Cox, J.P.L., 2016a. Complex flow in the nasal region of guitarfishes. Comp. Biochem.
896 Physiol. A 193, 52-63.
897 Agbesi, M.P.K., Borsuk, H.S., Hunt, J.N., Maclaine, J.S., Abel, R.L., Sykes, D., Ramsey
898 A.T., Wang, Z., Cox, J.P.L., 2016b. Motion-driven flow in an unusual piscine nasal region.
899 Zoology 119, 500-510.
900 Ayachit, U., 2016. The ParaView Guide. Kitware Inc.
901 Barlow, J.B., Rae, W.H., Pope, A., 1999. Low-Speed Wind Tunnel Testing. 3rd ed. John
902 Wiley & Sons, New York.
903 Barnard, R.H., Philpott, D.R., 2004. Aircraft Flight. 3rd ed. Pearson Education, Harlow.
904 Barnard, R.H., 2009. Road Vehicle Aerodynamic Design. 3rd ed. MechAero Publishing, St
905 Albans.
906 Burne, R.H., 1909. The anatomy of the olfactory organ of teleostean fishes. Proc. Zool. Soc.
907 Lond. 2, 610-663.
908 Caprio, J., 1980. Similarity of olfactory receptor responses (EOG) of freshwater and marine
909 catfish to amino acids. Can. J. Zool. 58, 1778-1784.
910 Cox, J.P.L., 2008. Hydrodynamic aspects of fish olfaction. J. Roy. Soc. Interface 5, 575-593.
911 Cox, J.P.L., 2013. Ciliary function in the olfactory organs of sharks and rays. Fish Fisheries
912 14, 364-390.
913 Cox, J.P.L., Hunt, J.N., Dalby, L.J., Oates, G., Martin, G.S., 2021. STL models of heads and
914 nasal region of *Ariopsis felis*. Mendeley Data, v1. http://dx.doi.org/10.17632/gcsdx4xnsd.1.
915 Douglas, J.F., Gasiorek, J.M., Swaffield, J.A., 1985. Fluid Mechanics. 2nd ed. Pitman,
916 Massachusetts.
917 Døving, K.B., Dubois-Dauphin, M., Holley, A. Jourdan, F., 1977. Functional anatomy of the
918 olfactory organ of fish and the ciliary mechanism of water transport. Acta Zool. 58, 245-255.
919 Garwood, R.J., Behnsen, J., Haysom, H.K., Hunt, J.N., Dalby, L.J., Quilter, S.K., Maclaine,
920 J.S., Cox, J.P.L., 2019. Olfactory flow in the sturgeon is externally driven. Comp. Biochem.
921 Physiol. A 235, 211-225.

Garwood, R.J., Behnsen, J., Ramsey, A.T., Haysom, H.K., Dalby, L.J., Quilter, S.K., Maclaine, J.S., Wang, Z., Cox, J.P.L., 2020. The functional anatomy of the pike, *Esox lucius* (L.). Comp. Biochem. Physiol. A 244, article number 110688.

Goldstein, S., 1965. Modern Developments in Fluid Dynamics. Dover Publications, New York.

Haynes, W.M., Lide, D.R., 2011. CRC Handbook of Chemistry and Physics. 92nd ed. CRC Press, Boca Raton.

Helfman, G.S., Collette, B.B., Facey, D.E., Bowen, B.W., 2009. The Diversity of Fishes. 2nd ed. Wiley-Blackwell, Chichester.

Holmes, W.M., Cotton, R., Xuan, V.B., Rygg, A.D., Craven, B.A., Abel, R.L., Slack, R., Cox, J.P.L., 2011. Three-dimensional structure of the nasal passageway of a hagfish and its implications for olfaction. Anat. Rec. 294, 1045-1056.

Howard, L.E., Holmes, W.M., Ferrando, S., Maclaine, J.S., Kelsh, R.N., Ramsey, A., Abel, R.L., Cox, J.P.L., 2013. Functional nasal morphology of chimaerid fishes. J. Morph. 274, 987-1009.

Kasumyan, A.O., 2003. The lateral line in fish. J. Ichthyol. 43 (Suppl. 2), S175-S213.

Kline, S.J., 1972. Flow visualization. In: National Committee for Fluid Mechanics Films. Illustrated Experiments in Fluid Mechanics. MIT Press, London, pp. 34-38.

Lugt, H.J., 1983. Vortex Flow in Nature and Technology. John Wiley & Sons, New York.

Massey, B.S., 1989. Mechanics of Fluids. 6th ed. Van Nostrand Reinhold, London.

Nelson, J.S., 2006. Fishes of the World. 4th ed. John Wiley & Sons, New Jersey.

Pfeiffer, W., 1968. Das Geruchsorgan der Polypteridae (Pisces, Brachiopterygii) (The olfactory organ of the Polypteridae). Z. Morph. Tiere 63, 75-110. In German, with an English summary.

Ramsey, A., Houston, T.F., Ball, A.D., Goral, T., Barclay, M.V.L., Cox, J.P.L., 2015. Towards an understanding of molecule capture by the antennae of male beetles belonging to the genus *Rhipicera* (Coleoptera, Rhipiceridae). Anat. Rec. 298, 1519-1534.

Reiten, I., Uslu, F.E., Fore, S., Pelgrims, R., Ringers, C., Verdugo, C.D., Hoffman, M., Lal, P., Kawakami, K., Pekkan, K., Yaksi, E., Jurisch-Yaksi, N., 2017. Motile-cilia-mediated flow improves sensitivity and temporal resolution of olfactory computations. Curr. Biol. 27, 166-174.

Rouhi, A.M., 1997. Detecting illegal substances. Chem. Eng. News 75 (39), 24-29.

Settles, G.S., 2005. Sniffers: fluid-dynamic sampling for olfactory trace detection on Nature and homeland security. J. Fluids Eng. 127, 189-218.

Shapiro, A.H., 1961. Shape and Flow. Heinemann, London.

Shapiro, A.H., 1972. Pressure fields and fluid acceleration. In: National Committee for Fluid Mechanics Films, Illustrated Experiments in Fluid Mechanics. MIT Press, London, pp. 39-46.

Teichmann, H., 1959. Über die Leistung des Geruchssinnes beim Aal [*Anguilla anguilla* (L.)] (On the performance of the sense of smell of the eel). Z. vgl. Physiol. 42, 206-254. In German.

Thwaites, B., 1960. Incompressible Aerodynamics. Clarendon Press, Oxford.

Vogel, S., 1978. Organisms that capture currents. Sci. Am. 239 (2), 108-117.

Vogel, S., 1988. How organisms use flow-induced pressures. Am. Sci. 76, 28-34.

Vogel, S., 1994. Life in Moving Fluids. 2nd ed. Princeton University Press, Princeton.

Wang, Z.-J., Jiang, P., Gursul, I., 2007. Effect of thrust-vectoring jets on delta wing aerodynamics. J. Aircraft 44, 1877-1888.

Weller, H.G., Tabor, G., Jasak, H., Fureby, C., 1998. A tensorial approach to computational continuum mechanics using object-oriented techniques. Comput. Phys. 12, 620-631.

Zeiske, E., Caprio, J., Gruber, S.H., 1986. Morphological and electrophysiological studies on the olfactory organ of the lemon shark, *Negaprion brevirostris* (Poey). In: Uyeno, T., Arai, R., Taniuchi, T., Matsuura, K. (Eds.), Indo-Pacific Fish Biology (Proceedings of the Second International Conference on Indo-Pacific Fishes, Tokyo, 29 July–3 August, 1985). Ichthyological Society of Japan, Tokyo, pp. 381–391.

Zeiske, E., Theisen, B., Breucker, H., 1994. The olfactory organ of the hardhead sea catfish, *Arius felis* (L.). Acta Zool. 75, 115-123.

977 **Video**

978 Dye visualisation with the plastic models of the sea catfish. Flow is left to right and the free-
979 stream speed is 5 cm s^{-1}. Unless stated otherwise: the dye is red food dye; pitch, yaw, and roll
980 angles are 0°; the camera positions (Fig. A.7, Appendix A.4) are *a* and X; the camera is
981 mounted on a tripod; and each clip is rotated by 180°.
982
983 **Clip 1** Model 1A. Passage of dye through nasal chamber. Dorsal aspect of head. Tubing for
984 dye release on left. Roll + 90°. Compare with Fig. 13A.
985 **Clip 2** Model 1A. Passage of dye through nasal chamber. Dorsal aspect. Roll + 90°. Compare
986 with Fig. 13B.
987 **Clip 3** Model 2A. Passage of dye through nasal chamber. *Right* lateral aspect. Clip flipped
988 horizontally.
989 **Clip 4** Model 1B. Passage of dye through nasal chamber. *Right* lateral aspect. Vertical line,
990 bottom right of clip: damage to model. Dye: rhodamine 6G. Clip flipped horizontally.
991 Compare with Fig. 13C.
992 **Clip 5** Model 1A. Dye fanning in front of the incurrent nasal flap. Superior view. Yaw + 10°;
993 roll + 45°. Compare with Fig. 13D.
994 **Clip 6** Model 1B. Deflection of dye medially within the nasal chamber. Superior view. Dye:
995 rhodamine 6G. Yaw + 10°; camera positions *b* and Y. Compare with Fig. 13E.
996 **Clip 7** Model 1A. Passage of dye through sensory channels 22 – 26. Superior view. Camera
997 positions *b* and Y. Compare with Fig. 13F.
998 **Clip 8** Model 1A. Passage of dye through sensory channels 8 – 11 and 21 – 26. Superior view.
999 Pitch + 10°; camera positions *b* and X.
1000 **Clip 9** Model 1A. Passage of dye through sensory channels 8 – 11 and 22 – 26. Superior view.
1001 Yaw – 10°; camera positions *b* and Y; camera hand-held.
1002 **Clip 10** Model 2B. Passage of dye through nasal chamber with depressed excurrent nasal flap.
1003 Dorsal aspect. Dye: rhodamine 6G. Roll + 180°; camera positions *c* and X.
1004 **Clip 11** Model 1B. Vortex on dorsal edge of incurrent nasal flap. *Right* lateral aspect. Dye:
1005 rhodamine 6G. Clip flipped horizontally. Compare with Fig. 13G.
1006 **Clip 12** Model 1B. Vortex on external face of lateral excurrent nasal flap. Superior view.
1007 Dye: rhodamine 6G. Yaw + 10°; camera positions *b* and Y. Compare with Fig. 13H.
1008 **Clip 13** Model 2B. Recirculation of dye behind truncated lateral barbel. *Right* lateral aspect.
1009 Dye: rhodamine 6G. Clip flipped horizontally.

Clip 14 Model 2A. Vortex in mouth. *Right* lateral aspect. Clip flipped horizontally.

Clip 15 Model 1A. Vortex anterior to rostrum. *Right* lateral aspect. Clip flipped horizontally.

Clip 16 Model 1B. Vortex anterior to rostrum. Dorsal aspect. Dye: rhodamine 6G. Roll + 90°.

Figures

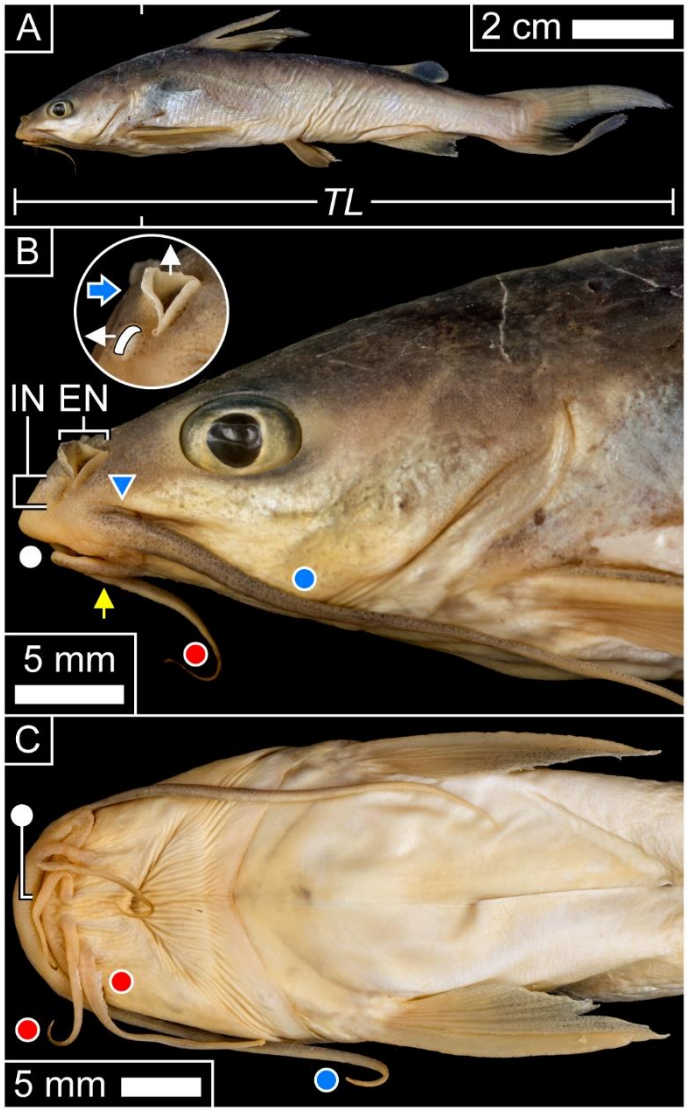

Fig. 1 Preserved specimen of sea catfish (*Ariopsis felis*, BMNH 1983.7.6.12) used to generate models for dye visualisation and computational fluid dynamics. (A) Complete specimen. White marks: posterior extent of X-ray scan. (B) Lateral aspect of head. Yellow arrow: location of TIFF image shown in Fig. 3A. Blue arrowhead: base of lateral barbel. Inset: lateral aspect of *right* nasal region. Horizontal and vertical white arrows: orientation of incurrent nostril (filled white region) and excurrent nostril, respectively, to oncoming flow (blue arrow). (C) Ventral aspect of head. White, blue and red disks: mouth, lateral and ventral barbels, respectively. EN: Excurrent nostril; IN: incurrent nostril; *TL*: total length.

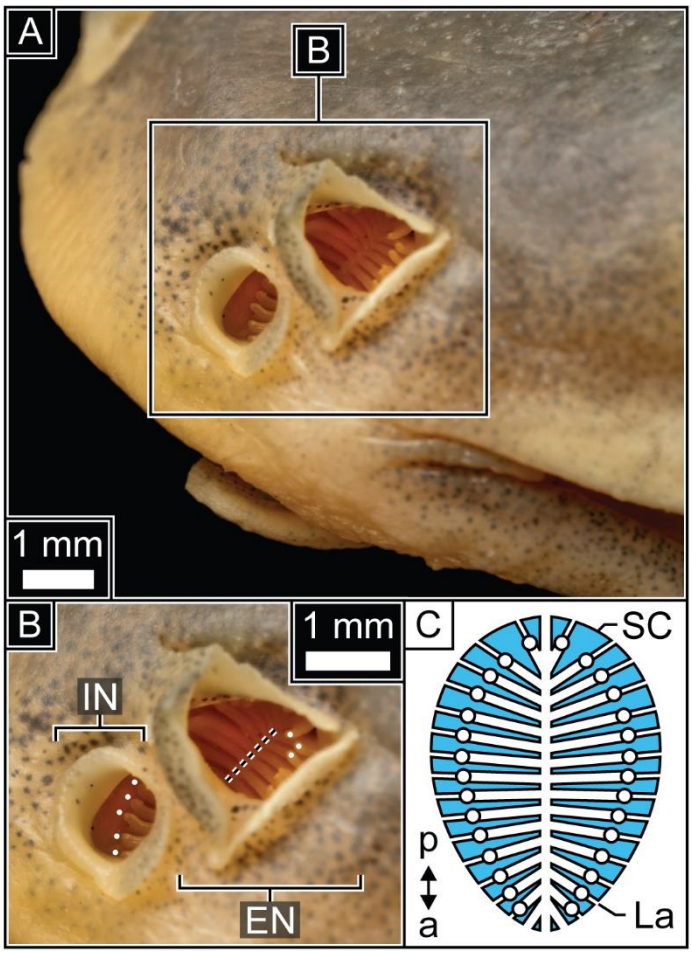

Fig. 2 Partial views of the olfactory rosette of sea catfish (*Ariopsis felis*, BMNH 1983.7.6.12) used to generate models for dye visualisation and computational fluid dynamics. (A) Superior view of left nasal region. (B) Magnified view of left nasal region. Olfactory rosette visible through the incurrent and excurrent nostrils. Dashed line: raphe. (C) Schematic of olfactory rosette. White disks in (B) and (C): tips of olfactory lamellae. a: Anterior; EN: excurrent nostril; IN: incurrent nostril; La: olfactory lamella; p: posterior; SC: sensory channel (blue region).

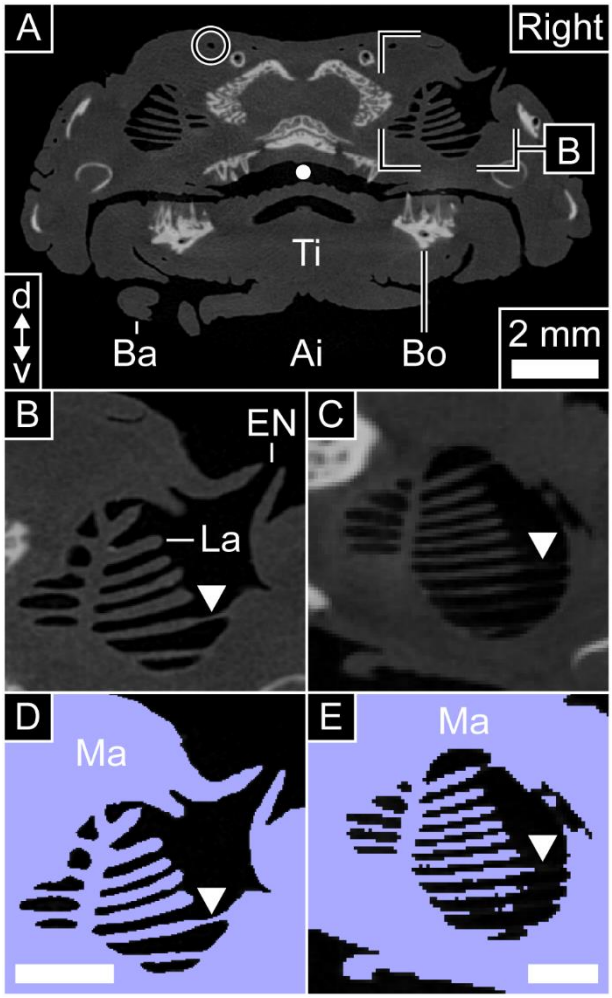

Fig. 3 Image processing of micro-CT scans of two sea catfishes (*Ariopsis felis*). (A) Transverse cross-section through head of specimen BMNH 1983.7.6.12. For location of cross-section, see Fig. 1B, yellow arrow. White disk: oral cavity. Circle: lateral line canal. (B) Transverse cross-section through right olfactory rosette of specimen BMNH 1983.7.6.12. (C) Transverse cross-section through *left* olfactory rosette of specimen BMNH 1948.8.6.196. (D) Same image as (B), with mask superimposed. (E) Same region of interest as (C), with mask superimposed on image. The pixel spacing in (E) is twice that in (C) (Appendix A.1.2.2). Scale bars in (D) and (E): 1 mm. Scale bars in (D) and (E) also apply to (B) and (C), respectively. Arrowhead: lamellar attachment to the wall of the nasal chamber. Ai: Air; Ba: barbel; Bo: bone; d: dorsal; EN: excurrent nostril; La: olfactory lamella; Ma: mask; Ti: tissue; v: ventral.

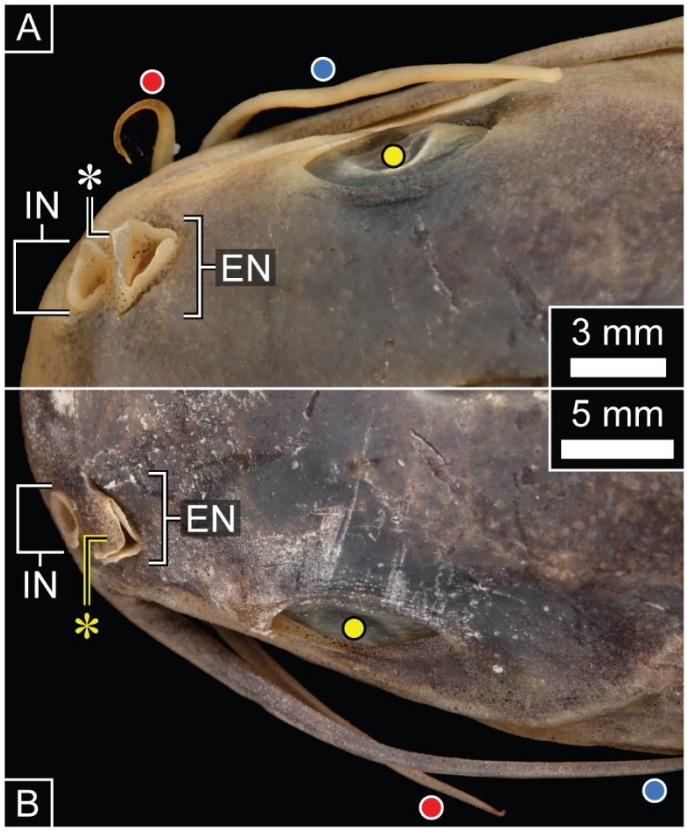

Fig. 4 Dorsal aspects of heads of two preserved sea catfishes (*Ariopsis felis*). (A) Specimen BMNH 1983.7.6.12. Right dorsal aspect. White asterisk: elevated nasal flap. (B) Specimen BMNH 1948.8.6.196. Left dorsal aspect. Yellow asterisk: depressed nasal flap. Yellow, blue and red disks: eye, lateral and ventral barbels, respectively. EN: Excurrent nostril; IN: incurrent nostril.

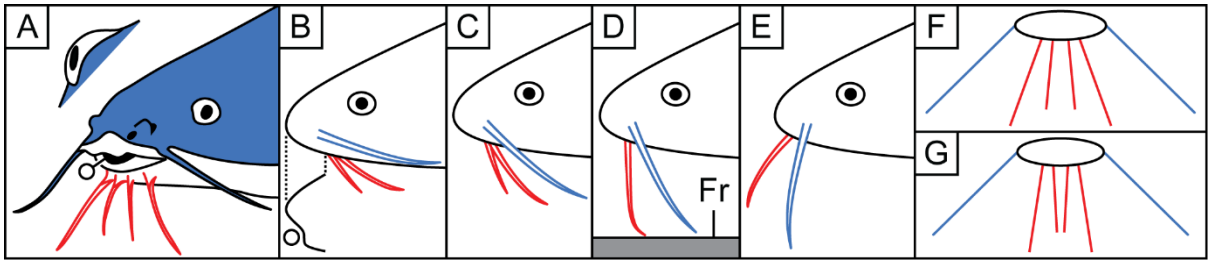

Fig. 5 Attitudes of barbels and mouth when a sea catfish swims forwards. Schematics based on video footage of aquarium specimens of *Ariopsis felis*. (A) – (C): Mid-water; (D) – (G): close to floor (Fr). (A) Anterolateral aspect. Inset: anterior aspect of right eye of a resting specimen. (B) – (E): Lateral aspects. Inferior outline in (B): attitude of mouth (white disk). (F) and (G): Anterior aspects. Ellipse: idealised head. Barbels coloured blue (lateral) and red (ventral). Larger pair of ventral barbels eclipse smaller pair of ventral barbels in (D) and (E).

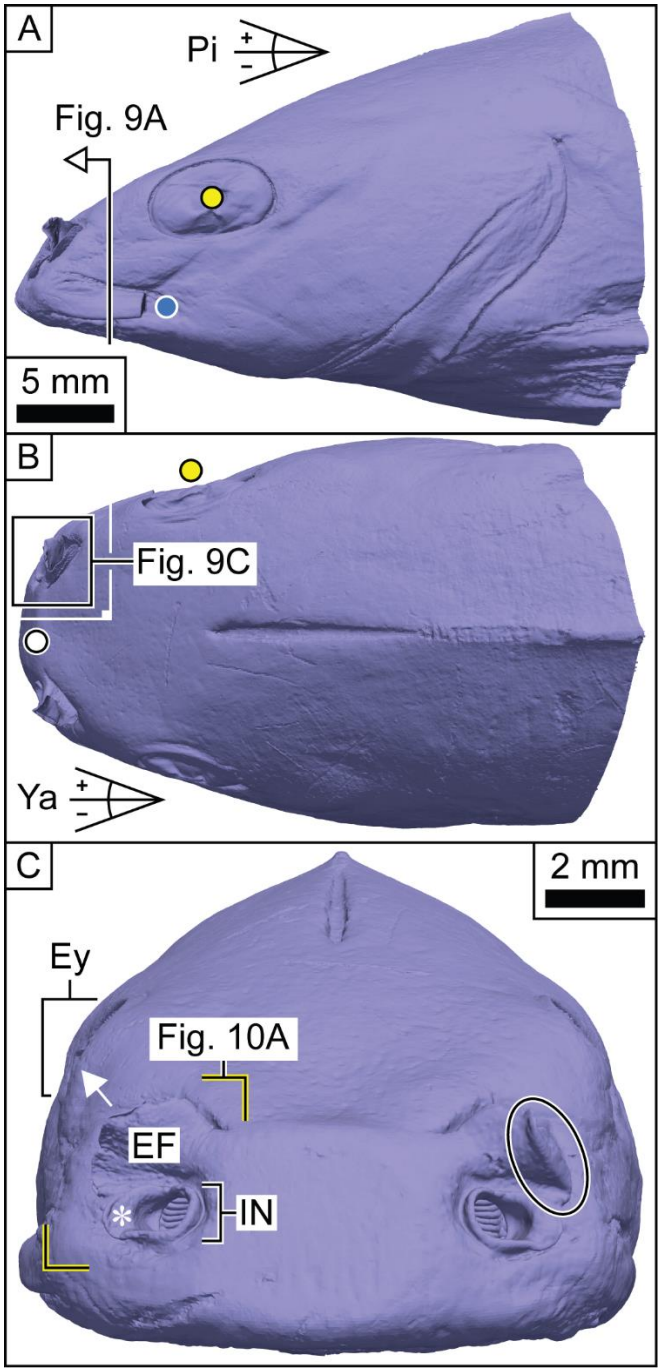

Fig. 6 Surface model of head of sea catfish. Model derived from specimen BMNH 1983.7.6.12. (A) *Right* lateral aspect. Scale bar applies also to (B). (B) Dorsal aspect. Translucent region of plastic model lies within two white lines marked by right angle. (C) Anterior aspect. Asterisk: incurrent nasal flap. White arrow: dorsolateral orientation of excurrent nostril. Ellipse: bent back left excurrent nasal flap. Locations of Figs. 9A, 9C and 10A indicated in panels (A), (B) and (C), respectively. Yellow, white and blue disks: eye, rostrum and lateral barbel, respectively. EF: Excurrent nasal flap; Ey: eye; IN: incurrent nostril; Pi: pitch; Ya: yaw.

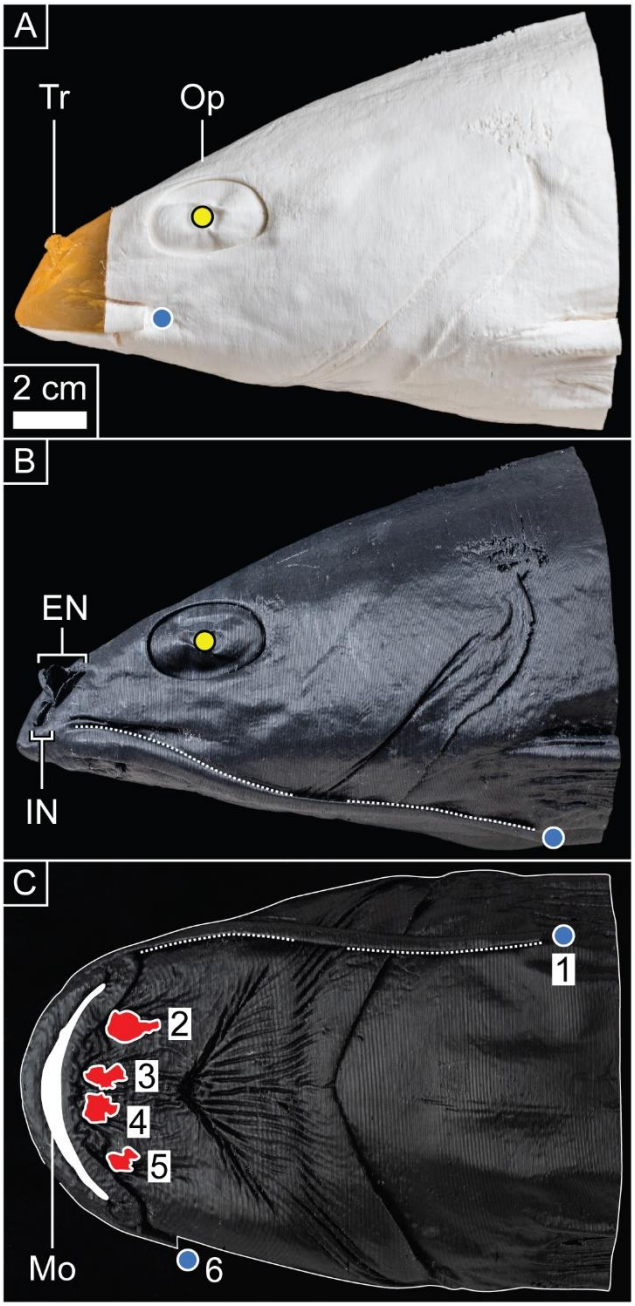

Fig. 7 Plastic models of head of sea catfish. Models derived from specimen BMNH 1983.7.6.12. (A) *Right* lateral aspect of Model 1A. The translucent nasal region has been stained yellow by the food dye used in dye visualisation experiments. Scale bar applies to all panels. (B) and (C): Lateral and ventral aspects, respectively, of Model 1B. White dashed line: edge of left lateral barbel, where it contacts the head. Red regions in (C): truncated ventral barbels. Barbels numbered in (C). Filled white region in (C): mouth. Yellow and blue disks: eye and lateral barbels, respectively. EN: Excurrent nostril; IN: incurrent nostril; Mo: mouth; Op: opaque part; Tr: translucent part.

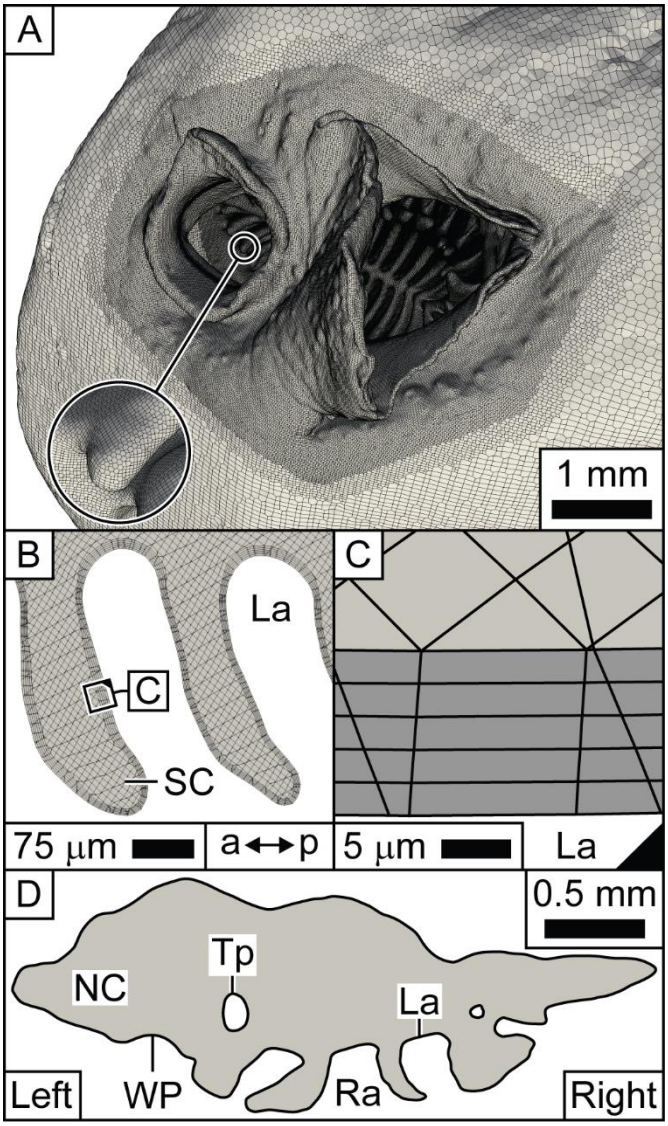

Fig. 8 CFD mesh of head of sea catfish. Mesh derived from specimen BMNH 1983.7.6.12. (A) Refinement of mesh on model surface. Nasal region (superior view). Large circle: magnification of region in small circle. Labels deliberately omitted to allow reader to see mesh. (B) Slice through mesh. Olfactory rosette. For location of slice, see Fig. A.15A, Appendix A.4. (C) Enlargement of box in (B) (rotated – see triangular marker), showing the five layers of refined cells (shaded) immediately adjacent to olfactory lamellar surface. (D) Schematic of slice used to calculate Reynolds numbers of flow through nasal chamber (Appendix A.1.6). For location of slice, see Fig. A.15B, Appendix A.4. a: Anterior; La: olfactory lamella; NC: nasal chamber; p: posterior; Ra: raphe; SC: sensory channel 28; Tp: olfactory lamellar tip; WP: wetted perimeter.

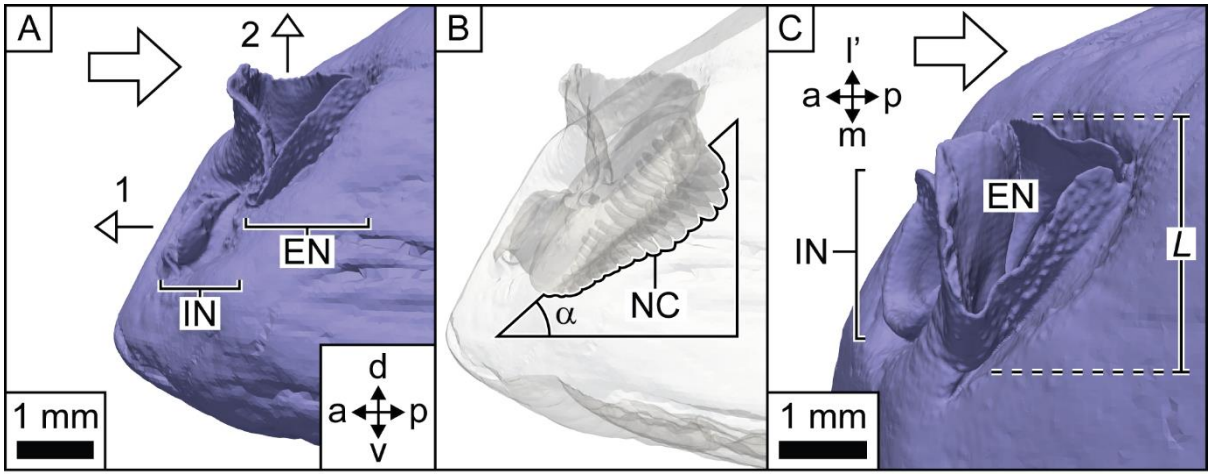

Fig. 9 Surface model of *right* nasal region of sea catfish. Model derived from specimen BMNH 1983.7.6.12. (A) Lateral aspect (Fig. 6A, arrow). Arrows 1 and 2: orientation of incurrent and excurrent nostrils, respectively, to oncoming flow. (B) Translucent lateral aspect (20 % opacity). α: angle at which floor of nasal chamber inclined to body axis. (C) Dorsal aspect (box, Fig. 6B). Large arrow: direction of free-stream flow. a: Anterior; d: dorsal; EN: excurrent nostril; IN: incurrent nostril; l': lateral; *L*: characteristic dimension of nasal region; m: medial; NC: floor of nasal chamber; p: posterior; v: ventral.

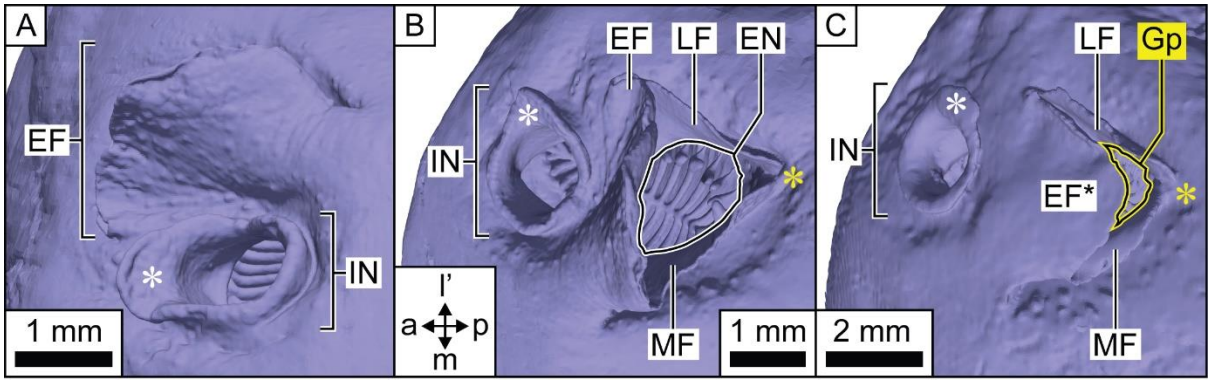

Fig. 10 Nasal flaps of sea catfish surface models. (A) and (B): Anterior aspect and superior view, respectively, of surface model derived from specimen BMNH 1983.7.6.12 (for location of panel A, see Fig. 6C, yellow brackets). Nasal flap elevated. (C) Superior aspect of surface model derived from specimen BMNH 1948.8.6.196. Nasal flap depressed. *Left* nasal region. Anatomical compass in (B) applies also to (C). White asterisk: incurrent nasal flap. Yellow asterisk: split between lateral and medial excurrent nasal flaps. a: Anterior; EF and EF*: elevated and depressed excurrent nasal flaps, respectively; EN: excurrent nostril; Gp: gap; IN: incurrent nostril; l': lateral; LF: lateral excurrent nasal flap; m: medial; MF: medial excurrent nasal flap; p: posterior.

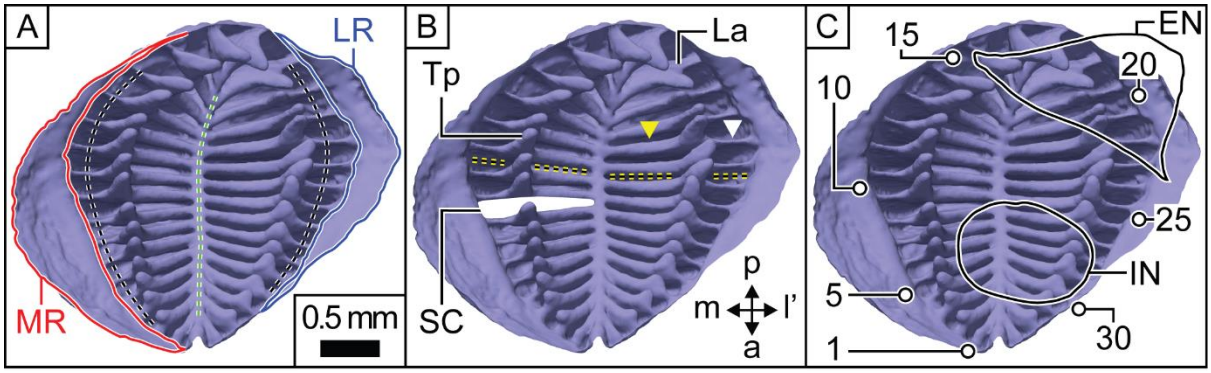

Fig. 11 Olfactory rosette of sea catfish surface model. Anterior aspect of right olfactory rosette. Surface model derived from specimen BMNH 1983.7.6.12. (A) Medial recess (MR, red outline), lateral recess (LR, blue outline), peripheral channel (black dashed line), and raphe (green dashed line). (B) Sensory channel (SC, white region), olfactory lamella (La) and olfactory lamellar tip (Tp). Yellow dashed line: location of transverse section shown in Fig. 12. Yellow and white arrowheads: proximal and distal dorsal edges of olfactory lamella, respectively. (C) Sensory channel numbering, and positions of incurrent nostril (IN) and excurrent nostril (EN) with respect to olfactory rosette. a: Anterior; l': lateral; m: medial; p: posterior.

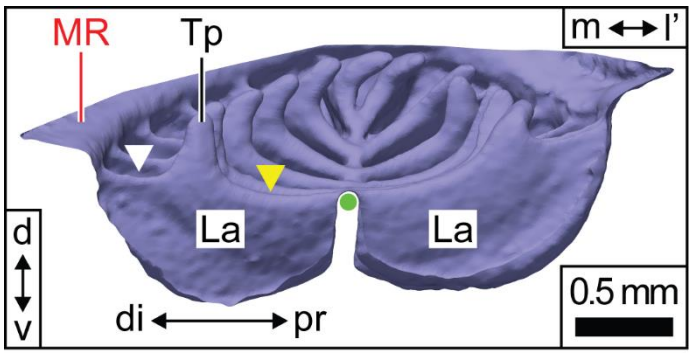

Fig. 12 Transverse section through right olfactory rosette of sea catfish surface model. Surface model derived from specimen BMNH 1983.7.6.12. For location of section, see Fig. 11. Yellow and white arrowheads: proximal and distal dorsal edges of olfactory lamella, respectively. Green disk: raphe. d: Dorsal; di: distal; l': lateral; La: olfactory lamella; m: medial; MR: medial recess; pr: proximal; Tp: olfactory lamellar tip; v: ventral.

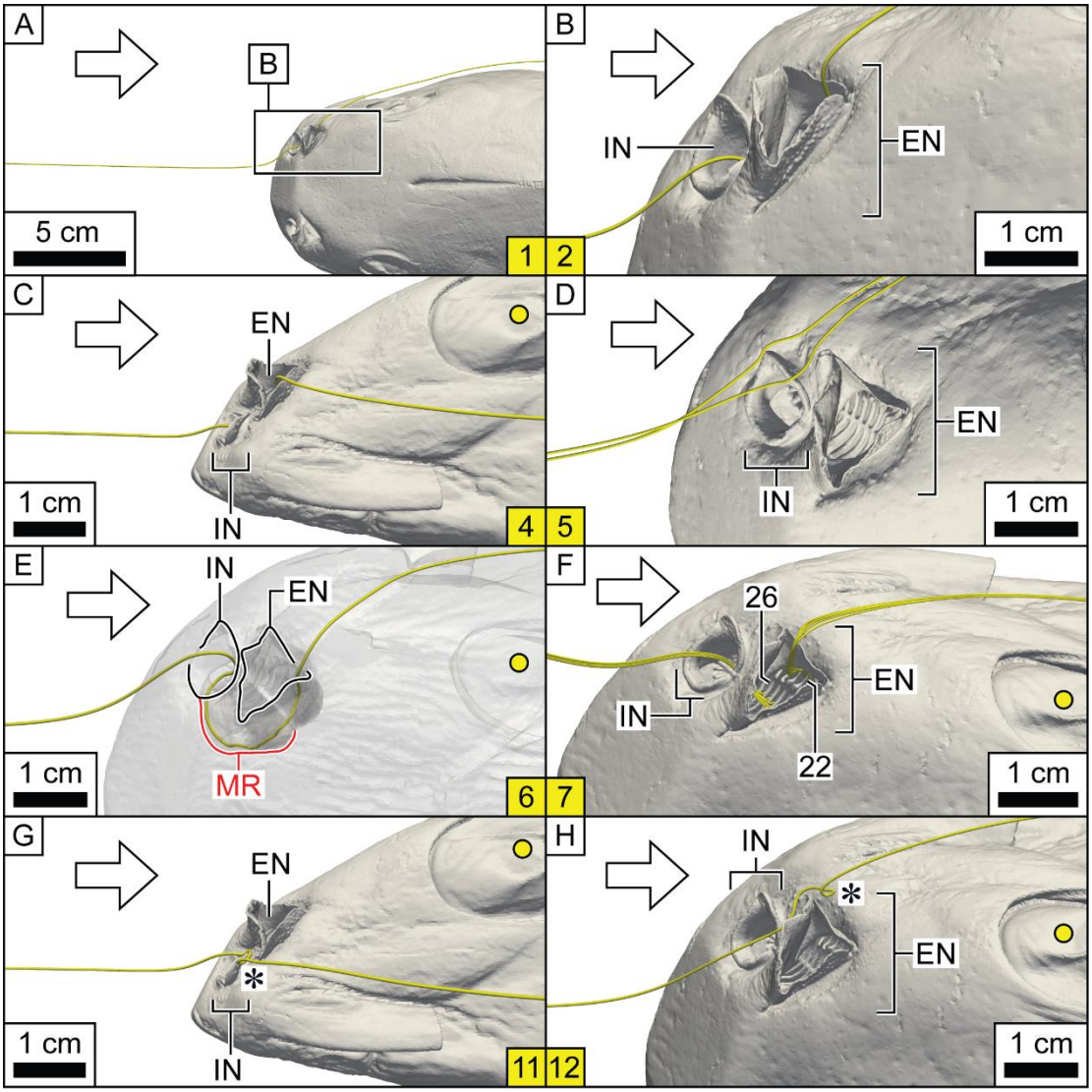

Fig. 13 Correspondence of CFD-generated streamlines to dye behaviour in the plastic model (Model 1A) of the sea catfish. Model 1A is represented by the surface model. Reynolds numbers: 600 – 800. For pitch and yaw angles, see individual legends for video clips (Supplementary data). Streamline(s) (yellow tubes) correspond to dye behaviour in: (A) Video clip 1; (B) Video clip 2; (C) Video clip 4; (D) Video clip 5; (E) Video clip 6; (F) Video clip 7; (G) Video clip 11; and (H) Video clip 12 (video clip identified by number in yellow box in each panel). (A) and (B): Dorsal aspect of model. (C) and (G): *Right* lateral aspect of model. (D) – (F) and (H): Superior views of model. Model in (E) at 20% opacity, to show passage of streamline through medial recess. Two sensory channels are numbered in (F). Scale bars refer to the size of the *plastic* model. Arrow: direction of free-stream flow. Asterisk: vortex. Yellow disk: eye. EN: Excurrent nostril; IN: incurrent nostril; MR: medial recess.

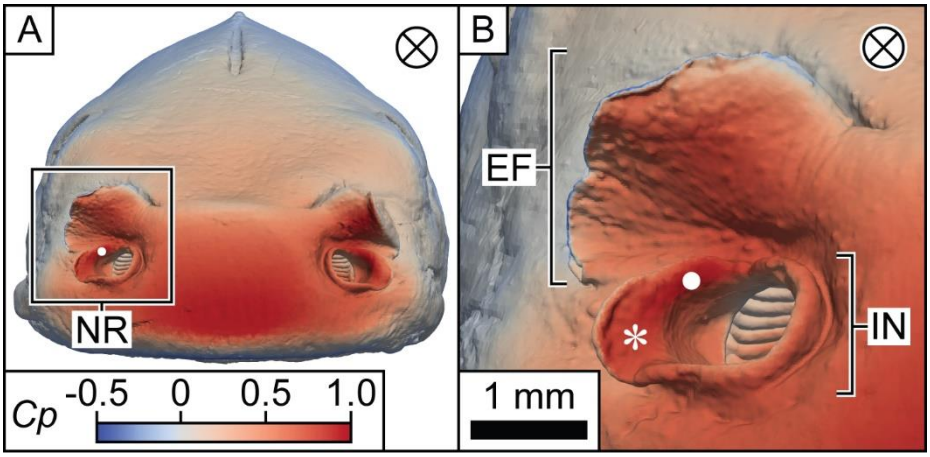

Fig. 14 Static pressure on the surface of sea catfish CFD model. Reynolds number: 300. Yaw: 0°. Surface coloured according to pressure coefficient (*Cp*, panel A). (A) Anterior aspect of head. For scale, see Fig. 6C. (B) Anterior aspect of nasal region (highlighted in panel A). Cross: direction of free-stream flow (into page). Asterisk: incurrent nasal flap. White disk: stagnation point. EF: Excurrent nasal flap; IN: incurrent nostril; NR: nasal region.

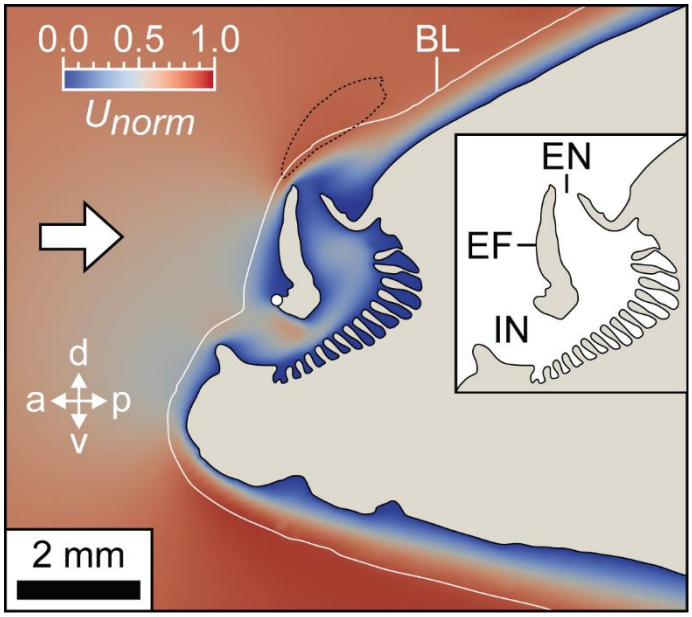

Fig. 15 Sagittal slice through CFD mesh of right nasal region of sea catfish. For location of slice, see Fig. A.15A, Appendix A.4. Reynolds number: 300. Yaw: 0°. Inset: key parts of nasal region. Flow speed (U_{norm}) normalised to the maximum speed in slice (which lies outside of the image shown). The region within the dashed line encompasses (in the dorsal nasal region) speeds > 0.8 on the normalised scale. Arrow: direction of free-stream flow. White line: outer limit of boundary layer (defined by a vorticity of 50 s^{-1}). White disk: maximum *Cp* in slice. a: Anterior; BL: boundary layer; d: dorsal; EF: excurrent nasal flap; EN: excurrent nostril; IN: incurrent nostril; p: posterior; v: ventral.

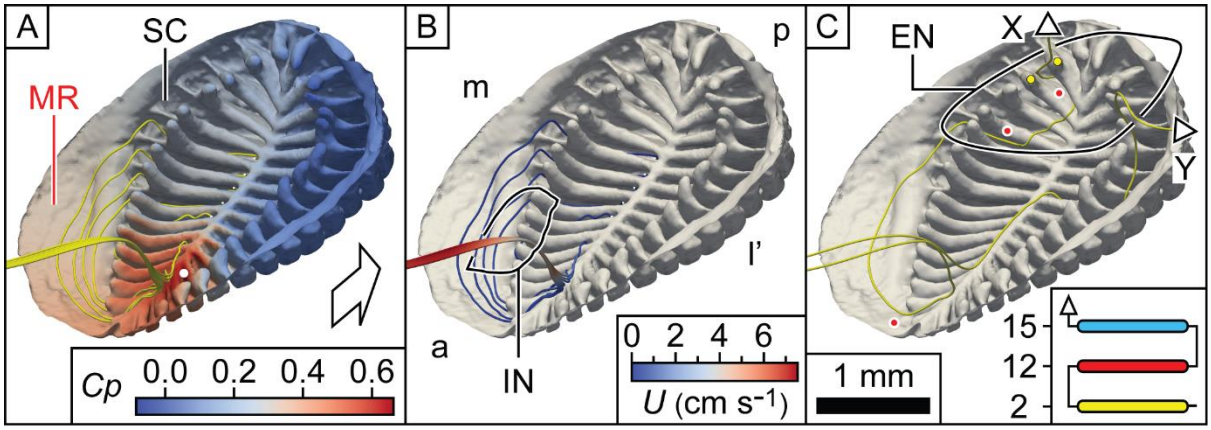

Fig. 16 Impaction of flow on floor of right nasal chamber of sea catfish CFD model. Reynolds number: 300. Yaw: 0°. (A) Static pressure on nasal chamber floor. Streamlines: yellow tubes. Each small white disk marks a streamline emerging from a sensory channel. Surface coloured according to pressure coefficient (*Cp*). Large white disk: point of maximum *Cp* on nasal chamber floor. Arrow: direction of free-stream flow. (B) Flow decelerating as it approaches nasal chamber floor. Streamlines coloured according to speed (*U*). (C) Pathways through sensory channels taken by two streamlines (X and Y). Red disks: sensory channels through which Streamline X passes. Yellow disks: lamellar protrusions. Inset: schematic of the pathway through the sensory channels (numbered rounded rectangles) taken by Streamline X. Sensory channels coloured according to whether streamline (small arrow) has passed previously through zero (yellow), one (red), or two (blue) sensory channel(s). a: Anterior; EN and IN: positions of excurrent and incurrent nostrils, respectively; l': lateral; m: medial; MR: medial recess; p: posterior; SC: sensory channel.

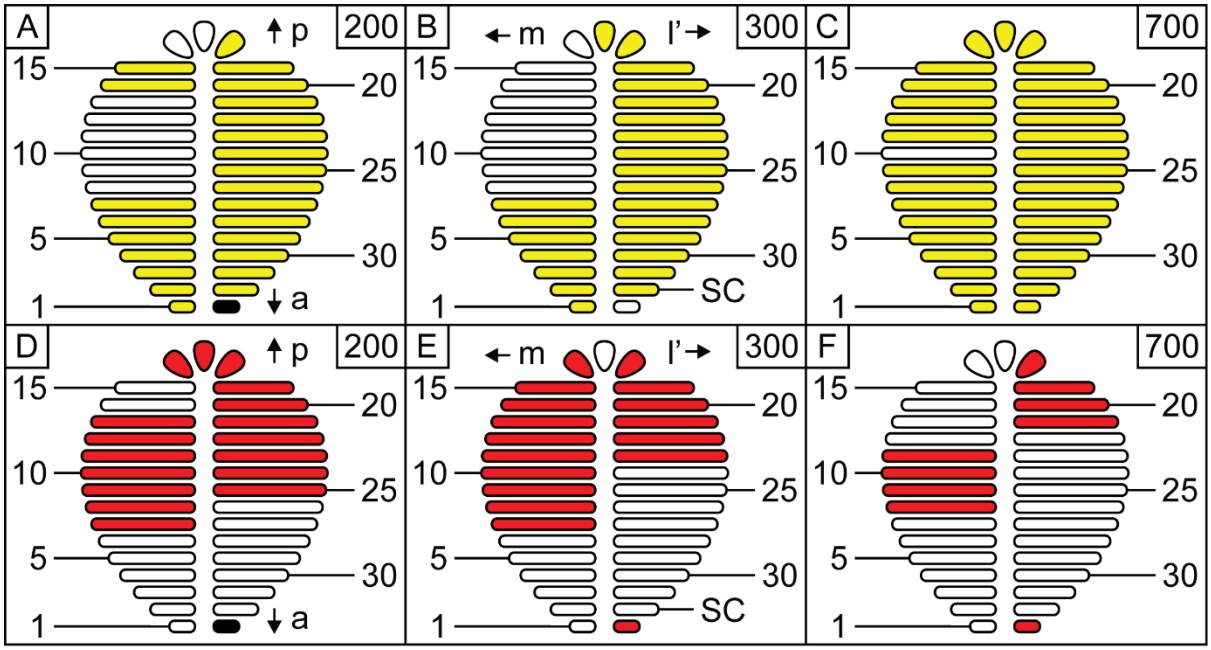

Fig. 17 Schematic showing sensory channels which CFD streamlines enter either directly (A – C) or indirectly (D – F). Right olfactory rosette of sea catfish CFD model. Reynolds number in top right box. Yaw: 0°. Sensory channels (rounded rectangles) coloured according to whether streamlines enter them directly (yellow) or indirectly (red). Streamlines in sensory channel 33 at a Reynolds number of 200 (panels A and D, black rounded rectangles) were broken (Appendix A.2). Consequently, it was not possible to tell whether these streamlines entered this channel directly or indirectly. a: Anterior; l': lateral; m: medial; p: posterior; SC: sensory channel.

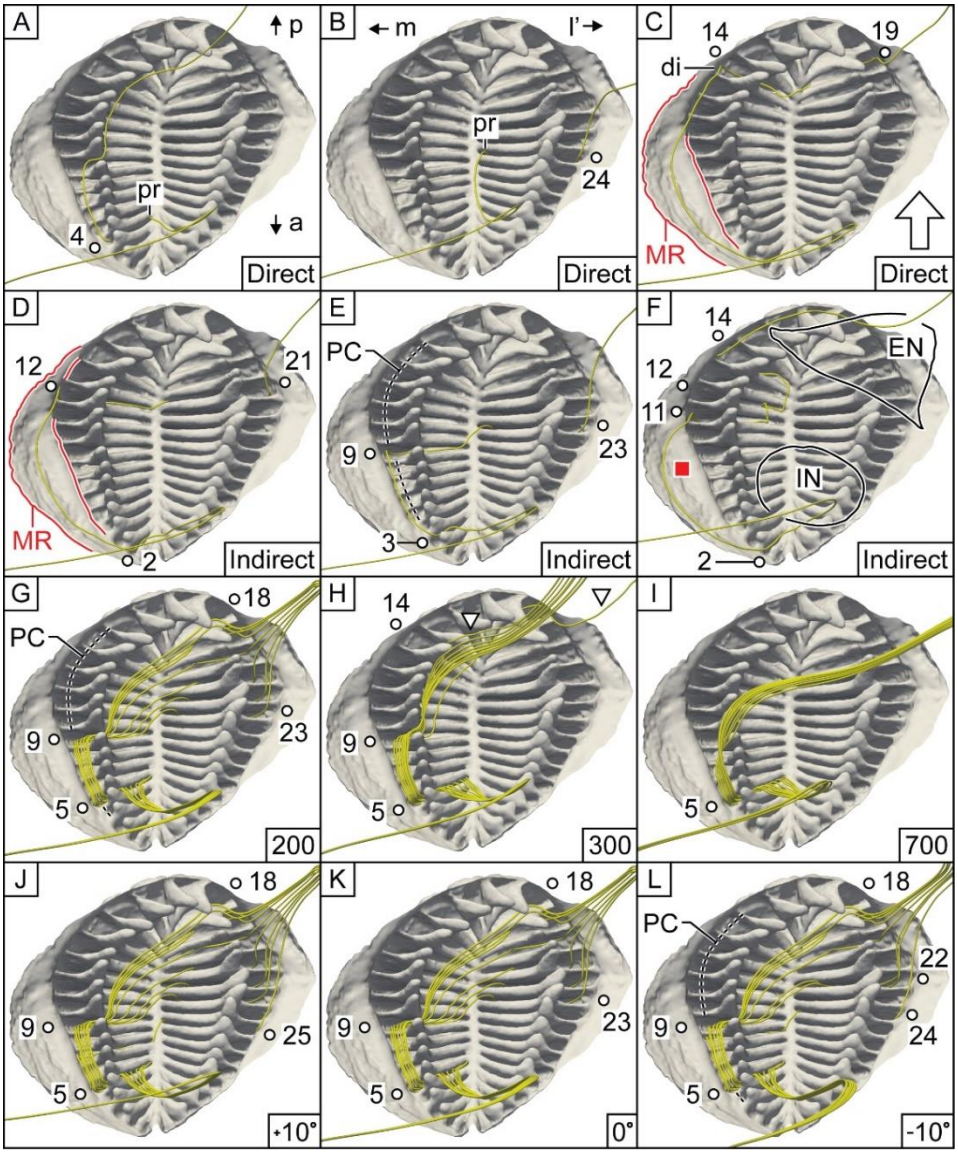

Fig. 18 Olfactory flow in right olfactory rosette of sea catfish CFD model. Streamlines: yellow tubes. Key sensory channels numbered. (A) – (C): Direct entry into a sensory channel. Reynolds numbers: 300 (A and B) and 200 (C). Yaw: 0°. (D) – (F): Indirect entry into a sensory channel. Reynolds numbers: 200 (D and E) and 700 (F). Yaw: 0° (D and E) and + 10° (F). (G) – (I): Reduced inter-channel olfactory resampling with increasing speed. Reynolds number in bottom right box. Yaw: 0°. (J) – (L): Effect of yaw on olfactory flow. Yaw angle in bottom right box. Reynolds number: 200. Arrow: direction of free-stream flow. Red square in (F): medial recess. Arrowheads in (H): streamlines that pass through three sensory channels. For scale, see Fig. 19B. a: Anterior; di: distal; EN and IN: positions of excurrent and incurrent nostrils, respectively; l': lateral; m: medial; MR: medial recess; p: posterior; PC: peripheral channel; pr: proximal.

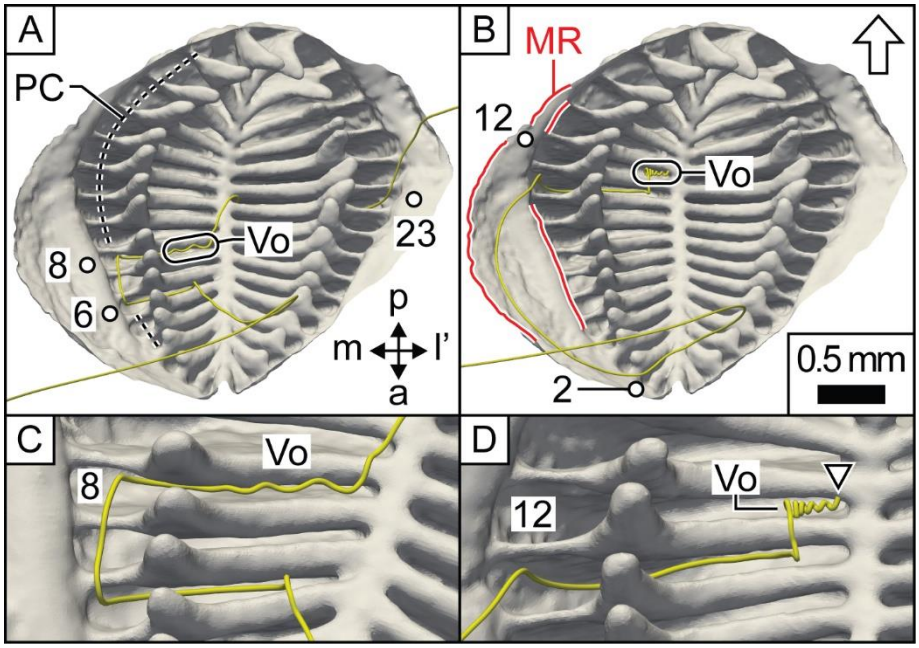

Fig. 19 Olfactory flow in right olfactory rosette of sea catfish CFD model. Vortices in sensory channels. Streamlines: yellow tubes. Key sensory channels numbered. (A) Vortex in sensory channel 8. Reynolds number: 300. Yaw: 0°. (B) Vortex in sensory channel 12. Reynolds number: 700. Yaw: + 10°. Arrow: direction of free-stream flow. (C) and (D): superior views of vortices in (A) and (B), respectively. Arrowhead: broken streamline (Appendix A.2). a: Anterior; d: dorsal; l': lateral; m: medial; MR: medial recess; p: posterior; PC: peripheral channel; Vo: vortex.

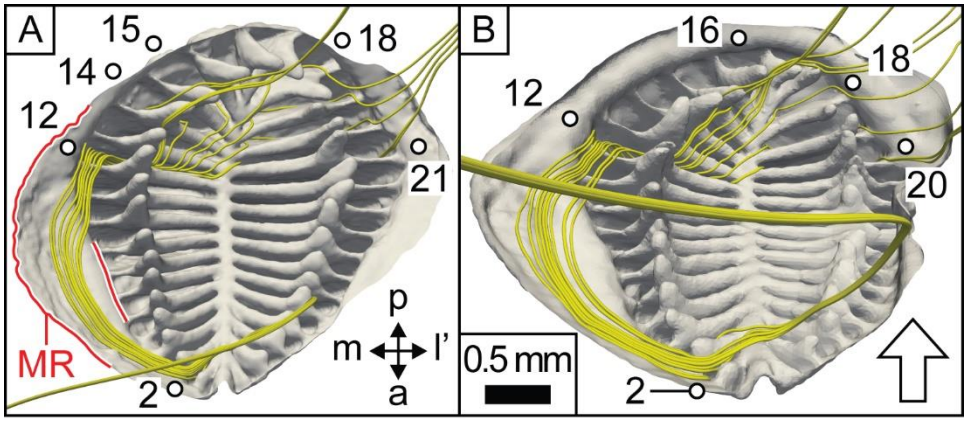

Fig. 20 Olfactory flow in sea catfish CFD model. Streamlines (yellow tubes) in (A) right and (B) left olfactory rosettes. Reynolds number: 300. Yaw: 0°. In general, sensory channels through which streamlines pass are numbered. Scale bar applies to both panels. Arrow: direction of free-stream flow. a: Anterior; l': lateral; m: medial; MR: medial recess; p: posterior.

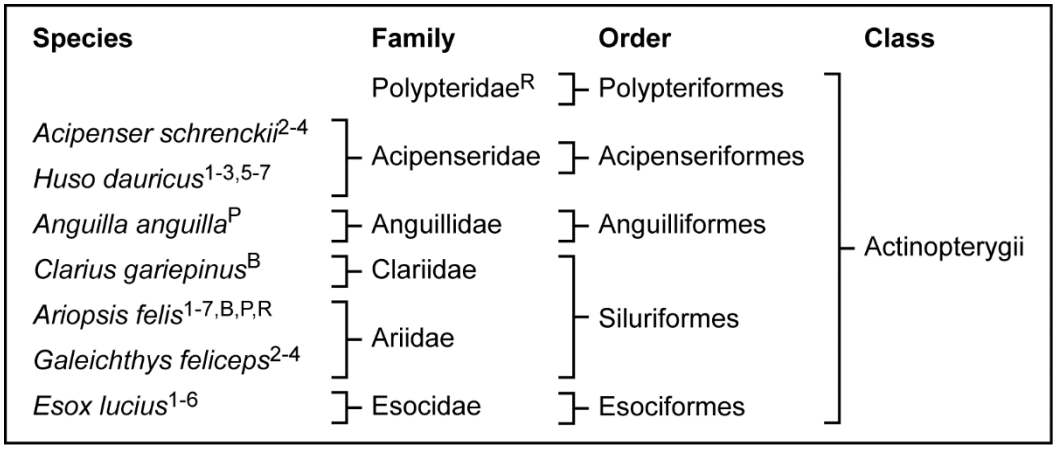

Fig. 21. Classification of the fishes considered in this report, and the features relevant to olfactory flow. Classification based on Nelson (2006). B: Lateral barbels may influence olfactory flow in resting fish; P: possesses pinnate olfactory rosette; R: respiration may influence olfactory flow in resting fish. 1: Incurrent nostril located in region of relatively high static pressure; 2: possesses nasal feature that impedes external flow; 3: excurrent nostril normal to external flow; 4: possesses feature that may accelerate flow over external nostril; 5: olfactory flow dispersed by jet impingement-like mechanism; 6: vortex may aid dispersal of olfactory flow; 7: resampling of olfactory flow by consecutive sensory channels.

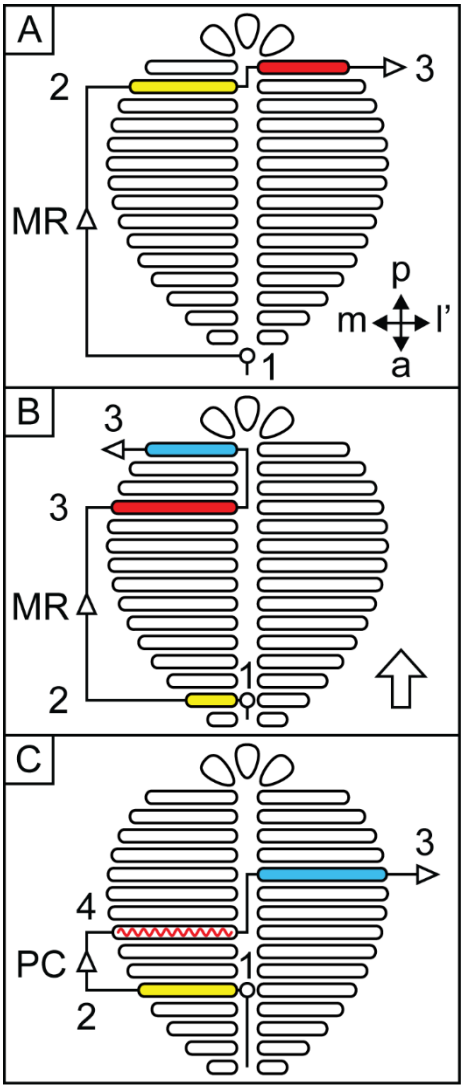

Fig. 22 Schematics of the four stages of dispersal of olfactory flow in the sea catfish. 1) Jet-impingement; 2) flow into a medial sensory channel; 3) inter-channel olfactory resampling; 4) intra-channel olfactory resampling. (A) – (C): Examples of three different dispersal pathways. Sensory channels (rounded rectangles) coloured according to whether streamline (small arrows) has passed previously through zero (yellow), one (red), or two (blue) sensory channel(s). Large arrow: direction of free-stream flow. Undulating red line: sensory channel vortex. White disk: point of impaction. a: Anterior; l': lateral; m: medial; MR: medial recess; p: posterior; PC: peripheral channel.

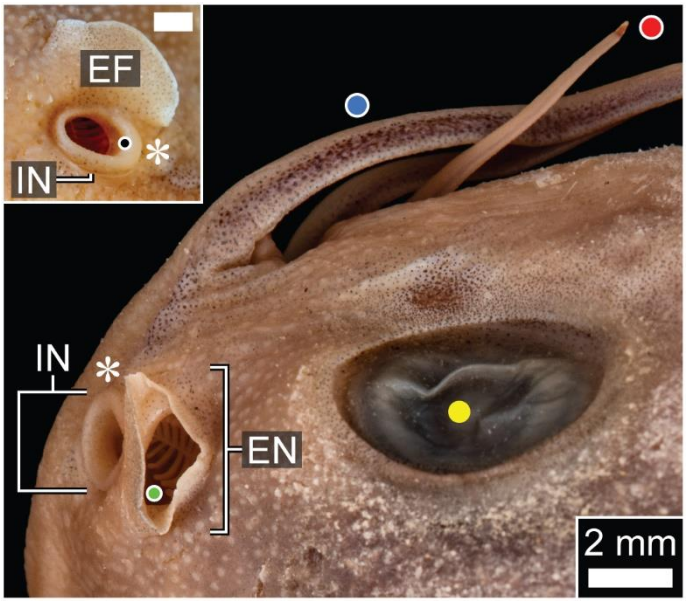

Fig. 23 *Left* dorsal aspect of head of *Galeichthys feliceps* (BMNH 2016.8.17.102). Inset: anterior aspect, left nasal region. Scale bar, inset: 1 mm. Asterisk: incurrent nasal flap. Green, black, yellow, blue and red disks: olfactory rosette, lateral wall of incurrent nostril, eye, lateral, and ventral barbels, respectively. EF: Excurrent nasal flap; EN: excurrent nostril; IN: incurrent nostril.

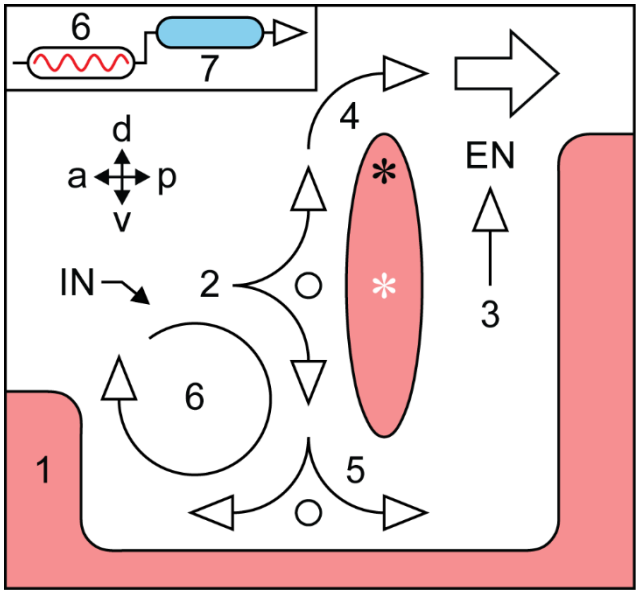

Fig. 24 Common elements (numbered) in the olfactory flow of the sturgeon, pike and sea catfish: 1) region of relatively high static pressure (pink); 2) nasal feature (white asterisk) that impedes external flow; 3) excurrent nostril normal to external flow (large arrow); 4) flow accelerated by nasal feature (black asterisk); 5) flow dispersed by jet impingement-like mechanism; 6) vortex; 7) inter-channel olfactory resampling (inset). Rounded rectangles (inset): sensory channels. Small arrows: direction of local flow. Undulating red line: sensory channel vortex. White disks: points of relatively high static pressure on nasal surfaces. a: Anterior; d: dorsal; EN: excurrent nostril; IN: incurrent nostril; p: posterior; v: ventral.

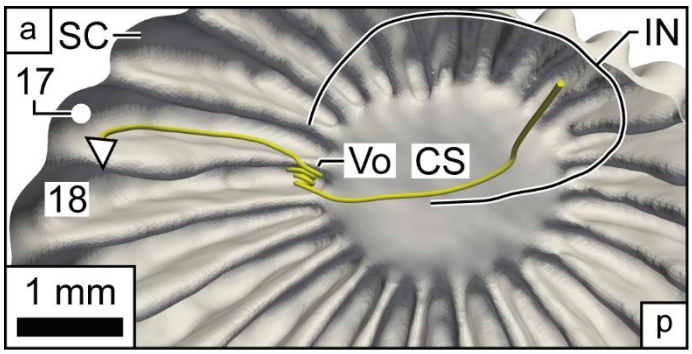

Fig. 25 Olfactory resampling in the sturgeon. Surface model of olfactory rosette of right nasal region of the sturgeon *Huso dauricus*. Shown is a CFD-generated streamline (yellow tube, direction indicated by arrow) passing from sensory channel 18 to sensory channel 17. Reynolds number: 500. For details of CFD simulation, see Garwood et al. (2019). a: Anterior; CS: central support; IN: position of incurrent nostril; p: posterior; SC: sensory channel; Vo: vortex.

Catalogue number[a]	*TL*[b] (cm)	Scale	Reynolds numbers[c]		Model type
BMNH 1983.7.6.12	13	5.5x life size	600 – 800	**Model 1A**	Off-white plastic, with translucent right nasal region
				Model 1B	Black plastic
		Life size	200, 300 and 700	**Model 1C**	Computational fluid dynamics
BMNH 1948.8.6.196	18	3.7x life size	600 – 700	**Model 2A**	Off-white plastic, with flexible barbels
				Model 2B	Black plastic

Table 1 Model heads of sea catfish, *Ariopsis felis*. a) Natural History Museum, London, UK. b) Total length (*TL*) of preserved specimen. c) For external olfactory flow (Section 2.9).

Reynolds number	Unique paths				Number of sensory channels
	Two	Three	Four	Total	
200	7	60	-	67	17
300	4	52	7	63	17
700	3	3	2	8	9

Table 2 Number of sensory channels and unique paths involved in inter-channel olfactory resampling. Yaw: 0°. See Section 3.3.2 for further explanation.

Species	Reynolds number(s)	Percentage dynamic pressure of free-stream flow harnessed[a]
Sea catfish, *Ariopsis felis*	200, 300 and 700	50[b]
Pike, *Esox lucius*	200 – 300	25 – 40[c]
Sturgeon, *Huso dauricus*	500	35[c]

Table 3 The percentage of the dynamic pressure of the free-stream flow harnessed by the nasal regions of the sea catfish, the pike and the sturgeon. a) To the nearest 5 or 10 %. b) For the right nasal region only, because this has a pristine excurrent nasal flap (Section 2.5). c) Percentages from Garwood et al., 2020.

Appendix A

A.1. Additional methodology

A.1.1. Micro-CT

The XT H 225 system used for the micro-CT scans was fitted with a 225 kV/225 W source and a PerkinElmer XRD 1621 detector. (The voltage stated for the source in Garwood et al., 2019 was incorrect: it should have been 225 kV, not 22 kV.) For each scan, the specimen was held in a truncated (140 mm height) 500 ml plastic measuring cylinder (inner diameter 48 mm), with the body axis vertical and the head uppermost. The region of interest (e.g. Fig. A.1A, region anterior to white marks) protruded from the top of the cylinder, so that the X-rays were not attenuated by the cylinder. Specimens BMNH 1948.8.6.195 and BMNH 1948.8.6.196 fitted tightly into the measuring cylinder, and were therefore deemed unlikely to undergo unwanted movements during the scan. However, specimens BMNH 1983.7.6.11 and BMNH 1983.7.6.12 fitted loosely into the measuring cylinder. To pack these two specimens tightly, they were placed in a plastic sleeve, wrapped in muslin in their pectoral fin area (Fig. A.1A, PF), and then put in the measuring cylinder. If necessary, excess preservative fluid in the nasal chamber, particularly from the sensory channels (Fig. 2C), was removed first with tissue and then with a pipette, by blowing air into the nasal chamber for up to 10 minutes. (This fluid would have blurred the lamellae in the resultant scan, because pixels corresponding to preservative fluid have intensities very similar to pixels corresponding to tissue stored in preservative fluid.) We checked with a magnifying lamp and a stereomicroscope that residual fluid had been removed. To prevent specimens BMNH 1948.8.6.195, BMNH 1983.7.6.11 and BMNH 1983.7.6.12 drying out during the scan, a plastic sleeve was placed over their heads (without touching them). However, we were unable to do this for BMNH 1948.8.6.196, because its head did touch the plastic sleeve. Therefore, to avoid excessive image processing of the scan at the mask-generating stage (Appendix A.1.2), we did not put a plastic sleeve over this specimen. The exposure time (single image) for each scan was 708 ms. The accelerating voltage and current were 75 kV and 70 μA, respectively, for the scans of BMNH 1948.8.6.195-196, and 70 kV and 85 μA for the scans of BMNH 1983.7.6.11-12. A total of 3142 projections were collected in a single 360° rotation at 0.114577° intervals. The projections were transformed into a 3D matrix using CT Pro 3D 2.2 (Nikon Metrology). Using the software Drishti (Version 2.6.3; Limaye, 2012), the contrast between pixels corresponding to biological tissue and those corresponding to air was

improved by making a non-linear adjustment to the histogram of greyscale values; each scan was then converted into a set of 8-bit TIFF images (Fig. 3A-C). The number of TIFF images in each dataset (Garwood et al., 2021a, 2021b, 2021c, and 2021d) is 1744 (BMNH 1948.8.6.195), 1868 (BMNH 1948.8.6.196), 1864 (BMNH 1983.7.6.11), and 1987 (BMNH 1983.7.6.12).

A.1.2. Surface models

A.1.2.1. Surface model of BMNH 1983.7.6.12 (Model 1)

TIFF images from the micro-CT scan of specimen BMNH 1983.7.6.12 were imported into ScanIP and segmented with the Threshold tool, creating a 'mask' of the complete head ('head' mask). For thresholding, we chose lower and upper values of 30 and 255, respectively, because they captured well pixels corresponding to the olfactory lamellae. We used the Floodfill and Paint tools to remove five of the barbels at or close to their bases (Fig. 7C, barbels 2 – 6). We did so because they were – based on our observations of the aquarium specimens (Fig. 5) – in unnatural positions (Fig. 1C), and might therefore adversely affect flow. The unnatural positions of the barbels were probably a result of storage. The left lateral barbel was in a more natural position, and consequently we removed only its distal tip (Fig. 7B, blue disk). To prevent this barbel snapping in the plastic model, the connection between it and the head (Fig. 7B, dashed line) was reinforced using the Paint tool. Two new masks were created from the head mask: a mask of the right nasal region ('nasal region' mask; Fig. 3D, Ma) and a mask of the remaining head ('partial head' mask). The nasal region mask was isolated from the head mask with the Floodfill tool. The partial head mask was generated with the Boolean operations tool by subtracting the nasal region mask from the head mask. To reduce the amount of image processing required for the next step, the pixel spacing of the partial head mask was adjusted with the Resample tool from 16 μm (16.43 μm to two decimal places) to 33 μm (32.86 μm to two decimal places). Internal cavities in both masks (e.g. in the oral cavity) were filled (to reduce the size of the STL file prior to 3D printing/conversion to the CFD mesh) using the Floodfill and Paint tools (filling the oral cavity sealed the mouth; Fig. 7C, Mo). The partial head mask and the nasal region mask were then duplicated. The original pair of masks was adjusted to 5.5x life size with the Rescale tool. The Paint tool was then used to put a hole in the back of the enlarged partial head mask (for the plastic model's aluminium peg, Appendix A.1.3.1). The two duplicated masks were not rescaled, i.e. remained life-sized. Finally, an intact 5.5x life-sized head mask (with

internal cavities filled, a hole in the back of it, and a pixel spacing of 33 μm) was created using the same techniques as above.

A surface model was created of each mask (head, nasal region, partial head) with the following features selected in ScanIP's 'Model configuration' dialogue box: a) 'General' tab → Smart mask smoothing (pre-processing) → Use greyscale values; b) 'Surface settings' tab → Triangle smoothing → Use triangle smoothing for masks (10 iterations); and c) 'Surface settings' tab → Decimation → Decimate box unticked. Each surface model was then exported in binary format as a stereolithography (STL) file.

The 5.5x life-sized STL models were used to make the plastic models for the dye visualisation experiments (Appendix A.1.5.1). The life-sized STL models of the right nasal region and partial head were used to make the CFD model (Appendix A.1.5.2.1).

STL files of the floor and roof of the right nasal chamber, together with the right nasal volume (the space occupied by water in the right nasal chamber), were created using the same methodology as above (see also Appendix A.1.5 of Garwood et al., 2019). All three STL files were derived from the high resolution (pixel spacing 16 μm) mask of the right nasal region, and were 16x life size.

A.1.2.2. Surface model of BMNH 1948.8.6.196 (Model 2)

The surface model of BMNH 1948.8.6.196 (Model 2) was generated in the same way as Model 1 (above), with several modifications, as follows. To generate STL models of manageable size for 3D printing, the pixel spacing of the set of TIFF images (Appendix A.1.1) was adjusted from 26 μm (25.84 μm to two decimal places) to 52 μm (51.69 μm to two decimal places) with the Resample tool (Fig. 3E, Ma). For thresholding, we chose lower and upper values of 25 and 255, respectively. The voxel size of the X-ray scan did not resolve the olfactory lamellar attachments to the nasal chamber wall in both nasal regions of the head mask (Fig. 3C, arrowhead). We therefore used the Paint tool to repair the resultant gaps and holes in these attachments. We were not, however, able to repair all these gaps (cf. Fig. 3D and E, arrowheads). We also used both Floodfill and Paint tools to: a) isolate the barbels near their bases, creating a 'barbels' mask (used to make Model 2A, below); and b) seal the back of the oral cavity (Fig. A.3D, filled white region). The hole on the ventral surface of the specimen (Fig. A.1C, asterisk) was replicated in the surface model (Fig. A.3C, asterisk). Because this hole was on the ventral surface, we assumed that it would have negligible effect

on olfactory flow. Therefore, we did not in the surface model fill this hole. The hole was likely to be postmortem damage.

Two variants of the head mask were made. The first ('head 1' mask, used to make Model 2A) was generated by subtracting with the Boolean operations tool the barbels mask from the original head mask. The second variant ('head 2' mask, used to make Model 2B) was generated from head 1 mask by a) trimming the bases of the four ventral barbels such that they were flush to the ventral surface, and b) restoring the two lateral barbels (although not to their full extent). Both operations were performed with the Floodfill, Paint, and 3D editing (Cuboid) tools, and both were done to minimise disruption to the flow in the plastic model. All three masks (head 1, head 2, barbels) were adjusted to 3.7x life size with the Rescale tool.

A.1.2.3. Surface models of BMNH 1983.7.6.11 and BMNH 1948.8.6.195

Surface models of BMNH 1983.7.6.11 and BMNH 1948.8.6.195 were created using the same methodology as for BMNH 1983.7.6.12 and BMNH 1948.8.6.196. We used the models of BMNH 1983.7.6.11 and BMNH 1948.8.6.195 to support our observations on the nasal anatomy of *Ariopsis felis*.

A.1.3. Plastic models

A.1.3.1. Plastic models of heads

All plastic models apart from Model 2A were 3D printed from the corresponding STL files according to the methodology of Abel et al. (2010). Model 2A was built as one part on a J750 PolyJet 3D printer (Stratasys, Eden Prairie, USA).

The opaque part (Fig. 7A, Op) of Model 1A (derived from the partial head mask; Appendix A.1.2.1) was made in off-white plastic (ABS-M30, Stratasys). Model 1A's translucent part (derived from the nasal region mask; Appendix A.1.2.1) was made in VisiJet SL Clear plastic (3D Systems, Rock Hill, USA). The layers arising from the 3D printing process were 178 μm thick in the opaque part and 50 μm thick in the translucent part. The two parts were glued together to give the complete model (Fig. 7A). The smooth joint between the translucent and opaque parts and the difference in the thickness of their layers did not appear to disrupt flow, based on the similar behaviour of the dye in the dye visualisation experiments and the streamlines in the CFD simulations (Fig. 13).

Model 2A (derived from the head 1 mask; Appendix A.1.2.2) was built from VeroWhitePlus (Stratasys). The barbels (derived from the barbels mask; Appendix A.1.2.2) were built from TangoPlus and VeroWhitePlus (Stratasys) in a ratio of 9:1 to give a hardness of 85 on the Shore A scale. Alone, VeroWhitePlus gave good contrast with the red dye used to visualise flow; in combination with TangoPlus it gave the barbels a degree of flexibility that to some extent reproduced their flexibility *in vivo*. The layers arising from the 3D printing of Model 2A were 30 μm thick.

Models 1B and 2B (from the STL file of each intact head; Appendices A.1.2.1 and A.1.2.2) were made in black plastic (ASA, Stratasys).

An aluminium peg (Fig. A.7A, Pe; see also Fig. 4 of Garwood et al., 2019) was inserted into the back of each model, allowing the model to be fixed to the rig used to suspend it in the flume. Model 2A was much heavier than the other models (1.1 kg *v.* ~ 0.17 – 0.29 kg). We mention this only as a practicality.

A.1.3.2. Plastic models of nasal region

To help visualise the nasal region and olfactory rosette of *A. felis* (specimen BMNH 1983.7.6.12), we prepared 16x life-sized plastic models of: a) the floor of the right nasal chamber (occupied chiefly by the olfactory rosette; Fig. A.5A); b) the roof of the right nasal chamber (Fig. A.5B and C); and c) the volume of the right nasal chamber (Fig. A.6). The models of the floor and roof of the nasal chamber fitted together to give the complete nasal region. The models were 3D printed according to the methodology of Abel et al. (2010). All nasal region models were made in off-white plastic (ASA).

A.1.4. Pitch, yaw, swimming speeds, and swimming behaviour of sea catfish

Pitch angles were estimated from footage of the aquarium specimens (Section 2.2) in which a specimen was ascending or descending. Yaw angles were estimated from footage in which a specimen was approaching directly the camera. Estimates of yaw angles did not include any discrepancy in height between the specimen and the camera. The pitch and yaw angles we observed were + 70° to - 90° and ± 10°, respectively.

The swimming speed (in *TL* s^{-1}, where *TL* is the total length of the specimen; Fig. 1A) of an aquarium specimen moving horizontally from one side of the aquarium to the other was estimated by placing a ruler alongside the aquarium and then measuring in the subsequent

video footage the time interval between the anterior tip of the specimen passing one end of the ruler and its posterior tip passing the same end. The aquarium specimens swam at speeds in the range 0.3 – 1.9 *TL* s^{-1} (mean = 0.6 *TL* s^{-1}, n = 39).

Our observations of the aquarium specimens largely support Zeiske et al.'s statement (1994) that *A. felis* is 'an almost permanent swimmer'. Of the five specimens, one was never observed resting. The other four were observed resting (i.e. were stationary on the floor of the aquarium) at least once. Of these four fish, two rested frequently, two infrequently.

A.1.5. Fluid dynamics

A.1.5.1. Dye visualisation

The working section (L x W x H) of the Eidetics Model 1520 flume was 152 cm x 38 cm x 51 cm. Each model was suspended in the flume via its aluminium peg using the rig described in Abel et al. (2010). The rig/peg arrangement also allowed the roll (Fig. 10.1 of Barnard and Philpott, 2004) of the model to be varied (Fig. A.7A, Rl). The models were positioned such that they were central (± 2 cm) width-wise to the working section of the flume. The maximum transverse cross-sectional area of each model was 90 cm^2 (Models 1A and B) and 91 cm^2 (Models 2A and B), both less than 5 % of the working cross-sectional area of the flume. The effect on flow in the vicinity of the model from the walls of the flume should therefore have been negligible, based on standard corrections (Barlow et al., 1999, p. 361). The posterior edge of each model was nine characteristic dimensions (Fig. 9C, *L*) downstream from the posterior edge of the excurrent nostril, a distance we considered sufficient to render upstream effects negligible.

Both the off-white and the black models were illuminated with a 500 W or 800 W halogen lamp supplemented on occasion with an LED light (Lezyne Micro Drive, 100 – 150 lumens). To help visualise dye, a white sheet was placed behind the off-white models and a black sheet behind the black models. The dye solution was introduced from a pressurised reservoir using stainless steel tubing (internal diameter 1.3 mm, external diameter 2 mm). The horizontal section of this tubing, from which dye was released, was 25 cm from the flume's floor. At a free-stream speed of 5 cm s^{-1}, dye emerged from the tubing as a well-defined filament, indicating that the exit velocity of the dye was equal to the local flow velocity (Fig. 3.1 of Lim, 2000). To minimise the effect of the tubing on flow over the model (Lim, 2000), the aperture of the tubing was located some distance (7 – 16 cm, and typically 10 cm) upstream

from the point of impingement on the model. The dye, as a filament, was directed at the dorsal surface of the head (Video clip 3). Note that the solution of the red food dye (which was not neutrally buoyant) and that of rhodamine 6G (which was neutrally buoyant) both gave the same results, e.g. both revealed the pair of vortices immediately anterior to Model 1 (Video clips 15 and 16).

A.1.5.2. Computational fluid dynamics

A.1.5.2.1. Generation of Model 1C (CFD model)

All the manipulations below were done with Geomagic Wrap (3D Systems) except the straightening of the olfactory lamellae, which was done with ZBrush 4R8 (Pixologic, Los Angeles, USA).

The high-resolution STL model of the right nasal region of Model 1 was fused to the low-resolution STL model of the head of Model 1 as follows. First, the right nasal region of the head model was selected with the Rectangle Selection Tool (Select Visible button active). (This measure ensured that the subsequent alignment step was to the right nasal region of the head, and not the left.) Next, the high-resolution right nasal region was broadly aligned to the right nasal region of the head (Alignment → Best Fit Alignment; all boxes in the Best Fit Alignment panel left unticked). To refine the alignment, this step was repeated (with in the Best Fit Alignment panel the Fine Adjustments Only box ticked). The Paint Brush Selection Tool was then used to paint an identical line (boundary) around the right nasal region of both models. The area within the boundary of the right nasal region of the head was then deleted, as was the region lying outside the boundary of the high-resolution right nasal region. The two models were then transformed into one object (Polygons → Combine → Combine). The high-resolution right nasal region was joined to the head with a series of bridging surfaces (Polygons → Fill Holes → Fill Single → Curvature → Bridge for the first surface, Complete for the final surface, and Partial for the intervening surfaces).

Each lateral line canal (Fig. 3A, circle) in the model was removed as follows. The segment of the canal that met the surface of the model was selected (Lasso Selection Tool, Select Visible and Select Backfaces Mode buttons active) and then deleted. Part of the remainder of the canal was selected (Lasso Selection Tool), the selection extended to the entire canal (Bounded Components), and the entire canal then deleted. The resultant hole in the surface of

the model was then filled to leave a smooth surface (Polygons → Fill Holes → Fill Single → Curvature → Complete).

Holes in the olfactory lamellae (Fig. A.8) were removed as follows. The Paint Brush Selection Tool was used to paint a line around the hole on one face of the lamella (Select Visible button active). Another line was painted around the same hole on the other side of the lamella. The area within each boundary was deleted (after selecting part of this area with the Paint Brush Selection Tool and then extending the selection to the entire area with the Bounded Components function), leaving two larger holes, one on each lamellar face. Each hole was filled (Polygons → Fill Holes → Fill Single → Curvature → Complete) to leave a smooth surface on each lamellar face, and an intact lamella.

Olfactory lamellar bridges (Fig. A.9) were corrected essentially in the same way as lamellar holes, painting around the base of the bridge on each lamella, deleting the resultant disconnected bridge, and then filling the two remanent holes such that the local curvature in the model was maintained.

A gap in an olfactory lamellar attachment (Fig. A.10) was corrected first by using the Paint Brush Selection Tool to paint a line around the gap (Select Visible button active), ensuring that the line stayed on each lamellar *face*, and did not stray into the gap (otherwise, when the gap was filled, the lamellar surface may have been pulled back into the gap). The area within the boundary was deleted as above (removal of olfactory lamellar holes). The gap was then filled by first creating a bridging surface across the top of the gap (Polygons → Fill Holes → Fill Single → Curvature → Bridge) and then filling the two resultant holes (Polygons → Fill Holes → Fill Single → Curvature → Complete).

The fused tips of olfactory lamellae 6, 7 and 8 (Fig. A.11) were, after separation, straightened according to the methodology of Agbesi et al. (2016b).

A.1.5.2.2. Simulations

The STL model resulting from the modifications in the previous section (Model 1C) was converted to a CFD mesh with the snappyHexMesh utility of OpenFOAM. The computational domain for the simulations had a velocity inlet, a pressure outlet, and dimensions (L x W x H) of 10.9 m x 2.05 m x 2.05 m. The model lay at the centre of the

domain in the transverse plane. The rostral tip was positioned 4.3 m from the velocity inlet. The size of the computational domain, together with the position of the model within it, were chosen to minimise flow artifacts from the walls of the domain. The no-slip condition was set for all solid surfaces, together with a symmetry plane (with a zero gradient of velocity and pressure across the plane) at the dorsal, ventral, and lateral surfaces of the domain. The Navier-Stokes equations governing transient and steady laminar flow were solved with the OpenFOAM algorithms PIMPLE and SIMPLEC, respectively. Solutions to the Navier-Stokes equations gave a field of velocity vectors.

Mass flow rates were converted to volumetric flow rates by dividing by the density of water used in the simulations (999.3 kg m^{-3}).

The terms 'pMean' and 'UMean' in Appendices A.1.5.2.3 – A.1.5.2.5 are the mean static pressure and the mean velocity over the last 500 iterations of the converged, time-averaged solution to the Navier-Stokes equations for a given simulation. The units of pMean when generated by the simulation are energy per unit mass. pMean was converted to the units of pressure (pascals) by multiplying by the density of water.

A.1.5.2.3. Pressure

Points of relatively high static pressure on the surface of the CFD model were located using ParaView's Find Data tool.

The average static pressure in each nostril ($P - P_0$ in Equation 1 of the main text) was calculated in ParaView by first using the Slice filter to put through the mesh a plane that passed through the nostril, and then applying to that plane the following succession of filters: Connectivity → Threshold → Calculator (Result Array Name: Pressure; subsequent box entry: density*pMean) → Integrate Variables. The average static pressure in the segment was then found in the Spreadsheet View by dividing the Pressure entry (Attribute: Point Data) by the Area entry (Attribute: Cell Data).

A.1.5.2.4. Streamlines

Streamlines were generated in ParaView by first applying to a line or point the Stream Tracer With Custom Source filter, with the following menu selections (selections in brackets): Vectors (UMean); Interpolator Type (Interpolator with Point Locator); Integration Direction (Both); Integrator Type (Runge-Kutta 4.5); Integration Step Unit (Cell Length); Initial Step

Length (0.2 m); Minimum Step Length (0.01 m); Maximum Step Length (0.2 m); Maximum Steps (2000); Maximum Streamline Length (0.2 m); Terminal Speed (10^{-12} m s^{-1}); Maximum Error (10^{-6}). The Tube filter was then applied to the Stream Tracer With Custom Source filter, with the following menu selections (selections in brackets): Scalars (Angular Velocity); Vectors (Normals); Number of Sides (6); Radius (10^{-5} m). Lines and points were created from the Sources menu (Point Source). Each line was placed in the superior part of the sensory channel. In the right nasal chamber the resolution of lines (i.e. the number of points from which streamlines were generated in each line) was as follows: channel 1 (4); channel 2 (19); channels 3 – 31 (9); channel 32 (14); and channel 33 (4).

A.1.5.2.5. Boundary layer

The vorticity contours used to gauge the thickness of the boundary layer on the surface of a model were generated in ParaView by applying the following succession of filters to the fluids file (selections in brackets): Compute Derivatives (Vectors: UMean; Output Vector Type: Vorticity; Output Tensor Type: Vector Gradient); Cell Data to Point Data; Calculator (Result Array Name: Vorticity; subsequent box entry: mag(Vorticity)); Slice; Contour (Contour by: Vorticity; Value Range: 50 [i.e. 50 s^{-1}]). Using this method, slices were placed through the CFD mesh (Fig. A.23) and a 50 s^{-1} vorticity contour generated in each (Figs. A.21 and A.22).

A.1.6. Reynolds numbers for olfactory flow through nasal chamber (CFD simulations)

The volumetric flow rate through each nasal chamber of *A. felis* was determined in ParaView by applying the following series of filters to the fluids.case file of the CFD model: Slice (Fig. 8D; location: Fig. A15B) → Connectivity → Threshold (to isolate the segment of the plane within the nasal chamber) → Surface Vectors (to select velocity vectors perpendicular to the nasal chamber segment); Constraint Mode: Perpendicular → Calculator (to determine the magnitude of the velocity vectors); Result Array Name: Magnitude UMean; subsequent box entry: mag(UMean) → Integrate Variables. The volumetric flow rate was the entry under 'Magnitude UMean' in the Spreadsheet View for the Integrate Variables filter (Attribute: Point Data). The wetted perimeter of the nasal chamber was calculated by applying the following series of filters to the surfaces.case file of the CFD model: Slice (location: Fig. A15B) → Connectivity → Threshold (to isolate the perimeter of the nasal chamber) → Integrate Variables. The perimeter of the nasal chamber was the entry under 'Length' in the Spreadsheet View for the Integrate Variables filter (Attribute: Cell Data).

A.1.7. Olfactory sensory surface areas

The sensory surface area of each olfactory rosette of specimen BMNH 1983.7.6.12 was determined in ParaView, as follows. Starting from the surfaces.case file of a CFD simulation, individual sensory channels, or groups of 2 – 5 sensory channels, were isolated by applying the Clip filter several times, and then applying the following set of filters: Merge Blocks → Connectivity → Threshold → Integrate Variables. The surface area of the isolated sensory channel(s) was then found in the Spreadsheet View (Attribute: Cell Data, Area entry). The sensory surface area of the olfactory rosette was then calculated by summing the areas of the isolated sensory channel(s) and is given to one significant figure in the main text.

A.2. Further limitations of this study

1) Some streamlines in the CFD simulations terminated prematurely (e.g. Fig. 19D, arrowhead). The termination was consistent between simulations. For example, streamlines in the first and last sensory channels of both the left and the right olfactory rosettes always terminated prematurely. The reason given by ParaView for the premature termination (ReasonForTermination, from variable chooser in toolbar) was that the streamline crossed the exterior boundary of the input dataset (ReasonForTermination = 1).

2) The models were rigid. We were therefore unable to use the models to investigate the mobility of the excurrent nasal flap, the lateral excurrent nasal flap and the medial excurrent nasal flap (Fig. 10B), all of which were mobile in the aquarium specimens. (The mobility of the excurrent nasal flap is described in Section 4.3. The lateral and medial excurrent nasal flaps could 'flutter' either when a specimen was resting or when it swam forward.)

3) Whereas *in vivo* the eyes of *A. felis* are convex (Fig. 5A, inset), the eyes of the preserved specimens had collapsed to a flattened state (Fig. 4, yellow disks). We did not in our models attempt to restore the eyes to their convex *in vivo* states (Fig. 6, yellow disks). We note, however, that a lack of convexity in the eyes of a model of a pike had only a minor effect on olfactory flow, and did not affect the passage of flow through the nasal chamber (Garwood et al., 2020).

4) We did not try to replicate the complex *in vivo* behaviour of the barbels (Fig. 5). We were, however, able to use a plastic model to show that both rigid and flexible versions of the barbels (in unnatural positions) did not impede flow through the nasal chamber (e.g. Video

clip 3). In the models with truncated barbels, flow recirculated in the area dorsal to the truncated barbel (Video clip 13). This recirculation may have encouraged flow through the nasal chamber.

5) We did not try to replicate respiratory flow in the models. The mouth of one of the models (Model 2) was open (Fig. A.3D, Appendix A.4), reflecting the normal state of the mouth *in vivo* (Fig. 5A and B). The posterior section of the oral cavity of this model had, however, been sealed when the model was prepared (Fig. A.3D, filled white region, Appendix A.4). Thus, flow through the oral cavity of Model 2 was prevented in the dye visualisation experiments. The vortex observed in the oral cavity of Model 2 in these experiments (Video clip 14) was undoubtedly a result of the sealed oral cavity. This vortex is unlikely to be present *in vivo*. Instead, the respiratory pump would generate a continuous flow of water through the oral cavity. The mouth of the other model (Model 1) was also sealed during its preparation (Fig. 7C; Appendix A.1.2.1), again blocking flow through the oral cavity.

The other limitations of this study are the same as those encountered and discussed in our previous studies (Abel et al., 2010; Agbesi et al., 2016a; Garwood et al., 2019).

A.3. Additional references

Garwood, R.J., Behnsen, J., Maclaine, J.S., Cox, J.P.L., 2021a. TIFF images from X-ray scan of head of *Ariopsis felis* (BMNH 1948.8.6.195). Mendeley Data, v1. http://dx.doi.org/10.17632/ys24bwfzks.1.

Garwood, R.J., Behnsen, J., Maclaine, J.S., Cox, J.P.L., 2021b. TIFF images from X-ray scan of head of *Ariopsis felis* (BMNH 1948.8.6.196). Mendeley Data, v1. http://dx.doi.org/10.17632/z6z4dsfdk6.1.

Garwood, R.J., Behnsen, J., Maclaine, J.S., Cox, J.P.L., 2021c. TIFF images from X-ray scan of head of *Ariopsis felis* (BMNH 1983.7.6.11). Mendeley Data, v1. http://dx.doi.org/10.17632/msmdg75fpp.1.

Garwood, R.J., Behnsen, J., Maclaine, J.S., Cox, J.P.L., 2021d. TIFF images from X-ray scan of head of *Ariopsis felis* (BMNH 1983.7.6.12). Mendeley Data, v1. http://dx.doi.org/10.17632/gbzy34knkj.1.

Lim, T.T., 2000. Dye and smoke visualization. In: Smits, A.J., Lim, T.T. (Eds.), Flow Visualization. Imperial College Press, London, pp. 43-72.

Limaye, A., 2012. Drishti: a volume exploration and presentation tool. In: Stock, S.R. (Ed.), Proceedings SPIE 8506, Developments in X-ray Tomography VIII, 85060X.

A.4. Additional figures

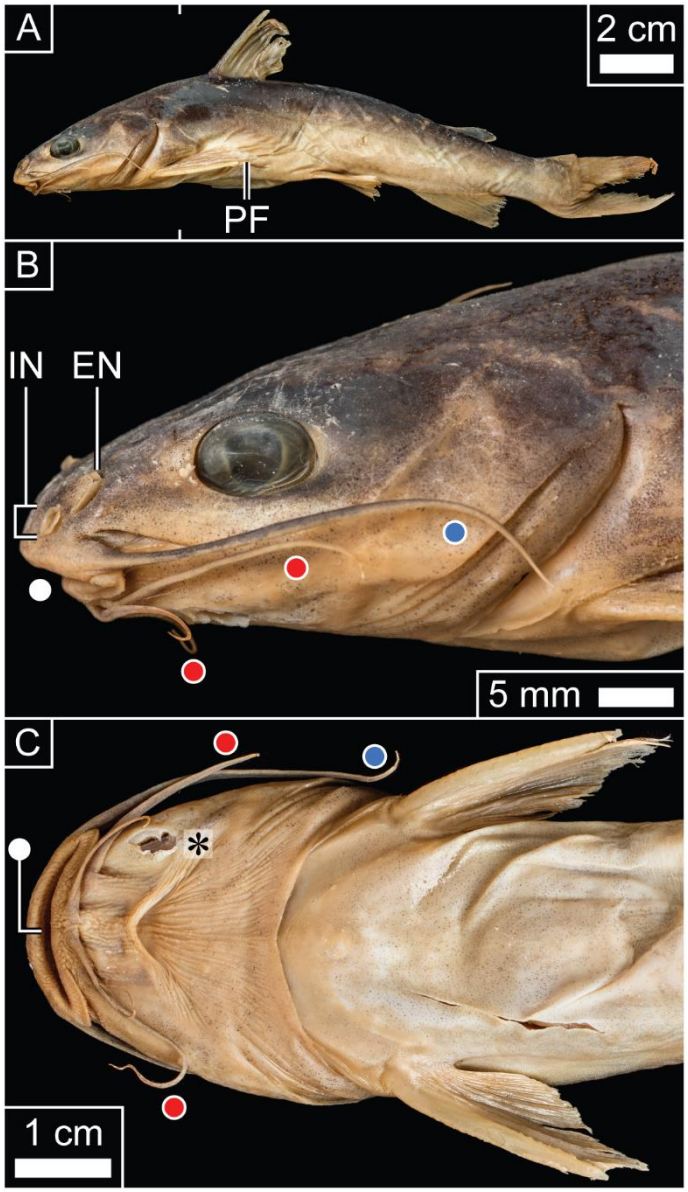

Fig. A.1. Preserved specimen of sea catfish (*Ariopsis felis*, BMNH 1948.8.6.196) used to generate model for dye visualisation. (A) Complete specimen. White marks: posterior extent of X-ray scan. (B) and (C): Lateral and ventral aspects of head, respectively. Asterisk in (C): hole. White, blue and red disks: mouth, lateral and ventral barbels, respectively. EN: Excurrent nostril; IN: incurrent nostril; PF: pectoral fin.

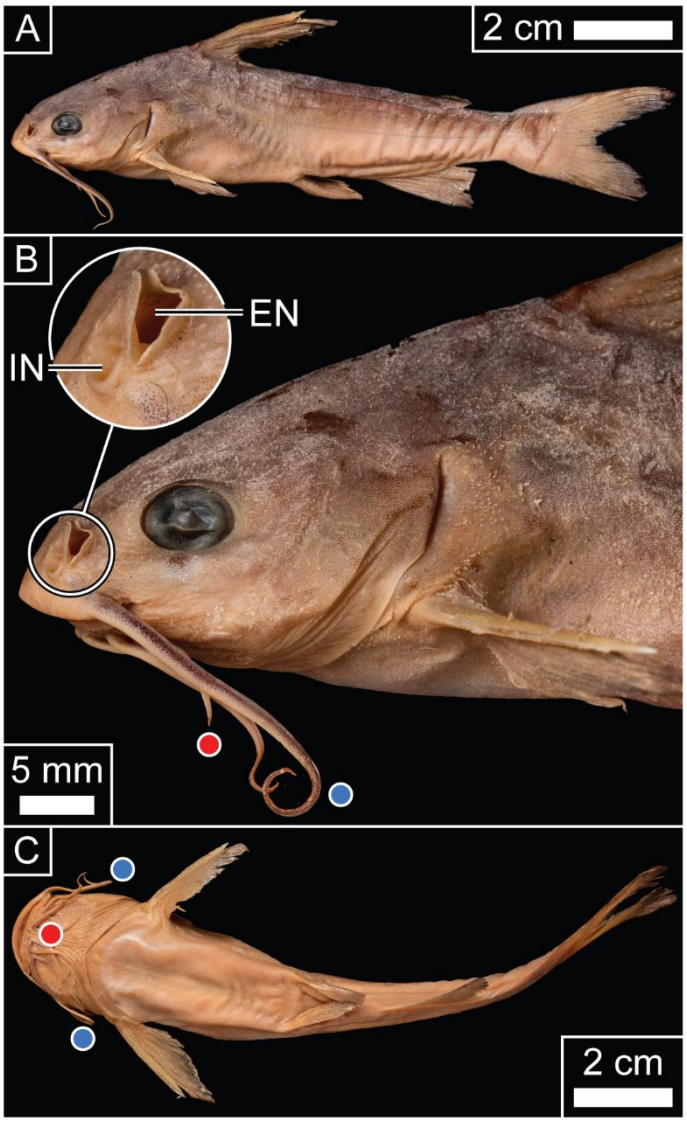

Fig. A.2. Preserved specimen of sea catfish (*Galeichthys feliceps*, BMNH 2016.8.17.102). (A) Complete specimen. (B) and (C): Lateral and ventral aspects of head, respectively. Inset in (B): detail of nasal region. Blue and red disks: lateral and ventral barbels, respectively. EN: Excurrent nostril; IN: incurrent nostril.

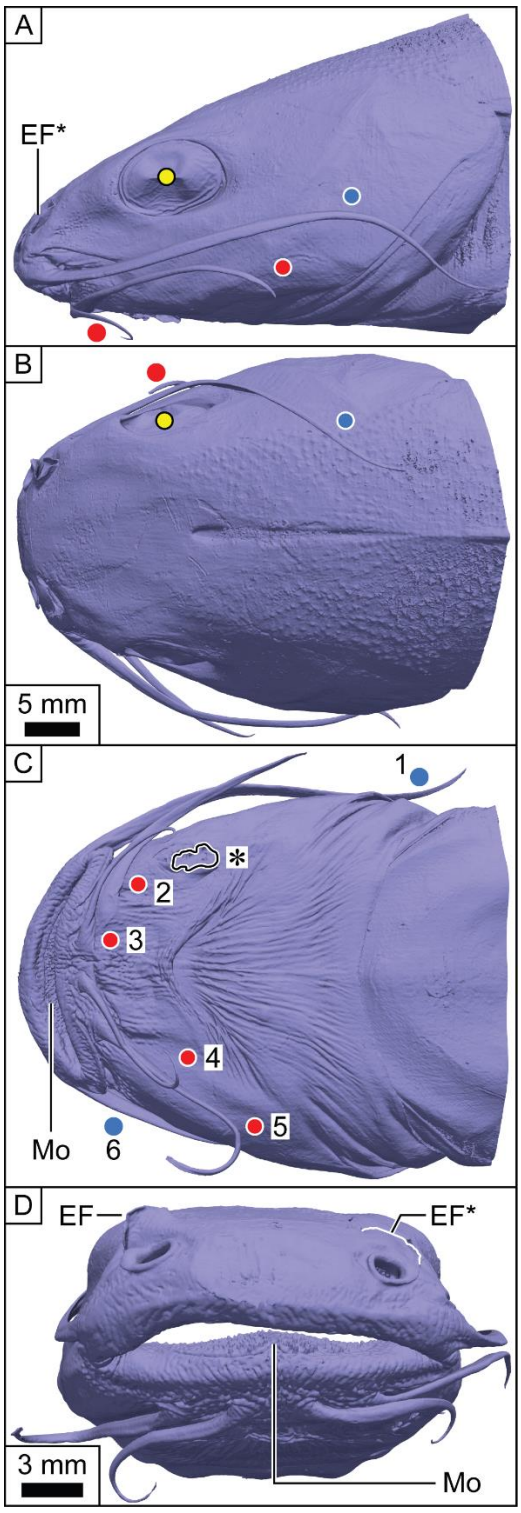

Fig. A.3. Surface model of head of sea catfish. Model derived from specimen BMNH 1948.8.6.196. (A) Lateral aspect. (B) Dorsal aspect. Scale bar applies also to (A) and (C). (C) Ventral aspect. Asterisk: hole. (D) Anterior aspect. Interior white region: sealed oral cavity (Appendix A.1.2.2). Yellow, blue and red disks: eye, lateral and ventral barbels, respectively. Barbels numbered in (C). EF and EF*: Elevated and depressed excurrent nasal flaps, respectively; Mo: mouth.

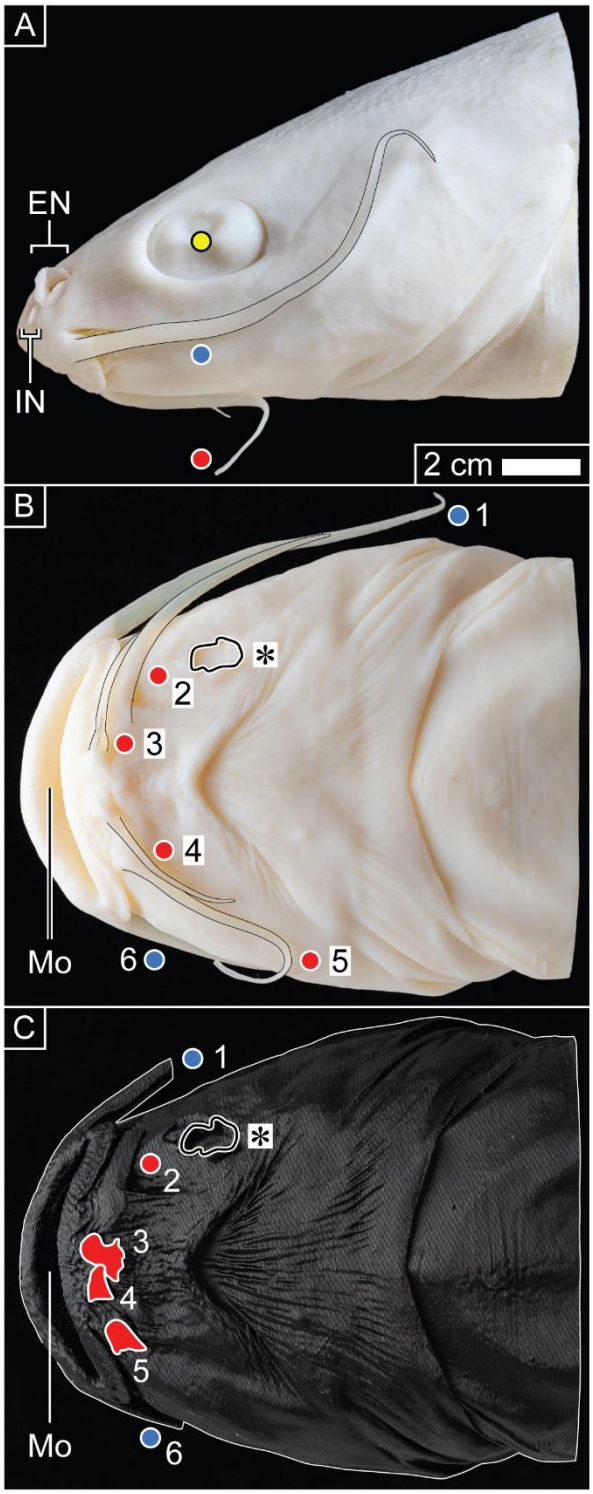

Fig. A.4. Plastic models of head of sea catfish. Models derived from specimen BMNH 1948.8.6.196. (A) and (B): Lateral (*right*) and ventral aspects, respectively, of Model 2A. Scale bar in (A) applies to all panels. (C) Ventral aspect of Model 2B. Red regions: truncated ventral barbels. Some barbels outlined in black in (A) and (B), and all barbels numbered in (B) and (C). Asterisk in (B) and (C): hole. Yellow, blue and red disks: eye, lateral and ventral barbels, respectively. EN: Excurrent nostril; IN: incurrent nostril; Mo: mouth.

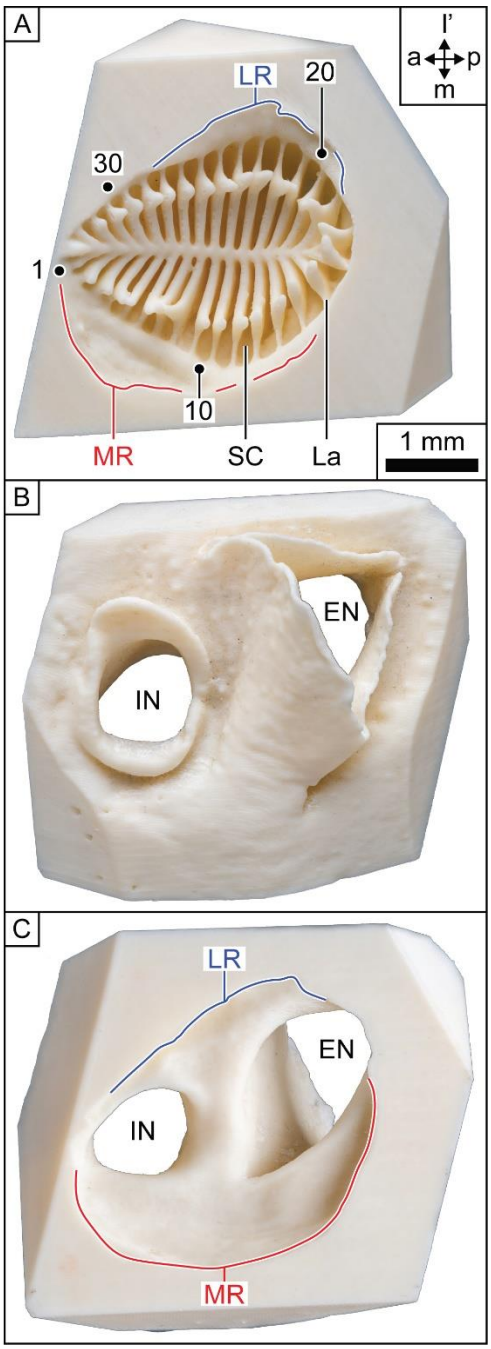

Fig. A.5. Plastic models of right nasal chamber of sea catfish (derived from specimen BMNH 1983.7.6.12). (A) Dorsal aspect of floor of nasal chamber. Selected sensory channels numbered. Extremities of medial and lateral recesses outlined in red and blue, respectively. (B) and (C): Dorsal and ventral aspects of roof of nasal chamber, respectively. Scale bar in (A) applies also to (B) and (C). Although the plastic models are 16x life size, the scale bar refers to the life-sized features. a: Anterior; EN: excurrent nostril; IN: incurrent nostril; l': lateral; La: olfactory lamella; LR: lateral recess; m: medial; MR: medial recess; p: posterior; SC: sensory channel.

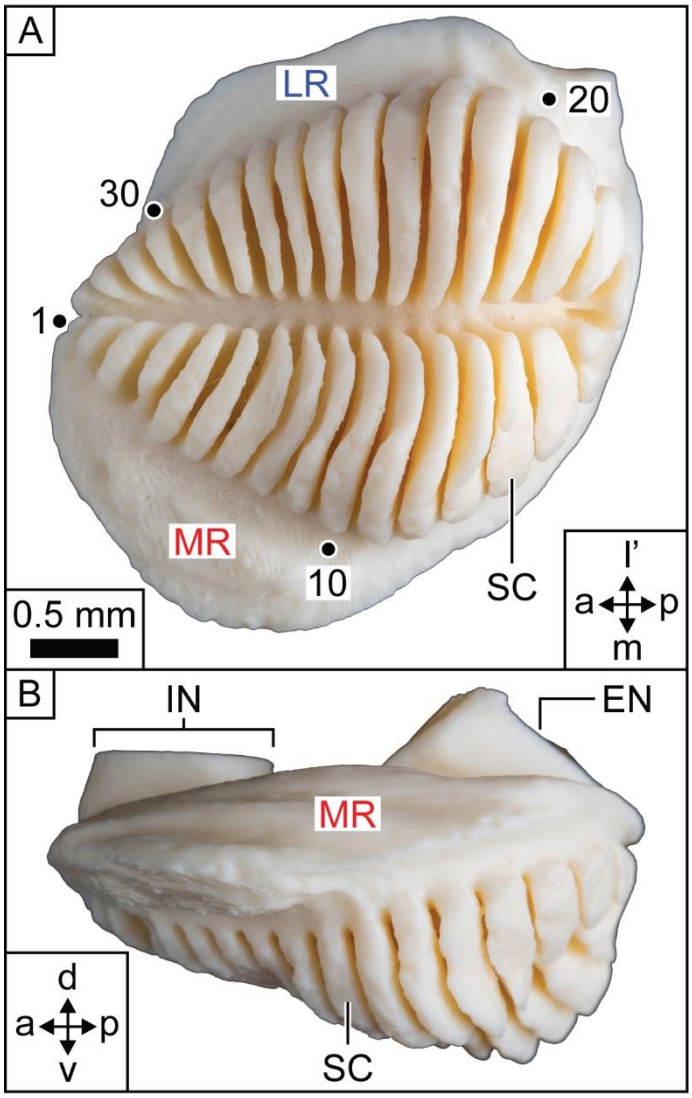

Fig. A.6. Plastic model of right nasal volume of sea catfish (derived from specimen BMNH 1983.7.6.12). (A) Ventral aspect. Scale bar applies also to (B). Although the plastic model is 16x life size, the scale bar refers to the life-sized nasal volume. Selected sensory channels numbered. (B) Medial aspect. a: Anterior; d: dorsal; EN: excurrent nostril; IN: incurrent nostril; l': lateral; m: medial; LR: lateral recess; MR: medial recess; p: posterior; SC: sensory channel; v: ventral.

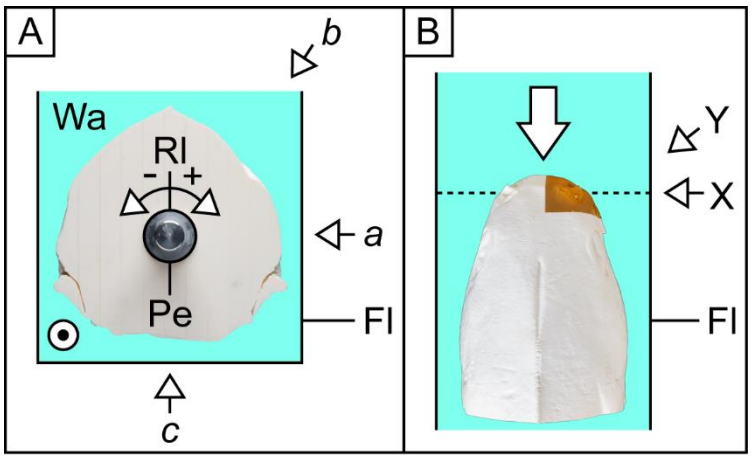

Fig. A.7. Camera positions and roll angle in the dye visualisation experiments. (A) Transverse cross-section of flume, showing posterior face of plastic model (Model 1A) of sea catfish. (B) Dorsal aspect of flume/plastic Model 1A. Circular symbol (A) and large arrow (B): direction of free-stream flow (out of page for circular symbol). Arrows *a*, *b*, *c*, X (also dashed line) and Y: camera positions. Images not to scale. Fl: Flume (and its most convenient viewing face); Pe: aluminium peg; Rl: roll angle; Wa: water.

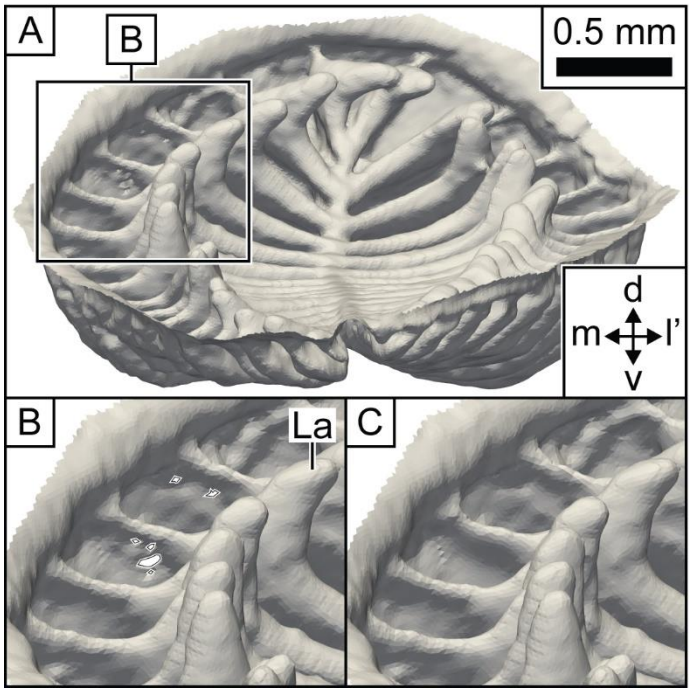

Fig. A.8. Removal of holes in the olfactory lamellae of the sea catfish CFD model. (A) Anterior view of right olfactory rosette. (B) Holes (white regions) in the olfactory lamellae. (C) Same image as (B), with holes repaired. Scale bars in (B) and (C) omitted for clarity. d: Dorsal; l': lateral; La: olfactory lamella; m: medial; v: ventral.

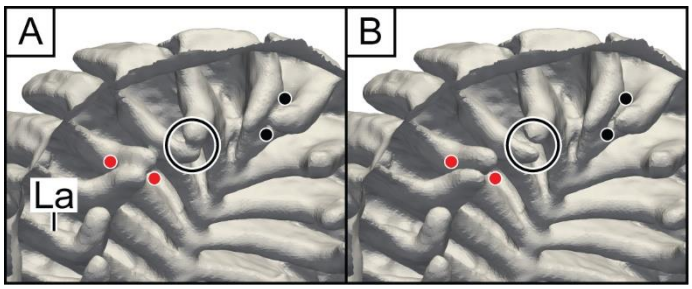

Fig. A.9. Removal of bridges between olfactory lamellae of sea catfish CFD model. Superior views of posterior right olfactory rosette. (A) Bridges between olfactory lamellae. Bridge in centre of image circled. Two other bridges are indicated between the pair of red disks and the pair of black disks. (B) Same image as (A), with bridges removed. Scale bar and anatomical compass omitted for clarity. La: Olfactory lamella.

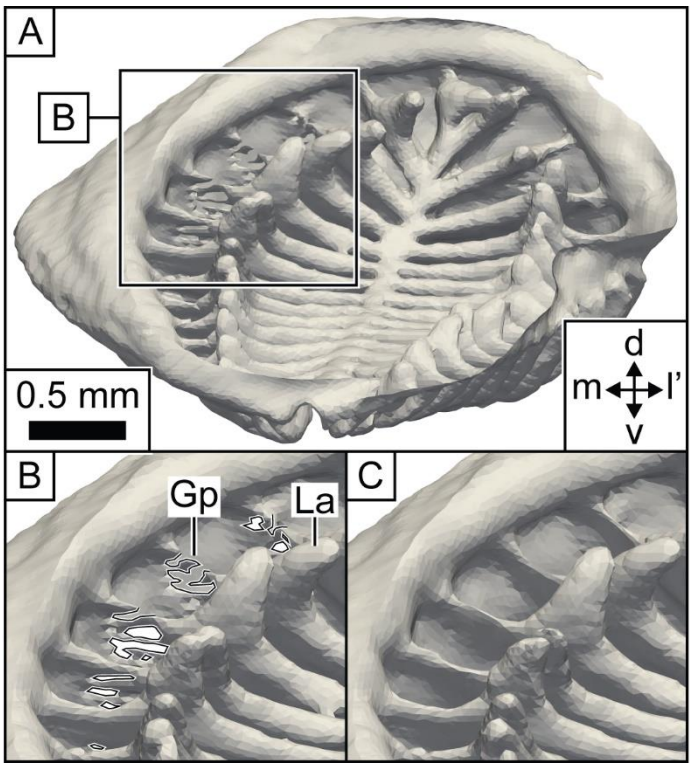

Fig. A.10. Removal of gaps in the olfactory lamellar attachments of the sea catfish CFD model. (A) Anterior view of left olfactory rosette. (B) Gaps (black outlines) and holes (white regions) in the olfactory lamellae. (C) Same image as (B), with gaps and holes repaired. Scale bars in (B) and (C) omitted for clarity. d: Dorsal; Gp: gap; l': lateral; La: olfactory lamella; m: medial; v: ventral.

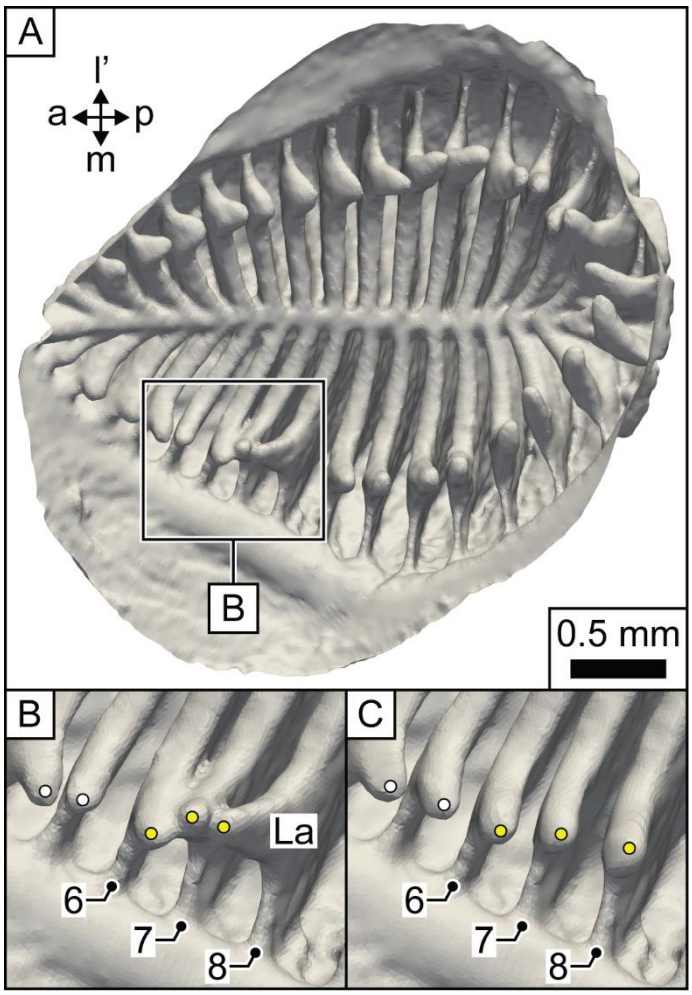

Fig. A.11. Separation and straightening of the tips of three olfactory lamellae (6 - 8) in the sea catfish CFD model. (A) Superior view of right olfactory rosette (context for panels B and C). (B) and (C): the three lamellar tips (yellow disks) before and after adjustments, respectively. The tips of olfactory lamellae 4 and 5 (white disks) have also been adjusted to conform to the general direction of the other lamellar tips. a: Anterior; l': lateral; La: olfactory lamella; m: medial; p: posterior.

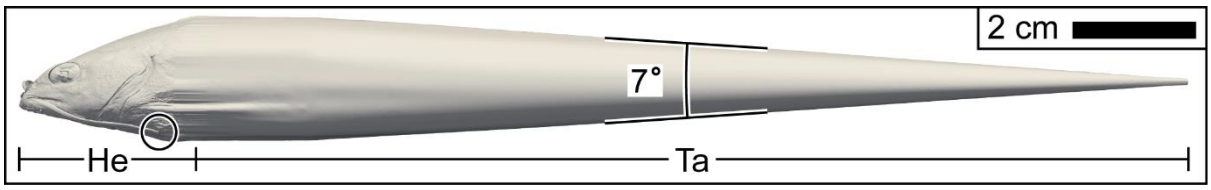

Fig. A.12. CFD model of sea catfish. Circle: truncated lateral barbel. He: Head; Ta: tapered extension (‘tail’).

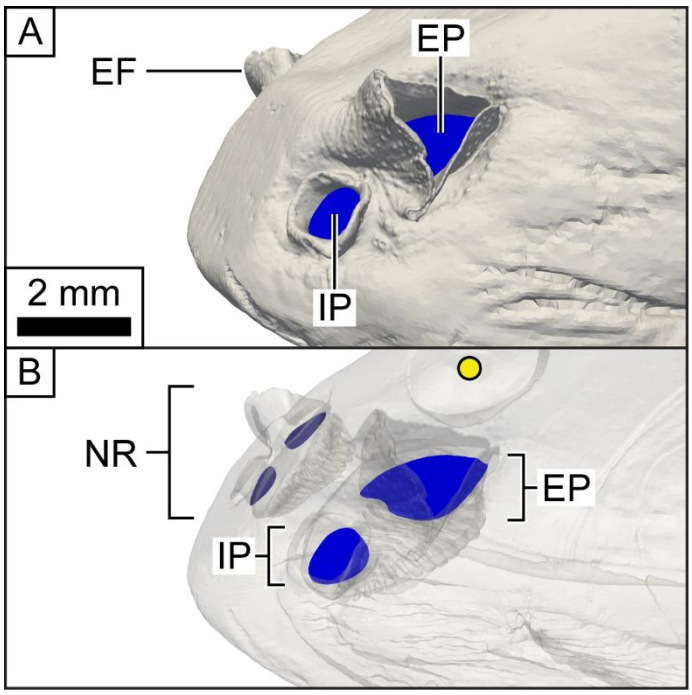

Fig. A.13. Nasal planes used to monitor volumetric flow rate through nasal chambers of sea catfish CFD model (Fig. A.14). Model of sea catfish head (*right* lateral aspect) with stereolithography model of each nasal plane (blue) superimposed. Head at 100 % (A) and 20 % (B) opacity. Scale bar in (A) applies also to (B). Yellow disk: *left* eye. EF: Excurrent nasal flap; EP and IP: stereolithography models of nasal planes in excurrent and incurrent nostrils, respectively; NR: *left* nasal region.

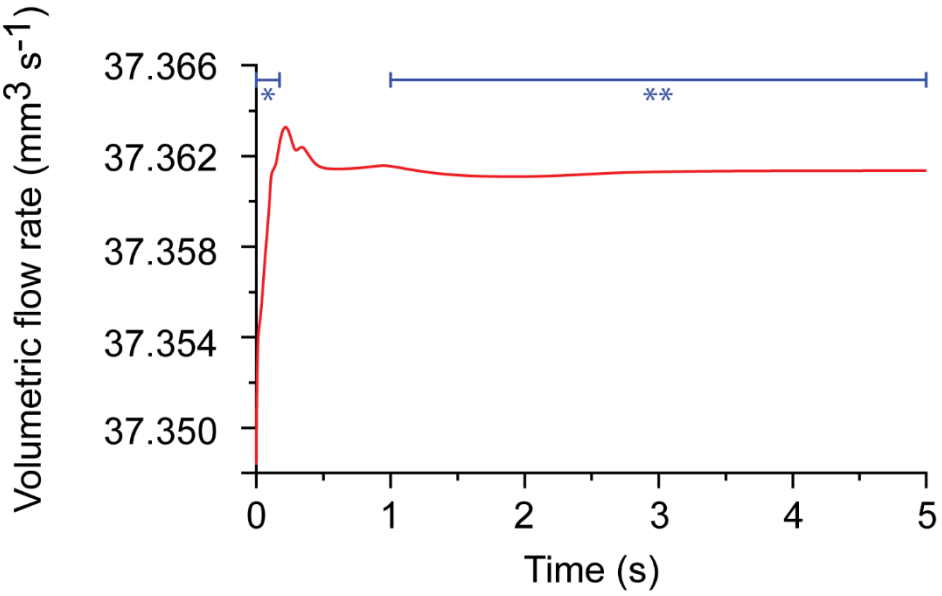

Fig. A.14. Variation in volumetric flow rate in transient CFD simulation of model of the sea catfish. Reynolds number: 300. Yaw: 0°. The volumetric flow rate was monitored in a plane through the right incurrent nostril (Fig. A.13B, EP). Red line: variation in volumetric flow rate. Blue line/single asterisk: time taken in the steady-state simulation for the nasal chamber to be flushed once. Blue line/double asterisk: period over which for all simulations the volumetric flow rate varies by ≤ 0.0007 % of the average volumetric flow rate for the same period.

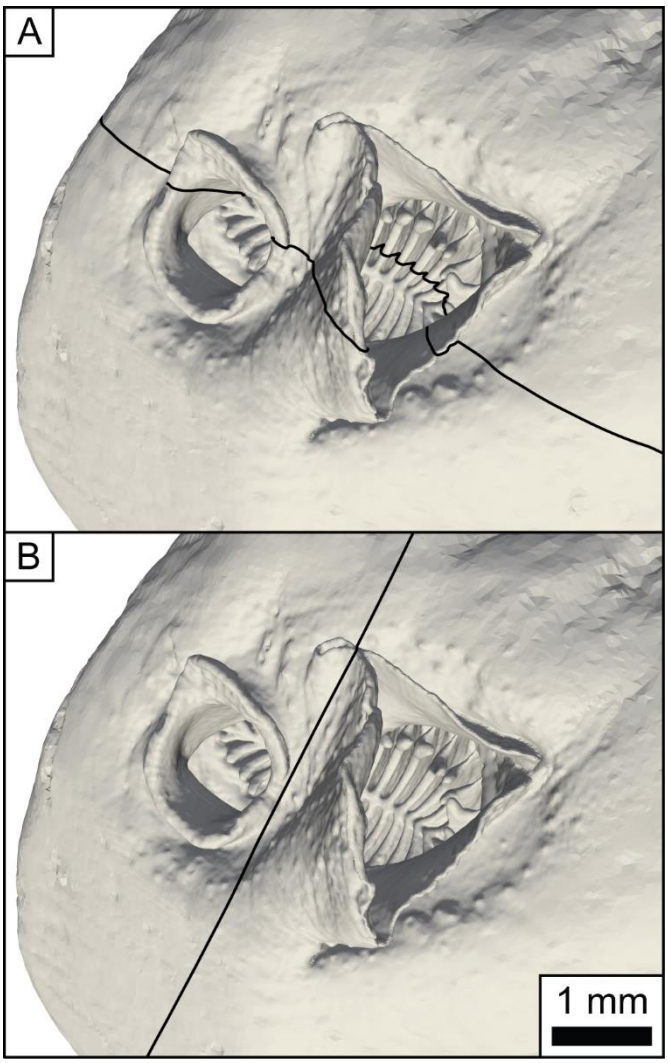

Fig. A.15. Locations of slices (black lines) in (A) Figs. 8B and 15, and (B) Fig. 8D. Views identical to Fig. 8A. Scale bar in (B) applies also to (A).

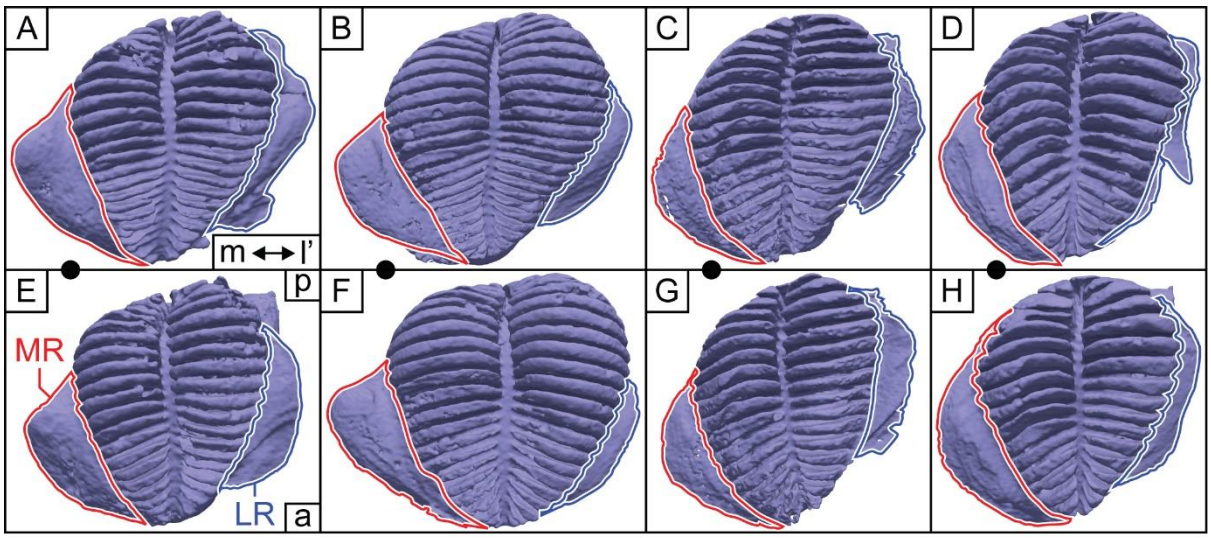

Fig. A.16. Medial and lateral recesses of nasal chambers of sea catfishes. Each panel shows the ventral aspect of a stereolithography model of a nasal volume (Appendix A.1.2) of a sea catfish specimen from the Natural History Museum, London, UK (catalogue numbers below). (A) - (D): volumes of left nasal chamber. (E) - (H): volumes of right nasal chamber. (A) and (E): Specimen BMNH 1948.8.6.195. (B) and (F): Specimen BMNH 1948.8.6.196. (C) and (G): Specimen BMNH 1983.7.6.11. (D) and (H): Specimen BMNH 1983.7.6.12. Scale bars omitted for clarity. Black disks indicate a pair of nasal volumes from the same specimen. a: Anterior; l': lateral; LR: lateral recess; m: medial; MR: medial recess; p: posterior.

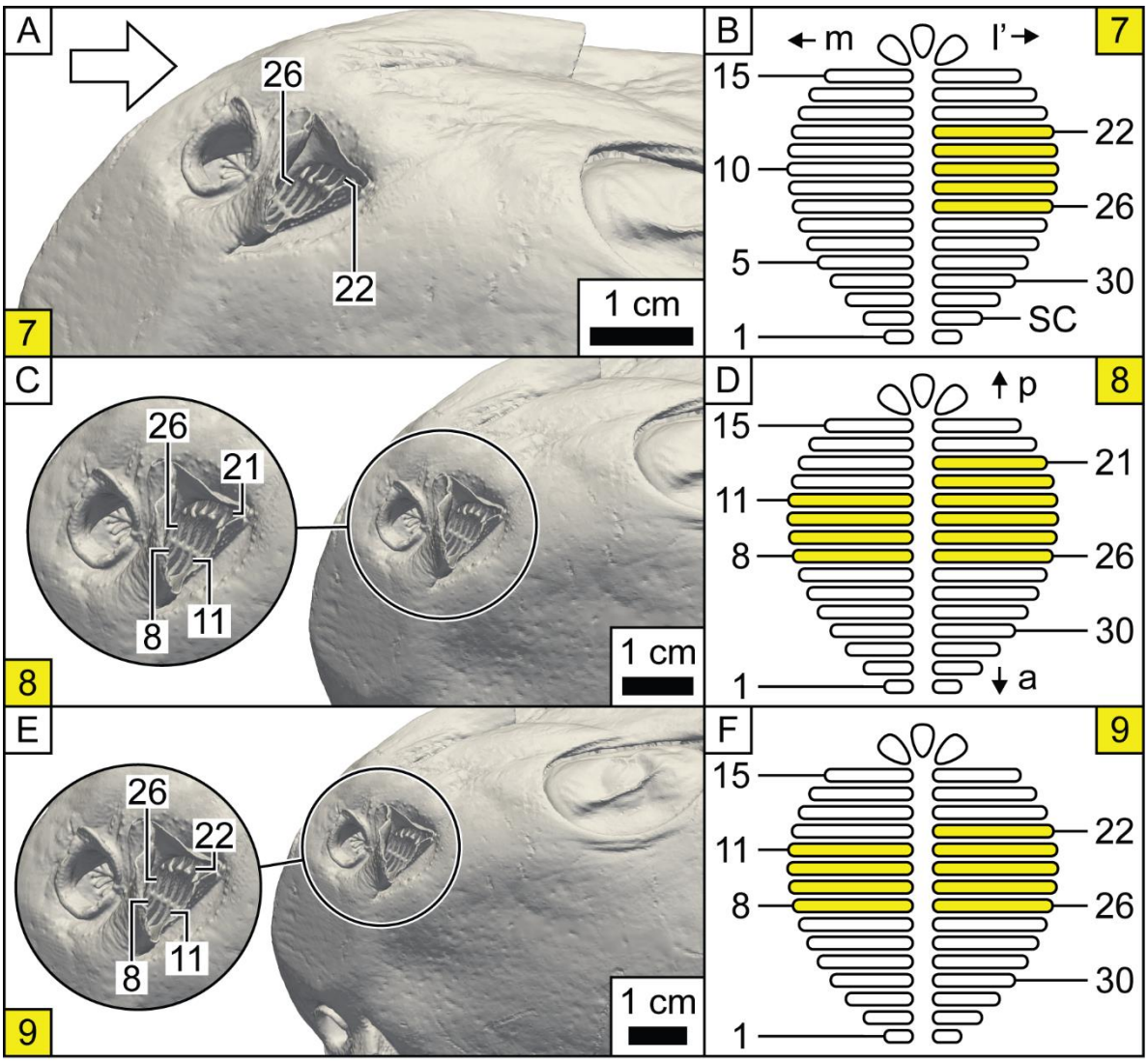

Fig. A.17. Sensory channels of plastic model (Model 1A) of the sea catfish that in the dye visualisation experiments are both visible and potentially irrigated. Selected sensory channels numbered. (A), (C) and (E): Surface model representation of Model 1A. Insets in (C) and (E): magnified nasal region. Arrow: direction of free-stream flow. (B), (D) and (F): Schematics of right olfactory rosette. Each schematic shows the sensory channels (yellow rounded rectangles) that are both visible and potentially irrigated in Video clips 7 – 9 (number of each clip given in yellow box). a: Anterior; l': lateral; m: medial; p: posterior; SC: sensory channel.

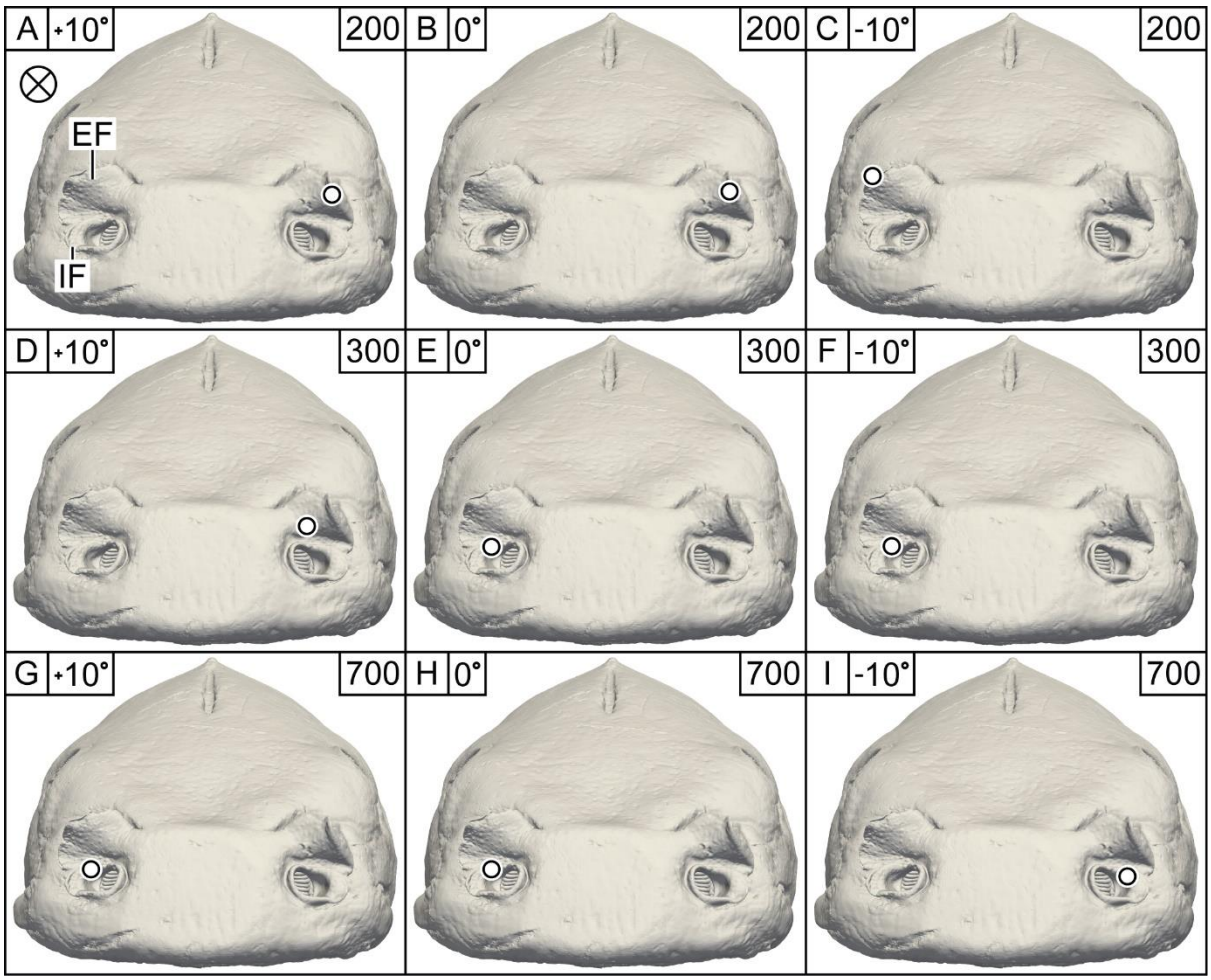

Fig. A.18. Location of stagnation points in CFD simulations. Anterior aspect of sea catfish CFD model (same aspect as Fig. 6C). Scale bar omitted for clarity (see Fig. 6C for scale). Cross: direction of free-stream flow (into page). Left boxed number in each panel: yaw angle. See Fig. 6B for definition of yaw angle. Right boxed number: Reynolds number. White disk: stagnation point. EF: Excurrent nasal flap; IF: incurrent nasal flap.

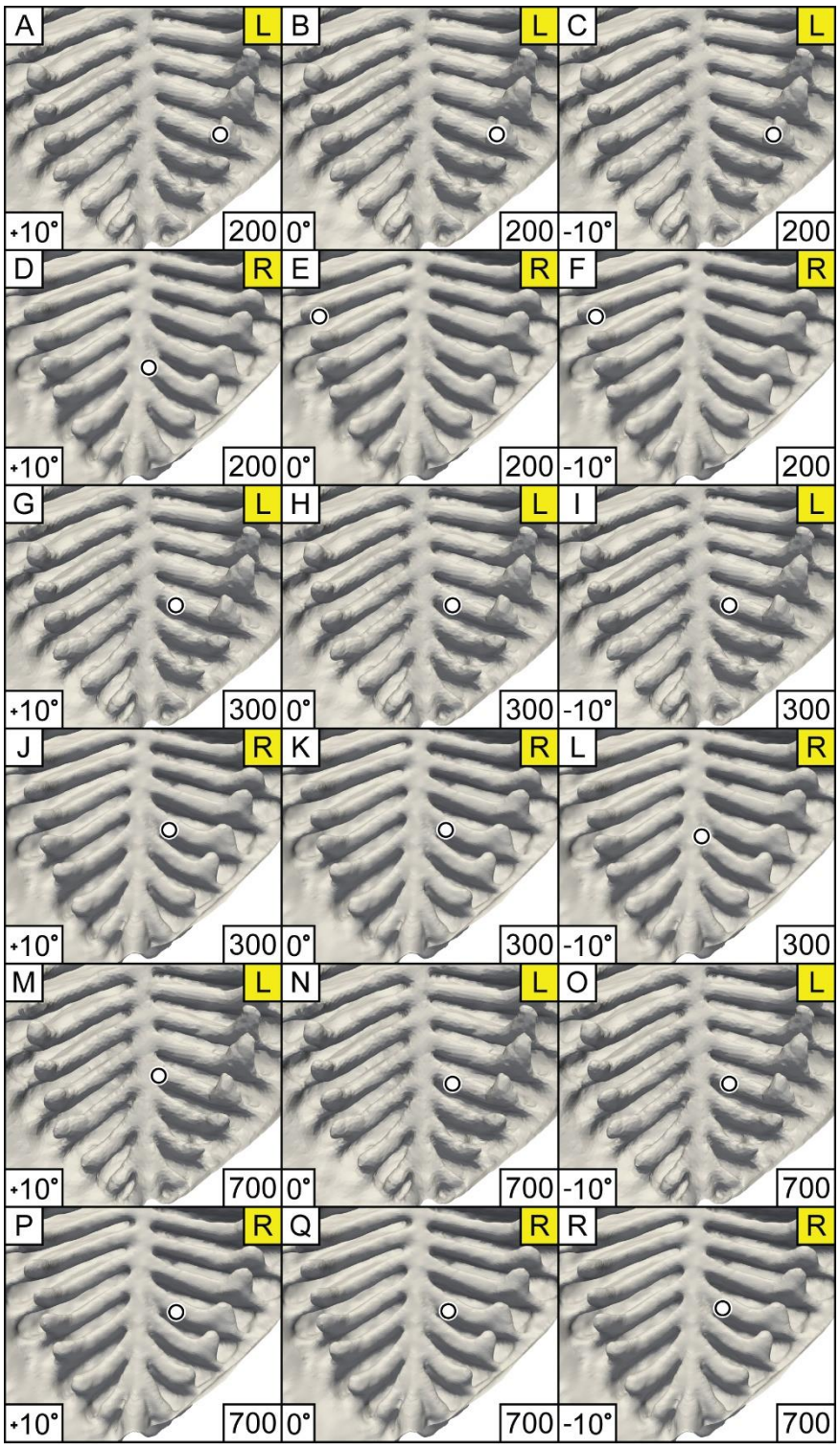

Fig. A.19. Location in CFD simulations of points of highest static pressure on floor of sea catfish nasal chambers. Each image shows a section from either the left (L, yellow box) or right (R, yellow box) nasal chamber of the CFD model. Left and right boxed numbers in each panel: yaw angle and Reynolds number, respectively. White disk: point of highest static pressure on floor of nasal chamber. See Fig. A.20 for labels, scale bar and anatomical compass, which are omitted here for clarity.

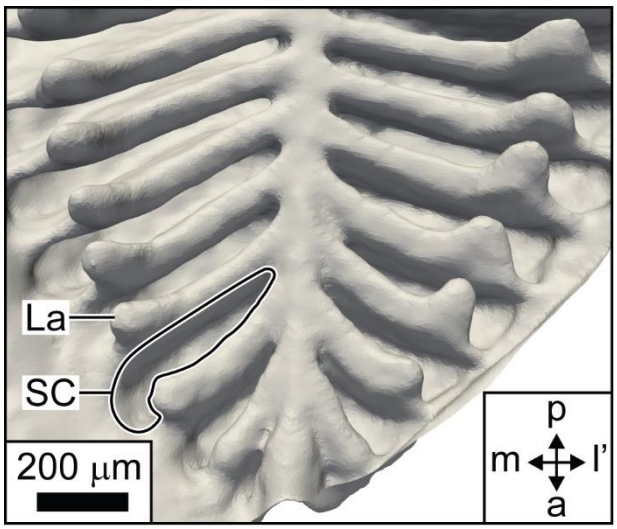

Fig. A.20. Guide to Fig. A.19. Section from right nasal chamber of sea catfish CFD model. a: Anterior; l': lateral; La: olfactory lamella; m: medial; p: posterior; SC: sensory channel.

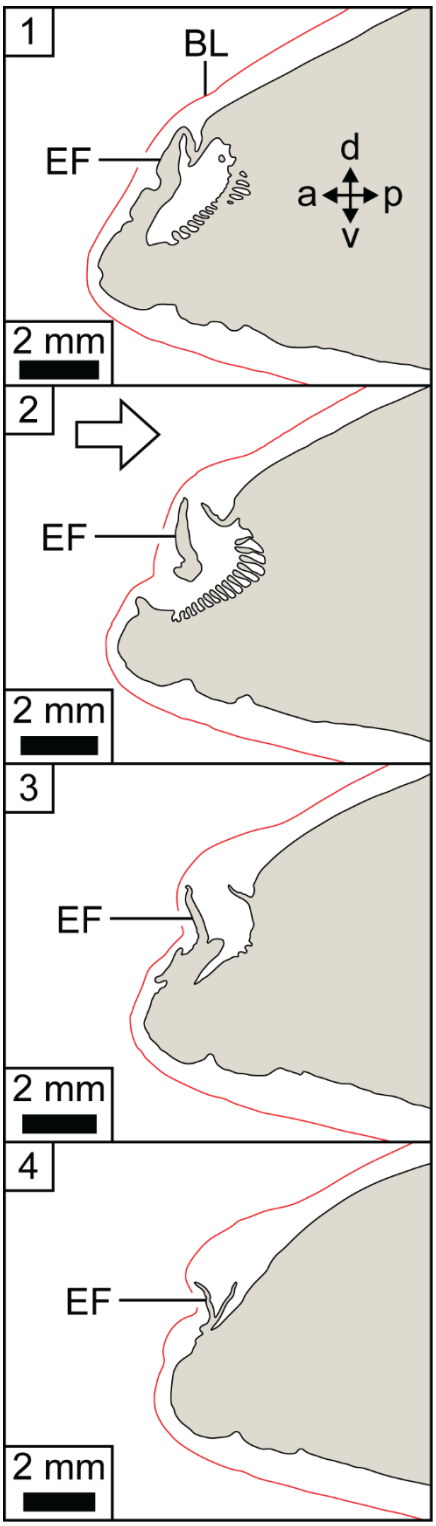

Fig. A.21. Boundary layer in four sagittal slices through CFD mesh of right nasal region of sea catfish. Location of each slice shown in Fig. A.23A. Reynolds number: 300. Yaw: 0°. Arrow: direction of free-stream flow. Red line: outer limit of boundary layer (defined by a vorticity of 50 s^{-1}). a: Anterior; BL: boundary layer; d: dorsal; EF: excurrent nasal flap; p: posterior; v: ventral.

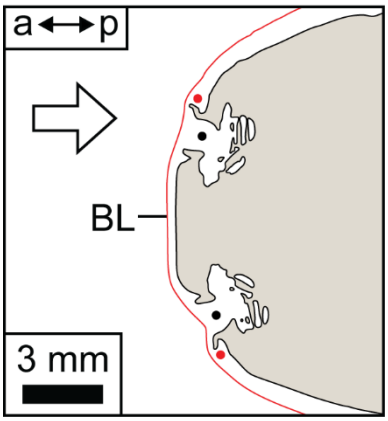

Fig. A.22. Boundary layer in horizontal slice through CFD mesh of sea catfish. Location of slice shown in Fig. A.23B. Reynolds number: 300. Yaw: 0°. Arrow: direction of free-stream flow. Red line: outer limit of boundary layer (defined by a vorticity of 50 s^{-1}). Red disk: incurrent nasal flap; black disk: incurrent nostril. a: Anterior; BL: boundary layer; p: posterior.

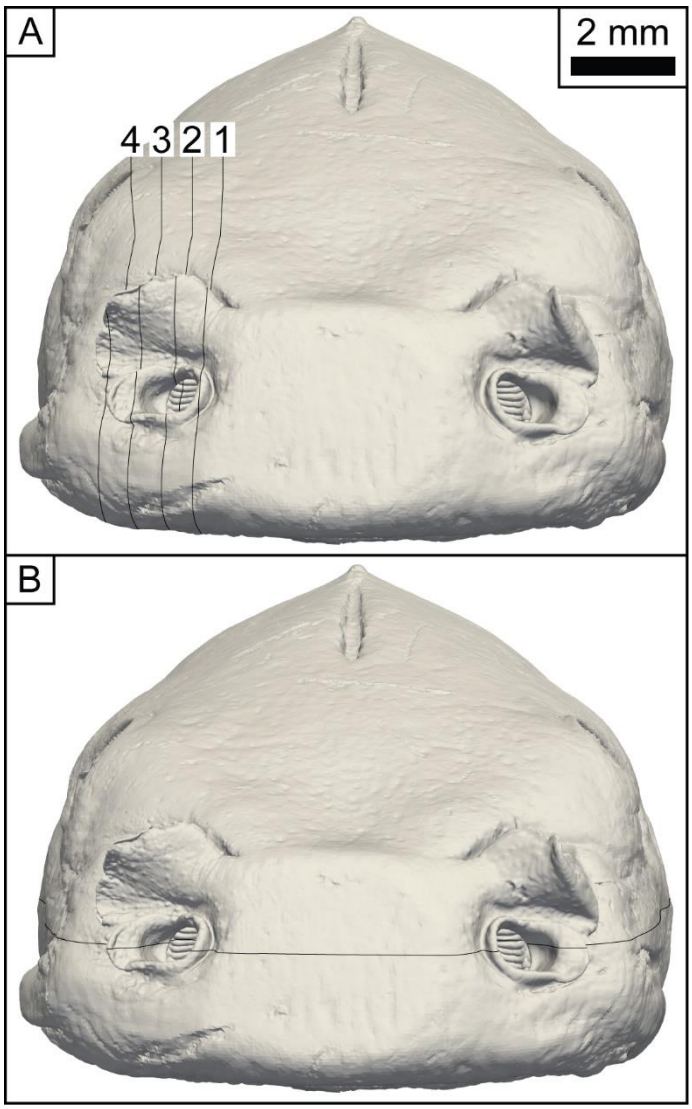

Fig. A.23. Locations of slices in (A) Fig. A.21 and (B) Fig. A.22. Anterior aspect of surface model of sea catfish head (same aspect as Fig. 6C).